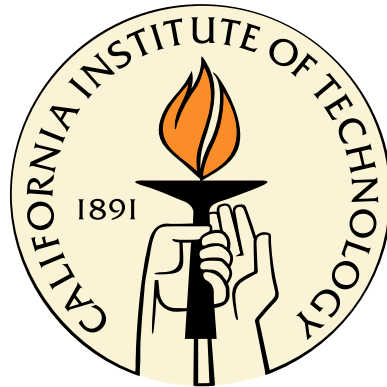


# Models of Turbulent Pipe Flow

Thesis by  
Jean-Loup Bourguignon

In Partial Fulfillment of the Requirements  
for the Degree of  
Doctor of Philosophy



California Institute of Technology  
Pasadena, California

2013  
(Defended November 5, 2012)

© 2013

Jean-Loup Bourguignon

All Rights Reserved

# Acknowledgments

The guidance and support of Beverley McKeon, Dennice Gayme, Rashad Moarref, Ian Jacobi, and Jeff LeHew are gratefully acknowledged. Xiaohua Wu kindly provided the DNS data for this thesis. The comments and feedback of Ati Sharma and Joel Tropp on the third chapter were appreciated, as well as their insightful advice. Support for this research provided by the Air Force Office of Scientific Research under award # FA9550-09-1-0701 was greatly appreciated.

# Abstract

The physics of turbulent pipe flow was investigated via the use of two models based on simplified versions of the Navier-Stokes equations. The first model was a streamwise-constant projection of these equations, and was used to study the change in mean flow that occurs during transition to turbulence. The second model was based on the analysis of the turbulent pipe flow resolvent and provided a radial basis for the modal decomposition of turbulent pipe flow. The two models were tested numerically and validated against experimental and numerical data.

Analysis of the streamwise-constant model showed that both non-normal and nonlinear effects are required to capture the blunting of the velocity profile, which occurs during pipe flow transition. The model generated flow fields characterized by the presence of high- and low-speed streaks, whose distribution over the cross-section of the pipe was remarkably similar to the one observed in the velocity field near the trailing edge of the puff structures present in pipe flow transition.

A modal decomposition of turbulent pipe flow, in the three spatial directions and in time, was performed, and made possible by the significant reduction in data requirements achieved via the use of compressive sampling and model-based radial basis functions. The application and efficiency of compressive sampling in wall-bounded turbulence was demonstrated.

Approximately sparse representations of turbulent pipe flow by propagating waves with model-based radial basis functions were derived. The basis functions, obtained by singular value decomposition of the resolvent, captured the wall-normal coherence of the flow and provided a link between the propagating waves and the governing equations, allowing for the identification of the dominant mechanisms sustaining the waves, as a function of their streamwise wavenumber.

Analysis of the resolvent showed that the long streamwise waves are amplified mainly via non-normality effects, and are also constrained to be tall in the wall-normal direction, which decreases the influence of viscous dissipation. The short streamwise waves were shown to be localized near the critical-layer (defined as the wall-normal location where the convection velocity of the wave equals the local mean velocity) and thus exhibit amplification with a large contribution from criticality. The work in this thesis allows the reconciliation of the well-known results concerning optimal disturbance amplification due to non-normal effects with recent resolvent analyses, which highlighted the importance of criticality effects.

# Contents

<b>Acknowledgments</b>	<b>iii</b>
<b>Abstract</b>	<b>iv</b>
<b>List of Figures</b>	<b>vii</b>
<b>List of Tables</b>	<b>xiii</b>
<b>List of Symbols</b>	<b>xv</b>
<b>1 Introduction</b>	<b>1</b>
1.1 Motivation . . . . .	1
1.2 Analysis of the Navier-Stokes Equations Linearized Around the Laminar Profile . . .	2
1.3 Linear Analyses Based on the Turbulent Mean Velocity Profile . . . . .	4
1.4 Nonlinear Studies in Wall-Bounded Turbulence . . . . .	5
1.5 Data-Based Analyses to Infer the Structure of Turbulence . . . . .	6
1.6 Thesis Outline . . . . .	8
<b>2 A Streamwise-Constant Model of Turbulent Pipe Flow</b>	<b>10</b>
2.1 Introduction . . . . .	10
2.2 Description of the Model and Numerical Methods . . . . .	13
2.3 Simplified Streamwise-Constant Model with Deterministic Forcing . . . . .	15
2.4 Stochastic Forcing of the Streamwise-Constant Model . . . . .	19
2.5 Summary . . . . .	25
<b>3 Efficient Representation of Wall-Bounded Turbulence Using Compressive Sampling</b>	<b>26</b>
3.1 Introduction . . . . .	26
3.2 Methodology . . . . .	28
3.2.1 Synthetic Velocity Fields . . . . .	29
3.2.2 DNS Velocity Fields . . . . .	32

3.3	Results . . . . .	34
3.3.1	Demonstration of Compressive Sampling Using Synthetic Velocity Fields . . .	34
3.3.2	Sparsity Check Based on Periodically Sampled DNS Data . . . . .	37
3.3.3	Frequency Analysis of Randomly Sampled DNS Data via Compressive Sampling	37
3.3.4	Comparison with Periodic Sampling . . . . .	47
3.4	Summary . . . . .	49
<b>4</b>	<b>Sparse Representation of Turbulent Pipe Flow by Propagating Waves and a Model-Based Radial Basis</b>	<b>52</b>
4.1	Introduction . . . . .	52
4.2	Methodology . . . . .	58
4.2.1	Decomposition in the Streamwise and Azimuthal Directions . . . . .	60
4.2.2	Decomposition in Time . . . . .	60
4.2.3	Decomposition in the Radial Direction . . . . .	62
4.2.4	Proper Orthogonal Decomposition . . . . .	64
4.3	Results . . . . .	65
4.3.1	Two-dimensional Fourier Modes ( $\mathbf{k}, \mathbf{n}$ ) . . . . .	65
4.3.2	Fourier Modes ( $\mathbf{k}, \mathbf{n}, \mathbf{u}_c$ ) . . . . .	68
4.3.3	Streamwise Singular Modes ( $\mathbf{k}, \mathbf{n}, \mathbf{u}_c, \mathbf{q}$ ) . . . . .	69
4.3.4	Comparison with Proper Orthogonal Decomposition . . . . .	75
4.4	Discussion . . . . .	78
4.4.1	Componentwise Form of the Input-Output Relationship . . . . .	78
4.4.2	Influence of Non-Normality on Disturbance Amplification . . . . .	82
4.4.3	Influence of Criticality on Disturbance Amplification for High $\mathbf{k}$ Modes . . .	85
4.4.4	Implications of the Present Study on Analyses on Criticality and Non-Normality	90
4.5	Summary . . . . .	93
<b>5</b>	<b>Conclusion</b>	<b>95</b>
<b>A</b>	<b>Matlab code used to solve the convex optimization problem</b>	<b>97</b>
	<b>Bibliography</b>	<b>97</b>

# List of Figures

2.1	The coordinate system used to project the Navier-Stokes equations. . . . .	14
2.2	(a) Streamfunctions $\Psi_{1,a-c}(r)$ and (b) corresponding velocity profiles $u_0(r)$ for $\Psi_{1,a}(r) = 0.033(r - 3r^3 + 2r^4)$ (thin solid), $\Psi_{1,b}(r) = 0.7(r - 3r^3 + 2r^4)^2$ (dashed), $\Psi_{1,c}(r) = 14(r - 3r^3 + 2r^4)^3$ (dash-dot) and experimental velocity profile of den Toonder & Nieuwstadt (1997) at $Re = 24,600$ (thick solid). . . . .	17
2.3	Model output for deterministic forcing: (a) contours of the streamfunction $\Psi = 0.033(r - 3r^3 + 2r^4) \sin \theta$ , (b) vector plot of the corresponding in-plane velocities, and (c) contours of the resulting axial velocity field. . . . .	19
2.4	Contours of the axial velocity induced by the streamfunction $\Psi_6(r, \theta) = (r^4 - 2r^5 + r^6) \sin(6\theta)$ , the light and dark filled contours correspond to regions of the flow respectively faster and slower than laminar. . . . .	20
2.5	Time traces of the centerline velocity from three different simulations respectively at $Re = 2,200$ with 0.0005 and 0.002 rms noise levels (a), (c) and at $Re = 10,000$ with 0.002 rms noise level (b). The resolution in the radial direction is $N = 48$ . (d) Zoom on the time interval during which the samples of figure 2.6 are taken. The vertical lines indicate the sampling instants. . . . .	21
2.6	Contours of the axial velocity, subfigures (a) to (c), and of the swirling strength for the in-plane velocities, subfigures (d) to (f), computed respectively at $\tau = 1620$ , $\tau = 1700$ , and $\tau = 1740$ dimensionless time units. . . . .	22
2.7	Diagram detailing the different stages of the QSSP. The dashed lines represent unmodeled effects. . . . .	24
3.1	Schematic of pipe geometry and nomenclature (McKeon & Sharma, 2010). . . . .	29
3.2	Frequency range resolved by the periodically sampled DNS data (delimited by the two horizontal dashed lines) compared to the empirical upper and lower bounds on the DNS frequency content (solid lines) as a function of the streamwise wavenumber $k$ . The shaded area shows the time-resolved streamwise wavenumber range for the available data. . . . .	33

3.3	Frequency spectrum premultiplied by $r$ as a function of the wall-normal distance $y$ , for the large-scale mode $(k, n) = (1, 10)$ , with the 8 input frequencies reported on table 3.1, sampled during 100 (a) and 25 (b) dimensionless time units. The distorted contours (b) indicate that the sparsity relationship is not satisfied. . . . .	35
3.4	Wall-normal profile of the magnitude (a) and phase (b) for the first three most energetic modes $(k, n) = (0.21, -2)$ (dotted), $(k, n) = (0.42, 3)$ (dashed), and $(k, n) = (0.21, 2)$ (solid) of the periodically sampled DNS flow field. . . . .	38
3.5	Representative frequency spectrum corresponding to the 2D Fourier mode $(k, n) = (0.42, 5)$ as a function of the wall-normal distance, with the empirical upper and lower bounds on frequency, corresponding to convection velocities equal to the centerline velocity and 10 times the friction velocity, demarcated by the two vertical lines. . . .	39
3.6	The 50 DNS sampling time instants randomly distributed over 100 dimensionless time units based on the radius and bulk velocity. The last sampling time instant is at $\tau = 96.57$ . . . . .	39
3.7	Power spectral density over the frequency range $f \in [0, 0.1]$ as a function of the wall-normal distance (a),(c) and integrated in the wall-normal direction (b),(d) for the 2D Fourier mode $(k, n) = (0.21, 2)$ from the randomly sampled DNS. The top and bottom rows correspond to a local minimization with respectively 400 and 800 optimization frequencies. The dots (b),(d) indicate the sparse frequencies. . . . .	41
3.8	Wall-normal profiles of the Fourier modes $(k, n, \omega) = (0.21, 2, 2\pi f)$ from the randomly sampled DNS, for the different dominant frequencies, compared to the time average of the original and reconstructed signals computed using the local (a) and global (b) minimizations with 400 optimization frequencies, and the local (c) and global (d) minimizations with 800 optimization frequencies. The maximum frequency for the optimization is 1 in both cases. . . . .	42
3.9	Power spectral density for the 2D Fourier mode $(k, n) = (0.21, 2)$ from the randomly sampled DNS obtained via optimal compressive sampling. . . . .	43
3.10	Contours of the real part of the 2D Fourier mode $(k, n) = (0.21, 2)$ from the randomly sampled DNS, as a function of the wall-normal distance and time, with all the frequencies included (a) and with only three dominant frequencies recovered from compressive sampling included (b). . . . .	44
3.11	Contours of the real part of the 2D Fourier modes $(k, n) = (1.05, 2)$ (a) and $(k, n) = (3.14, 4)$ (c) from the randomly sampled DNS as a function of the wall-normal distance and time. Wall-normal profiles of the Fourier modes $(k, n, \omega) = (1.05, 2, 2\pi f)$ (b) and $(k, n, \omega) = (3.14, 4, 2\pi f)$ (d) for the different sparse frequencies compared to the time average of the original and reconstructed signals. . . . .	45

3.12	(a) Time-averaged power spectral density in the wall-normal direction for the 2D Fourier mode $(k, n) = (3.14, 4)$ from the randomly sampled DNS. (b) Contours of the real part of the 2D Fourier mode $(k, n) = (3.14, 4)$ low-pass filtered and (c) high-pass filtered showing the two different types of uniform momentum zones present in the wall-normal direction. . . . .	46
3.13	Frequency content of the 2D Fourier modes as a function of the streamwise wavenumber for various azimuthal wavenumbers (a). The two solid lines indicate the upper and lower empirical bounds on the frequency content and the dashed line shows the streamwise wavenumber corresponding to the near-wall type modes. The shaded areas highlight the dynamically significant bandwidth and streamwise wavenumber range at $Re = 24, 580$ (a) and extrapolated to $Re = 300, 000$ (b). . . . .	47
3.14	Comparison between the time-averaged wall-normal profile of the 2D Fourier mode $(k, n) = (0.21, 2)$ from the randomly sampled DNS and its two sparse frequencies obtained using compressive sampling with 14 and 50 snapshots. . . . .	49
3.15	Power spectral density of a superposition of three Fourier modes with unit magnitude and frequencies $f = 0.035, 0.052, 0.087$ sampled 50 times during 100 time units computed using (a) periodic sampling with FFT, and (b) compressive sampling with a frequency increment of $df = 0.01$ and (c) $df = 0.001$ . . . . .	50
4.1	The 50 DNS sampling time instants randomly distributed over 100 dimensionless time units based on the radius and bulk velocity. The last sampling time instant is at $t = 96.57$ .	59
4.2	Schematic of pipe geometry and nomenclature. . . . .	60
4.3	Block diagram representing the decomposition of fully developed turbulent pipe flow as a sum of propagating waves. . . . .	61
4.4	Comparison of the first (solid), second (dotted), and tenth (dashed) singular mode profiles of the streamwise velocity component before (black) and after (gray) applying the QR decomposition for the set of parameters $(0.21, 2, 0.83)$ . For the first two modes, the profiles before and after QR decomposition are identical to plotting accuracy. . . .	64
4.5	Convergence of the turbulence intensities and kinetic energy as a function of the number of 2D Fourier modes for one representative DNS snapshot. . . . .	66
4.6	Time average wall-normal profile of the 2D Fourier mode $(k, n) = (0.21, 2)$ compared to the reconstructed profile using only the three dominant frequencies. The profiles of the Fourier modes $(0.21, 2, u_c)$ at the three dominant frequencies corresponding to the convection velocities $u_c = 0.71, 0.83, 0.95$ are also shown for comparison. . . . .	67

4.7	Contour plots of streamwise velocity fluctuations at $\theta = 0$ for the DNS flow field Fourier filtered in the streamwise direction (a) and the Fourier series approximation with 51 $(k,n)$ modes capturing 20% of the streamwise turbulence intensity (b). . . . .	67
4.8	Contours of the real part of the 2D Fourier mode $(k, n) = (0.21, 2)$ as a function of the wall-normal distance and time with all the frequencies included (a) and with only the three dominant frequencies included (b). The contours are obtained by interpolation between the randomly sampled velocity fields, and plotted at $\theta = 0$ and $x = 0$ . . . . .	69
4.9	Contours of the streamwise velocity fluctuations in the streamwise and wall-normal directions at two different time instants separated by half a period of the longest structures or about 14.3 dimensionless time units. The velocity fields from top to bottom are reconstructed based on a superposition of respectively the top 2, 4, and 16 dominant $(k,n)$ wavenumber pairs with all the sparse frequencies included. The bottom velocity field correspond to the DNS data Fourier filtered to remove the small scales. . . . .	70
4.10	Wall-normal profiles for the magnitude (a),(c) and phase (in radians) (b),(d) of the singular modes (a),(b) $(k, n, u_c, q) = (0.21, 2, 0.83, 1)$ (dotted), $(0.21, 2, 0.83, 2)$ (dashed), and $(0.21, 2, 0.83, 3)$ (solid); and (c),(d) $(0.21, 2, 0.83, 4)$ (dotted), $(0.21, 2, 0.83, 5)$ (dashed), and $(0.21, 2, 0.83, 6)$ (solid). Energy (e) and cumulative energy (f) captured as a function of the mode order and normalized by the DNS mode energy $u'^2$ with (solid) and without (dashed) QR orthonormalization. . . . .	71
4.11	Wall-normal profiles for the magnitude (a) and phase (in radians) (b) of a superposition of 1 $(k, n, u_c, q) = (0.21, 2, 0.83, 1)$ , 3 $(0.21, 2, 0.83, 1 : 3)$ , and 6 $(0.21, 2, 0.83, 1 : 6)$ singular modes compared to the Fourier mode $(k, n, u_c) = (0.21, 2, 0.83)$ magnitude and phase profiles. . . . .	72
4.12	Contours of the streamwise velocity fluctuations in a streamwise wall-normal plane for the Fourier mode $(k, n, u_c) = (0.21, 2, 0.83)$ and its representation as a sum of respectively 1 $(k, n, u_c, q) = (0.21, 2, 0.83, 1)$ , 3 $(0.21, 2, 0.83, 1 : 3)$ , and 6 $(0.21, 2, 0.83, 1 : 6)$ singular modes (top to bottom). The horizontal dashed lines delimitate the region where the Fourier mode and its representation are in phase. . . . .	73
4.13	Average number of singular modes $N_m$ required to capture 95% of $u'^2$ as a function of the streamwise wavenumber (a) and convection velocity (b) based on the decomposition of 134 Fourier modes from the DNS turbulent pipe flow realization. . . . .	74
4.14	Wall-normal profile of the synthetic Fourier coefficient $c_{k,n,\omega}(r) = (1-r)r^4$ (a). Number of streamwise singular modes required to capture 99% of the analytic Fourier coefficient energy at $(k, n, u_c) = (0.21, 2, 0.77)$ (solid) and $(k, n, u_c) = (1.47, 2, 0.77)$ (dashed) (b). . . . .	75

4.15	Time-averaged wall-normal profile (a) and energy integrated in the wall-normal direction as a function of time (b) of the 2D Fourier mode $(k, n) = (0.21, 2)$ (dashed) together with the first POD mode (solid, black) and the reconstructed 2D Fourier mode based on three dominant frequencies (solid, grey). Note that the temporal Fourier basis functions are not orthogonal on the set of randomized sampling time instants such that Parseval's theorem does not apply, i.e., the time average profile differs from the square root of the sum of the square of the three frequency components. (c) Phase of the time-varying amplitude coefficient of the first POD mode compared to the phase of the most energetic Fourier mode $(k, n, u_c) = (0.21, 2, 0.83)$ . The phase of the Fourier mode depends on the wall-normal distance but the phase speed is constant. The origin of phase is chosen to match the POD mode. . . . .	76
4.16	Streamwise (a),(c) and azimuthal (b),(d) contributions to the forcing (top row) and response (bottom row) energy, as a function of the streamwise wavenumber and singular mode order, in the presence of mean shear and for $n = 3, u_c = 0.8$ . . . . .	80
4.17	Cross-sectional contribution to the forcing energy for the first singular mode and with $n = 3$ . The preferential forcing direction switches from being mainly in the cross-sectional plane at low $k$ to being mainly streamwise at high $k$ at a value of $k$ around 4 – 5 corresponding to the streamwise length of the near-wall type structures ( $k = 4.3$ corresponds to 1,000 viscous length units at $Re = 24,580$ ). . . . .	81
4.18	Amplification as a function of the singular mode order with (solid) and without (dashed) the linear coupling term for the modes $(k, n, u_c) = (k, 3, 0.5)$ (a) and $(k, n, u_c) = (k, 3, 0.8)$ (b) for three different streamwise wavenumbers $k = 0.1, 1, 10$ . The arrow indicates the direction of increasing $k$ . . . . .	83
4.19	Streamwise (a),(c) and azimuthal (b),(d) contributions to the forcing (top row) and response (bottom row) energy, as a function of the streamwise wavenumber and singular mode order, in the absence of mean shear and for $n = 3, u_c = 0.8$ . . . . .	84
4.20	Magnitude of the streamwise velocity component of the singular mode with 5 local peaks for the Fourier modes $(k, n, u_c) = (1, 3, 0.5)$ (a) and $(k, n, u_c) = (1, 3, 0.8)$ (b) with (solid) and without (dashed) non-normality effects. The modes have a significantly different shape even though the amplification is the same with or without mean shear for these modes at $k = 1$ . The order of the singular mode with five local peaks from SVD of the coupled and uncoupled resolvent is $q = 5$ and $q = 9$ , respectively. . . . .	85
4.21	Fraction of energy contained in an annulus centered on the critical layer and covering 10% of the cross-sectional area as a function of the singular mode order. A uniform distribution of energy would correspond to 10% energy in the annulus. . . . .	86

4.22 Wall-normal profile of (a) the DNS propagating wave  $(k, n, u_c) = (0.84, 3, 0.83)$ , (b) decomposed into the first three singular modes with (dashed) and without (solid) non-normality effects and (c) a residual containing energy mainly away from the critical layer, and corresponding to the higher-order singular modes. . . . . 88

4.23 Schematic of the regions where non-normality effects (1 and 2) and criticality effects (2 and 3) are important on top of the contours of the singular value on a logarithmic scale, as a function of the streamwise wavenumber and singular mode order at  $(n, u_c) = (3, 0.8)$ . The line delimiting the region where non-normality effects are important (regions 1 and 2) follows the contours of the singular value, indicating that the amplification is significantly larger in the presence of non-normality effects. In region 4, the amplification is relatively low and inversely proportional to the viscosity as is the case for a normal system. . . . . 89

4.24 Thickness of the first singular mode as a function of the streamwise wavenumber  $k$  at  $u_c = \frac{2}{3}$  and  $n = 3$  (a) and as a function of the mean shear at the critical layer  $U'_{crit}$  for  $u_c$  varying from 0.5 to 0.95 by increments of 0.05 at  $k = 1$  and  $n = 3$ . The dots indicate the data points, the solid and dashed lines correspond to the scaling laws  $k^{-\frac{1}{3}}$  and  $k^{-\frac{1}{2}}$  (a), respectively, and  $U'^{-\frac{1}{3}}_{crit}$  (b). . . . . 91

4.25 Wall-normal profile of the first singular modes  $(k, n, u_c) = (1 : 2 : 8, 3, \frac{2}{3})$  (a) and  $(k, n, u_c) = (1, 3, 0.5 : 0.1 : 0.9)$  (b). The arrow indicates the direction of increasing  $k$  (a) and  $u_c$  (b). . . . . 92

# List of Tables

3.1	Parameters and optimization results for the three test cases. The input frequencies come from the content of the synthetic velocity fields, the output frequencies are those recovered by optimized compressive sampling. . . . .	36
3.2	Frequency analysis of 5 representative modes using only 14 snapshots acquired over 100 dimensionless time units from two different runs of the turbulent pipe flow DNS. The dominant frequencies obtained via compressive sampling analysis of the randomly sampled DNS and their streamwise energy content are reported in the second and third columns, respectively. The fourth and fifth columns correspond to the frequencies and respective energy content obtained by FFT of the periodically sampled DNS. . . . .	48
4.1	Top 10 $k \neq 0$ 2D Fourier modes and percentage of the time-average (over the 50 randomly sampled velocity field) streamwise turbulence intensity captured. . . . .	65
4.2	Comparison of the parameters for the Duggeby <i>et al.</i> (2007) POD analysis and the present modal decomposition including the sampling duration $T_s$ , the number of degrees of freedom DOF (grid points) used to compute the modes, and the number of modes $N_{modes}$ required to capture 90% of the TKE / $u'^2$ for the two analyses, respectively. The last row indicates the order of the successive decompositions performed on the data.	77



# List of Symbols

## *Parameters*

$C_p$	Dimensionless pressure gradient
$D$	Pipe diameter
$df$	Frequency increment
$f$	Frequency
$f_0$	Fundamental frequency
$f_{max}, f_{min}$	Maximum and minimum resolvable frequencies
$f_s$	Sampling frequency
$k$	Streamwise wavenumber
$K$	Number of sparse frequencies
$k_{min}$	Minimum resolvable streamwise wavenumber
$n$	Azimuthal wavenumber
$N$	Radial resolution ( $N = N_r - 3$ )
$N_{opti}$	Number of optimization frequencies
$N_r$	Number of grid points in the radial direction
$N_s$	Number of samples
$q$	Mode order, quantum number
$R$	Pipe radius
$Re$	Reynolds number ( $Re = \frac{\bar{U}D}{\nu}$ )
$Re_\tau$	Friction Reynolds number ( $Re_\tau = \frac{u_\tau R}{\nu}$ )
$\bar{U}$	Bulk velocity
$u_c$	Convection velocity, phase speed, normalized by the centerline velocity
$U_{CL}$	Centerline velocity
$u_\tau$	Friction velocity
$\lambda$	Eigenvalue
$\lambda^+$	Streamwise wavelength in wall units
$\nu$	Kinematic viscosity
$\sigma$	Singular value
$\omega$	Angular frequency ( $\omega = 2\pi f$ )
$\Omega$	Bandwidth of the signal
$\Omega_{fl}$	Flow domain

*Variables*

$r$	Radial distance normalized by the pipe radius $R$
$x$	Streamwise distance normalized by the pipe radius $R$
$X$	Vector of spatial variables $X = (x, y, z)^T$ or $X = (x, r, \theta)^T$
$y$	Wall-normal distance normalized by the pipe radius $R$ ( $y = 1 - r$ )
$\theta$	Azimuth, polar angle
$\tau$	Dimensionless time ( $\tau = \frac{\bar{U}t}{R}$ )

*Scalar Fields*

$\bar{c}(r)$	Spatio-temporal averaged POD mode for the streamwise fluctuations
$\bar{c}_{k,n}(r)$	Time-averaged 2D Fourier coefficient for the streamwise fluctuations
$c_{k,n}(r, t)$	2D Fourier coefficient coefficient for the streamwise fluctuations
$\mathcal{N}_\psi(r, \theta)$	Cross-stream stochastic forcing
$u'^2(r)$	Streamwise turbulence intensity
$u(x, r, \theta, t)$	Streamwise velocity fluctuations
$u_r(x, r, \theta, t)$	Radial velocity fluctuations
$u_\theta(x, r, \theta, t)$	Azimuthal velocity fluctuations
$U(r)$	Mean velocity profile, base flow
$\phi(x, r, \theta, t)$	Generic 1 component of velocity POD mode
$\Psi(r, \theta)$	Cross-stream streamfunction

*Vector Fields*

$\mathbf{c}_{k,n,\omega}(r)$	3D Fourier coefficient (streamwise, azimuthal, temporal)
$\mathbf{f}_{k,n,\omega}(r)$	Forcing mode
$\mathbf{c}_{k,n,\omega,q}(r)$	Left (response) singular mode
$\mathbf{f}_{k,n,\omega,q}(r)$	Right (forcing) singular mode
$\mathbf{u}(x, r, \theta, t)$	Velocity fluctuations ( $\mathbf{u} = (u_r, u_\theta, u)^T$ )
$\hat{\mathbf{u}}(x, r, \theta, t)$	Synthetic velocity fields
$\mathbf{U}(r)$	Base flow ( $\mathbf{U} = (0, 0, U(r))^T$ )
$\Phi(x, r, \theta, t)$	Generic 3 components of velocity POD mode

# Chapter 1

## Introduction

### 1.1 Motivation

The flow through pipes is of significant industrial importance and is representative of a more general class of wall-bounded flows including boundary-layers and channels. Pipe flow occurs in a variety of settings from the movement of oil in intercontinental pipelines to the flow through arteries and capillaries. The particularly simple geometry of the flow led to many experimental studies resulting in the discoveries, among others, of Osborne Reynolds on transition more than 125 years ago. The flow exhibits three different regimes: laminar, transitional, and turbulent. At the Reynolds number representative of industrial applications, the flow is most often turbulent. The Reynolds number is defined as  $Re = \frac{\bar{U}D}{\nu}$ , where  $\bar{U}$  is the bulk velocity,  $D$  the pipe diameter, and  $\nu$  the kinematic viscosity of the fluid.

The transition from an organized laminar state to a disorganized three-dimensional (3D) turbulent state in pipe flow causes a significant increase in the pumping power required to move the fluid along the pipe. The transition occurs naturally once the Reynolds number is increased past a critical value depending on the flow facility, even though pipe flow is linearly stable for all Reynolds numbers. The turbulent state appears disorganized, yet exhibits coherent structures that play an important role in the dynamics, and are responsible for sustaining turbulence. Coherent structures are defined by Berkooz *et al.* (1993) as *organized spatial features which repeatedly appear and undergo a characteristic temporal life cycle*. The structures can be observed in both the velocity and vorticity fields. The different types of coherent structures observed in wall-bounded turbulence are described in details in the review article by Robinson (1991). In this thesis, only the velocity field is considered, and the structures are defined as zones of nearly uniform streamwise momentum, evolving coherently in time.

Turbulent pipe flow is often decomposed into a mean component  $\mathbf{U}$  and fluctuations about the mean  $\mathbf{u}$ , which is called a Reynolds decomposition of the flow. The fluctuations arise due to the coherent structures and disorganized motions. Understanding the generation and maintenance of the

turbulent fluctuations, and the change in mean flow during transition (which is related to the drag increase) is one of the last unsolved problems in classical physics, as discussed by Gad-el-Hak in the editorial preceding the article by George & Castillo (1997). New insight gained into the maintenance of fully developed turbulence or into pipe flow transition is expected to result in the identification of more efficient approaches to manipulate the flow. Typical flow manipulations include suppressing turbulence or decreasing the drag down to a level closer to laminar flow drag.

The Navier-Stokes (NS) equations are a set of nonlinear partial differential equations describing the motion of fluid particles. Very few analytical solutions of these equations are known, mainly for laminar flows in simple geometries. Laminar pipe flow is one such example for which the NS equations can be solved analytically, by assuming that the flow is one-dimensional, and that it depends only on the wall-normal distance. For more general flows, including transitioning and turbulent flows, the NS equations need to be drastically simplified in order to make analytical progress. One such simplification is to linearize the equations around the laminar velocity profile, under the assumption that the perturbations of the laminar state are infinitely small, leading to an eigenvalue analysis of the flow.

In this chapter, the literature on linear and nonlinear analysis of the NS equations in wall-bounded turbulence is reviewed to provide some background for the present study. The literature on this subject is really broad and only the works most pertinent to this thesis are highlighted. Linear analyses focus on perturbations around an input mean flow. If the input mean flow is laminar, perturbations that are relevant for transition to turbulence are identified, whereas if the mean flow is turbulent, the most amplified perturbations are hypothesized to capture important features of turbulence, such as the coherent structures and the scaling of the turbulent fluctuations with Reynolds number. Nonlinear analyses are also reviewed as they provide a way to study the change in mean flow, which occurs during transition that linear studies cannot capture.

## 1.2 Analysis of the Navier-Stokes Equations Linearized Around the Laminar Profile

Eigenvalue analysis of pipe flow linearized around the laminar profile has showed that there is no critical Reynolds number above which disturbances grow exponentially (Schmid & Henningson, 1994). Hence, linear theory predicts that laminar pipe flow is linearly stable for all Reynolds numbers, in contradiction to experimental observations. Schmid & Henningson (1994) considered the evolution of the solutions to a linear initial-value problem, and showed that even though the solutions decay exponentially at large times, significant transient growth can be obtained on a shorter timescale. The transient growth is due to the non-normality of the underlying linear operator (the operator does not commute with its adjoint), and provides a way to trigger finite-amplitude effects leading to tran-

sition to turbulence. Schmid & Henningson (1994) showed that the optimal disturbance exploiting the transient growth mechanism maximally is streamwise-constant with an azimuthal wavenumber  $n = 1$ , and spans the whole flow domain, i.e., is not localized in the wall-normal direction. Non localized modes will henceforth be referred to as global modes, meaning that they span a significant fraction of the radius. The non-normality sustains the possibility of transient growth and high sensitivity to disturbances, and is due to the presence of mean shear providing a coupling between the cross-sectional velocities and the streamwise velocity (Jovanovic & Bamieh, 2005).

Farrell & Ioannou (1993) used small-amplitude stochastic forcing of the linearized NS equations for Couette flow to show that a high level of fluctuating energy can be maintained via extraction of energy from the mean flow by the stochastic disturbances. The principal forcing and response modes differ from each other (and from the normal modes due to the non-normality of the linearized NS equations), and span most of the flow domain, i.e., are global modes. Those authors argued that, if a mechanism to replenish the growing subspace of optimal disturbances is present, a non laminar statistically steady state can be reached. The nonlinear interaction of the disturbances neglected in the linear study may provide such a mechanism. However, this mechanism of bypass transition to turbulence was questioned by Waleffe (1997), who showed that the growth of the most amplified disturbances modifies the mean flow in a way that reduces the amplification potential. Bypass transition is described in more detail in Schmid (2000).

Further insight into the importance of non-normality in the amplification of disturbances was obtained by Jovanovic & Bamieh (2005), who considered the linearized NS equations for channel flow under the action of temporally and spatially varying body forces, and found that the largest amplification is obtained by forcing in the cross-sectional plane, and is observed in the streamwise velocity component. The largest amplification is obtained for streamwise-constant forcing and response modes, i.e., modes with vanishing streamwise wavenumber ( $k = 0$ ), corresponding to streamwise vortices and streaks (Jovanovic & Bamieh, 2005).

The above-mentioned analyses based on the NS equations linearized around the laminar profile focused on the temporal evolution of initial disturbances, or on the flow response to stochastic or deterministic forcing, to show that transition may be started by linear non-normal effects, resulting in the formation of finite size disturbances that trigger nonlinear effects. Hence, even though laminar pipe flow is linearly stable for all Reynolds numbers, transition may take place due to transient growth and large amplification of infinitesimal disturbances that are always present in experiments. Jovanovic & Bamieh (2005) showed that the amplification scales unfavorably with the Reynolds number, such that regardless of how well the perturbations are controlled in an experiment, transition will take place when the Reynolds number is high enough for infinitesimal disturbances to grow to a finite size.

### 1.3 Linear Analyses Based on the Turbulent Mean Velocity Profile

The amplification of disturbances in turbulent pipe and channel flows can be studied similarly to the laminar case, by considering the NS equations linearized around the turbulent mean flow, with the additional complexity that the mean flow is not a solution of the NS equations because it needs to be sustained by the Reynolds stress. del Álamo & Jiménez (2006) studied the transient growth of initial conditions using an eddy viscosity to model the interaction of the perturbations with the background turbulence. The eddy viscosity was calibrated such that the mean flow velocity profile, obtained by solving the linearized NS equations, corresponds to the profile obtained from the direct numerical simulation (DNS) of turbulent channel flow. They showed that the turbulent mean flow is also linearly stable, and sustains large amplification of disturbances due to the non-normality associated with the presence of mean shear. Two different types of optimal disturbances, having a spanwise spacing of 100 viscous units and three times the channel height, respectively, were identified in their transient growth analysis. The first type of optimal disturbances was hypothesized to correspond to the sublayer streaks and vortices and the second type to the global modes spanning the full channel. Further study on linear non-normal mechanisms in wall-bounded turbulence by Hwang & Cossu (2010), using the same eddy viscosity as in del Álamo & Jiménez (2006), showed that the optimal disturbances identified using harmonic forcing, stochastic forcing, or based on the transient growth of initial conditions are nearly identical. The optimal forcing and response modes correspond to streamwise-elongated vortices and streaks, respectively.

McKeon & Sharma (2010) proposed to consider the nonlinear terms as an unstructured forcing of the linear dynamics – instead of assuming small perturbations and the existence of external disturbances – to obtain a self-consistent framework for the study of wall-bounded turbulence. The framework is based on the analysis of the transfer function between the forcing (the nonlinear terms) and the response (the velocity field), and only requires the mean velocity profile as an input, obtained either from experimental or DNS data. The use of an eddy viscosity is avoided in this framework by enforcing that the Reynolds stress induced by the nonlinear interaction of the response modes sustains the mean shear, thereby constraining the mean flow not to change in the presence of finite-size fluctuations. The forcing and response modes are harmonic in space and time, and take the form of propagating waves due to their coherence in the wall-normal direction; see chapter 3 for further discussion.

The transfer function is called the resolvent in this setting, and was decomposed into singular modes ranked in decreasing order of their singular value (corresponding to input-output amplification), to identify the most amplified forcing and response modes at each  $(k, n, u_c = \frac{\omega}{kU_{CL}})$ , where  $k$  and  $n$  are the streamwise and azimuthal wavenumbers, respectively,  $\omega$  the angular frequency, and  $u_c$

the convection velocity (phase speed) normalized by the centerline velocity  $U_{CL}$ . The most amplified modes are assumed to play an important role in the flow dynamics, and have been shown to exhibit similarities with observations in simulations and experiments.

Analysis of the turbulent pipe flow resolvent by McKeon & Sharma (2010) showed that large amplification of the forcing modes may be due to non-normality, as is the case in the linearized amplification studies, but also to criticality effects, when the forcing and response modes are localized in the wall-normal direction around the critical-layer. The critical-layer is defined as the point where the local mean velocity matches the convection velocity of the modes. Critical-layers are extensively reviewed in Maslowe (1986) and are also observed in linear stability studies based on the Orr-Sommerfeld equations in Cartesian coordinates.

## 1.4 Nonlinear Studies in Wall-Bounded Turbulence

Kim & Lim (1993) showed through numerical experiments that the linear terms coupling the wall-normal velocity to the wall-normal vorticity are required to maintain turbulence, but these terms are unable to capture the change in mean flow that occurs during transition (Gayme *et al.*, 2010), implying that different simplifications of the NS equations containing at least one nonlinear term are needed. The importance of both linear non-normal and nonlinear mechanisms in the creation and maintenance of a turbulent mean flow was emphasized by Reddy & Ioannou (2000), based on the analysis of energy transfers in Couette flow. The latter authors showed that streamwise-constant modes dominate the energy extraction from the laminar base flow via linear non-normal mechanisms, and maintain by their nonlinear interaction a mean flow that differs from the laminar state.

The prominent role played by the streamwise-constant modes in the linear studies of Bamieh & Dahleh (2001) and Jovanovic & Bamieh (2005), and in the (nonlinear) energy transfer analysis in Couette flow by Reddy & Ioannou (2000), suggests that a streamwise-constant projection of the Navier-Stokes equations could capture significant dynamical processes in wall-bounded turbulence. A streamwise-constant nonlinear model for Couette flow was introduced by Gayme *et al.* (2010) to reproduce the change in mean flow associated with transition to turbulence. The model was stochastically forced to exploit the large amplification of disturbances due to the non-normality of the linearized operator described by Farrell & Ioannou (1993), and successfully captured the blunting of the velocity profile, and structures reminiscent of the streamwise-elongated vortices and streaks observed in experiments.

Exact coherent structures for transitioning pipe flow can be computed by adding a body force to the nonlinear Navier-Stokes equations, and following the 3D states induced by the forcing over to canonical pipe flow (no forcing), by decreasing the body force progressively, as explained in Eckhardt (2007). The exact coherent structures take the form of traveling waves, and exhibit several

streamwise-elongated vortices and streaks. The low-speed streaks are concentrated near the center of the pipe, whereas the high-speed streaks are located close to the wall. On average, the flow is faster near the wall, and slower at the centerline, implying that the traveling waves exhibit a blunter velocity profile, characteristic of pipe flow turbulence. The traveling waves computed in pipe flow are all unstable, but their main features are hypothesized to have been observed in low Reynolds number experiments, e.g., Hof *et al.* (2004). The existence of traveling waves at low Reynolds number can be used to explain transition to turbulence as being a consequence of the appearance of a chaotic saddle in state space, see Eckhardt (2007).

## 1.5 Data-Based Analyses to Infer the Structure of Turbulence

Experimental measurements and DNS of the NS equations are used to provide data for investigating the structure of wall-bounded turbulence. DNS is limited to low Reynolds number flows, due to the sharp increase in resolution requirements with Reynolds numbers (Jiménez & Moser, 2007), but provides full field information, i.e., 3D velocity fields at any time instant. The highest Reynolds number reached by DNS today is 44,000 for the pipe (Wu & Moin, 2008), and 97,000 for the channel (Hoyas & Jiménez, 2006), based on the pipe diameter and channel height, respectively. The physical understanding of wall-bounded turbulence gained from DNS is summarized in Jiménez & Moser (2007).

Experimental measurements in wall-bounded turbulence are of mainly two kinds: point-wise using hot wire anemometry and planar based on Particle Image Velocimetry (PIV). Lately, 3D experimental measurements were made possible by the use of tomographic or holographic techniques, however the field of view is particularly limited, and does not lend itself to spectral measurements. Point-wise measurements usually consist of acquiring time series of the streamwise velocity, which are analyzed by applying a Fast Fourier Transform (FFT) to extract the dominant frequencies. The frequency spectra are often converted into wavenumber spectra, by invoking Taylor hypothesis of frozen turbulence, to infer the streamwise extent of the dominant modes. This approach led to the discovery, among others, of the existence of large amounts of energy at low streamwise wavenumbers, deemed the Very-Large-Scale motions (VLSMs), in high Reynolds number wall-bounded turbulent flows (Kim & Adrian, 1999; Morrison *et al.*, 2004; Guala *et al.*, 2006), and whose strength increases with Reynolds number.

One-dimensional spectral analyses are unable to distinguish between streamwise- and oblique-propagating waves, and are thus contaminated by aliasing effects. The uncertainty on the direction of propagation of the waves can be removed using time-resolved PIV in planes, as in the experiments by LeHew *et al.* (2011) aimed at computing and analyzing 2D + time spectra at different

wall-normal locations. The 2D + time spectra confirmed that the small scales tend to convect at the local mean velocity, as was shown by Morrison *et al.* (1971), whereas the large scales convect faster than the local mean in the near-wall region, therefore invalidating the use of Taylor hypothesis with a scale-independent convection velocity. The discrepancy in the convection velocities can be explained by considering that the large scales extend from the wall to the log region, or even further, and convect at speeds characteristic of the log region.

While PIV in wall-parallel planes as in LeHew *et al.* (2011) permits the flow decomposition as a sum of waves, it does not provide any information on the coherence of the waves in the wall-normal direction. Simultaneous measurements at different wall-normal locations are required to capture the coherence of the structures, and can be obtained using PIV in a streamwise wall-normal plane, as in the experimental visualizations of Meinhart & Adrian (1995), or in a spanwise wall-normal plane as in Hellstroëm *et al.* (2011). The former authors observed large zones of nearly uniform streamwise momentum evolving coherently in time corresponding to coherent structures. The latter authors used PIV to identify the most energetic structures in 3D velocity fields, obtained by reconstructing the flow in the streamwise direction from its temporal evolution in a cross-sectional plane invoking Taylor hypothesis.

The Fourier decomposition of the flow in the homogeneous directions and in time, used in spectral analyses, is optimal in the sense that it maximizes the turbulent kinetic energy captured for a given number of basis functions (Liu *et al.*, 2001). It can be interpreted as a decomposition of the fluctuations into a series of propagating waves. In the wall-normal direction, the flow is inhomogeneous, and the optimality property of the Fourier decomposition is lost.

Proper Orthogonal Decomposition (POD) has been used to obtain an optimal basis (based on a mean turbulent kinetic energy norm) to decompose structures in the wall-normal direction. (Berkoöz *et al.* (1993) showed that, in the homogeneous directions, the POD modes correspond to Fourier modes, such that a spectral analysis is equivalent to a POD, except in the wall-normal direction.) The methods used for performing a modal decomposition by POD of experimental or DNS data are reviewed in chapter 4.

Modal decomposition of wall-bounded turbulence provides a means for identifying the coherent structures, and allows for the development of low-order models by truncation of the series representation of the flow. A full 3D+time data-based modal decomposition of turbulent pipe flow requires numerous time-resolved flow realizations to ensure convergence of the POD modes, and consequently has never been completed. Duggleby *et al.* (2007) used time averaging to decrease the data requirements to perform a POD analysis of turbulent pipe flow DNS data at  $Re = 4,300$ . The POD modes correspond to propagating waves that grow and decay in time, highlighting that the statistical steadiness of the flow is not enforced, due to the time averaging operation and lack of available data.

In addition to requiring large amounts of data, data-based PODs lack a clear link to the physical mechanisms generating and sustaining the coherent structures captured by the POD modes, i.e., the flow dynamics. The shape of the most energetic POD modes is a result of the analysis, and cannot be predicted or explained based on physical arguments. An empirical formula for the shape of the higher-order less-energetic POD modes was developed by Baltzer & Adrian (2011), but does not apply to the low-order POD modes, which depend strongly on the flow geometry.

## 1.6 Thesis Outline

In this thesis two models of pipe flow turbulence, obtained by simplifying the governing equations, are introduced. The first model, described in the next chapter, is nonlinear and consists of an extension of streamwise-constant projections of the NS equations to pipe flow. This model is presented to investigate the basic mechanisms responsible for the change in mean flow, which occurs during pipe flow transition, and is stochastically forced to identify the structures resulting from the large amplification of preferential forcing directions. The mean turbulent profile predicted by the streamwise-constant model can be used as an input for the resolvent analysis, in order to obtain a completely data-independent framework to study wall-bounded turbulence.

The second model is based on the resolvent analysis described in this Introduction. The singular value decomposition of the resolvent provides an orthonormal basis on which to project turbulent pipe flow velocity fields, in order to perform a full modal decomposition of flow. The velocity fields are obtained from a DNS by X. Wu at  $Re = 24,580$ , using the code described in Wu & Moin (2008). Compressive sampling is used to reduce the number of samples required to resolve the frequency content of the DNS velocity fields, and is described in chapter 3. The application of compressive sampling in wall-bounded turbulence is demonstrated for the first time in this thesis, and depends upon the approximate sparsity of the data in the frequency domain. It is shown that compressive sampling can be applied in wall-bounded turbulence if the flow fields are Fourier transformed in the homogeneous spatial (wall-parallel) directions, and extracts the right frequencies, using significantly less samples than predicted by the Nyquist criterion, when applied to flow fields with known frequency content.

The modal decomposition of turbulent pipe flow in the three spatial directions and in time is described in chapter 4, and provides a means for identifying the coherent structures and developing low-order models of the flow. A significant reduction of the data requirements to perform the modal decomposition is achieved via the use of compressive sampling and model-based radial basis functions. The radial basis functions obtained from the singular value decomposition of the resolvent capture the coherence of the structures in the wall-normal direction, thereby providing a link between the coherent structures and the physical mechanisms sustaining them. The coherent struc-

tures are represented as a superposition of propagating waves. The model highlights that the long streamwise waves are tall in the wall-normal direction and largely amplified due to non-normality effects, similarly to the global modes identified in the linearized analysis of the NS equations. The short streamwise waves are localized in the wall-normal direction and are best described using resolvent analyses. The modal decomposition allows for the identification of the most energetic modes in the  $(k, n, u_c)$  parameter space and of the relative phase of the modes which both were not predicted by the resolvent analysis of McKeon & Sharma (2010). The analysis presented in this thesis also supports the importance of criticality effects and provides an estimate of the rank of the resolvent as a function of the streamwise wavenumber.

The last chapter summarizes the new understandings of wall-bounded turbulence gained from the analysis of the two models presented in this thesis and gives some recommendations for future work.

## Chapter 2

# A Streamwise-Constant Model of Turbulent Pipe Flow

This chapter was published as Bourguignon & McKeon (2011). Reprinted with permission from Bourguignon & McKeon (2011). Copyright 2011, American Institute of Physics.

### 2.1 Introduction

A streamwise-constant model is presented in this chapter to investigate the basic mechanisms responsible for the change in mean flow that occurs during pipe flow transition. The model retains a nonlinear term, which, per the discussion in the introduction, is required to capture the blunting of the velocity profile. Streamwise-constant models describe the evolution of the three components of velocity in a plane perpendicular to the mean flow, and are equivalently referred to as 2D/3C. A streamwise-constant model for fully-developed (pipe) flow was derived Joseph (1968) and shown to be globally stable for all Reynolds numbers (also Papachristodoulou (2005)). Thus the 2D/3C model has the useful property of having a unique fixed point corresponding to the laminar flow. A stochastically forced 2D/3C model formulated in terms of a cross-stream streamfunction and the deviation of the streamwise velocity from the (linear) laminar profile, described in the Introduction, was used by Gayme *et al.* (2010) to study Couette flow. The model successfully captured both the blunting of the velocity profile and structures similar to the streamwise-elongated vortices and streaks observed in experiments. In general terms, the stochastically forced 2D/3C model exploits the large amplification of background disturbances due to the non-normality of the linearized operator described by Farrell & Ioannou (1993), which has been shown to reach a maximum for streamwise-constant disturbances (Bamieh & Dahleh, 2001).

Pipe flow is well suited for an assumption of streamwise invariance since streamwise-elongated coherent structures have been shown to play an important role during transition, e.g., Eckhardt (2008), as well as in fully developed turbulence, e.g., Kim & Adrian (1999), Morrison *et al.* (2004),

Guala *et al.* (2006), Hutchins & Marusic (2007), and Marusic *et al.* (2010). The streamwise-elongated coherent structures in pipe flow, both in the near-wall region and further from the wall, take a form dominated by quasi-streamwise vortices and streaks of streamwise velocity. A body of recent work in the literature suggests a connection between these features and studies of the linear Navier-Stokes (LNS) equations. For example, the most (temporally) amplified mode of the LNS equations, based on an energy norm, is streamwise-constant with an azimuthal wavenumber  $n = 1$  and features a pair of counter-rotating vortices, which create streaks by convecting streamwise momentum (Schmid & Henningson, 2001). Reshotko & Tumin (2001) also studied the spatial evolution of optimal disturbances in pipe flow in contrast to previous studies focusing on the temporal evolution, arguing that a spatial study is better suited for comparison with experiments in which the disturbances are growing as they convect downstream. They concluded that the most amplified disturbances are stationary and have an azimuthal wavenumber  $n = 1$ .

Additional, important support for the streamwise-constant model comes from the nonlinear study of turbulent Couette flow by Reddy & Ioannou (2000), which emphasizes the dominant role played by the streamwise-constant modes in the flow dynamics. Based on an energy transfer analysis, the latter authors showed that the streamwise-constant modes with azimuthal wavenumber  $\pm n$ , where  $n$  is an integer, dominate energy extraction from the laminar base flow using linear non-normal mechanisms, and maintain the mean turbulent flow via their nonlinear interaction. Note that the mean turbulent mode does not extract energy directly from the laminar base flow.

The laminar base flow in a pipe, which is linearly stable for all Reynolds numbers (Salwen *et al.*, 1980; Meseguer & Trefethen, 2003), becomes unstable when streamwise-constant vortices and velocity streaks are superposed due to the creation of inflection points (Meseguer, 2003), which sustain the growth of infinitesimal 3D disturbances until the streaks decay (Zikanov, 1996). Waleffe (1997) argued that the 3D disturbances can regenerate the vortices, or “rolls,” by nonlinear interaction, which consequently create the streaks by convecting streamwise momentum, leading to a self-sustaining process (SSP), which occurs across a range of shear flows. The regeneration mechanisms invoked by Waleffe (1997) were later revisited by Schoppa & Hussain (2002), who attributed the regeneration of the rolls to a mechanism involving transient growth of the streaks. In this model, the 3D infinitesimal perturbations exhibit transient growth, and evolve into sheets of streamwise vorticity which are then stretched by the mean shear and collapse, resulting in the formation of streamwise rolls. The SSP was shown to dominate the near-wall cycle in fully developed turbulence and features of the SSP are also observed in turbulent puffs occurring during pipe flow transition (van Doorne & Westerweel, 2009) and in the edge state analysis of Schneider *et al.* (2007), an alternate view of the approach to turbulence associated with the treatment of the turbulent state as a chaotic saddle in state space.

Traditionally, the later stages of transition to turbulence in pipe flow have been characterized by

the creation of puffs and slugs (Wynanski & Champagne, 1973). Puffs have been identified as the flow response to large amplitude disturbances at low Reynolds number, e.g.,  $Re \approx 2,000$ , and are characterized by a sharp trailing edge and a smooth leading edge whereas slugs are created by low amplitude disturbances at larger Reynolds number,  $Re > 3,000$  and have sharp leading and trailing edges (Wynanski & Champagne, 1973). The puffs are sustained via a SSP taking place near the trailing edge, characterized by the creation of low-speed streaks inside the puff which convect slower than the puff and create a shear layer at the boundary with the laminar flow at the back of the puff (Shimizu & Kida, 2009). The shear layer is subject to Kelvin-Helmholtz instability resulting in the creation of streamwise vortices by roll-up of vortex sheets. The streamwise vortices propagate faster than the puff and maintain the turbulence inside the puff as they re-enter it. The quasi-periodic generation of streamwise vortices near the trailing edge of the puffs, where the transition from laminar to turbulence takes place, was also reported by van Doorne & Westerweel (2009). Hof *et al.* (2010) suggested a new driving mechanism for puffs based on the formation of inflection points in the velocity profile near the trailing edge of the puff whose instability sustains turbulence inside the puff.

The clear distinction between puffs and slugs made by Wynanski & Champagne (1973) was later questioned by Darbyshire & Mullin (1995) who observed mixed occurrences of puffs and slugs. More recently, Duguet *et al.* (2010) argued that slugs are out-of-equilibrium puffs and therefore cannot exist together with stable equilibrium puffs, which are observed at  $Re \approx 2,200$  and convect slightly slower than the mean flow. Equilibrium puffs keep a constant length as they travel downstream and are separated by regions of laminar flow which are necessary to sustain them (as noticed by Lindgren (1957), see also Hof *et al.* (2010)). In general terms, equilibrium puffs represent a minimal flow unit able to sustain turbulence. The particle-image-velocimetry (PIV) measurements of Hof *et al.* (2004) confirmed that the dominant flow structures inside a puff are quasi-streamwise vortices and streaks which are independent of the method used to generate the puff (Wynanski & Champagne, 1973), and also highlighted the similarity between the travelling wave solutions of the NS equations and the velocity field near the trailing edge of a puff. At larger Reynolds number, the puffs expand as they convect downstream and tend to merge together, becoming unstable via a Kelvin-Helmholtz instability of the wall-attached shear layers (Duguet *et al.*, 2010) and resulting in the formation of slugs which keep expanding until the whole flow domain is dominated by turbulent motion.

In this chapter, a streamwise-constant model for turbulent pipe flow is presented, along with an exploration of the simplest forcing models that allow for the isolation of the basic mechanisms governing the dynamics that result in the blunting of the velocity profile. The model is described in the next section, together with the numerical methods employed to simulate the flow. In the third section, a simple, steady, deterministic forcing is used to isolate the effects of the linear and nonlinear terms, showing that the linear coupling between the in-plane and axial velocities leads to

the formation of high- and low-speed streaks (defined with respect to the laminar base flow), and that the nonlinear coupling convects the low-speed streaks towards the center of the pipe and the high-speed streaks towards to wall, resulting in the blunting of the velocity profile. The distribution of the high- and low-speed streaks over the cross-section of the pipe produced by the model is remarkably similar to one observed in the velocity field near the trailing edge of the puff structures present in pipe flow transition. In the fourth section, the response of the 2D/3C model to stochastic forcing in the cross-stream plane is described, demonstrating the generation of “streamwise-constant puffs,” so-called due to the good agreement between the temporal evolution of their velocity field and the projection of the velocity field associated with three-dimensional puffs in a frame of reference moving at the bulk velocity. The main achievements obtained with the 2D/3C model for pipe flow are summarized at the end of this chapter.

## 2.2 Description of the Model and Numerical Methods

The streamwise-constant model of turbulent pipe flow is derived from the NS equations written in cylindrical coordinates under the assumption of streamwise invariance, i.e., it constitutes a projection of the NS equations onto the streamwise direction. We employ a nondimensionalization based on the pipe radius  $R$  and the bulk velocity  $\bar{U}$ , i.e.,  $r \in [0, 1]$ ,  $\tau = \frac{\bar{U}t}{R}$  and  $Re = \frac{2R\bar{U}}{\nu}$ . Continuity is enforced via the introduction of a dimensionless streamfunction  $\Psi$  whose evolution equation is obtained by taking the curl of the NS equations projected in the axial direction. The model consists of a forced evolution equation for the streamfunction, from which the radial and azimuthal velocities can be derived, and an evolution equation for the axial velocity in terms of the deviation from the laminar profile corresponding to the axial momentum balance, subject to boundary conditions of no-slip and no-penetration on the wall of the pipe. The deviation of the local axial velocity from laminar illustrates how the flow evolves away from the laminar state and is defined as

$$u(r, \theta) = \tilde{u}(r, \theta) - U(r), \quad (2.1)$$

where  $\tilde{u}(r, \theta)$  is the instantaneous axial velocity and  $U(r) = 1 - r^2$  is the laminar base flow.

The 2D/3C model was first derived by Joseph (1968) and is written as follows for the cylindrical coordinate system shown in figure 2.1:

$$\begin{cases} \frac{\partial \Delta \Psi}{\partial \tau} = \frac{2}{Re} \Delta^2 \Psi + \mathcal{N}_\psi, \\ \frac{\partial u}{\partial \tau} = C_p - \frac{1}{r} \frac{\partial \Psi}{\partial \theta} \frac{\partial U}{\partial r} - \frac{1}{r} \frac{\partial \Psi}{\partial \theta} \frac{\partial u}{\partial r} + \frac{1}{r} \frac{\partial \Psi}{\partial r} \frac{\partial u}{\partial \theta} + \frac{2}{Re} \Delta u, \\ \Psi|_{r=1} = \frac{\partial \Psi}{\partial r}|_{r=1} = 0, \end{cases} \quad (2.2)$$

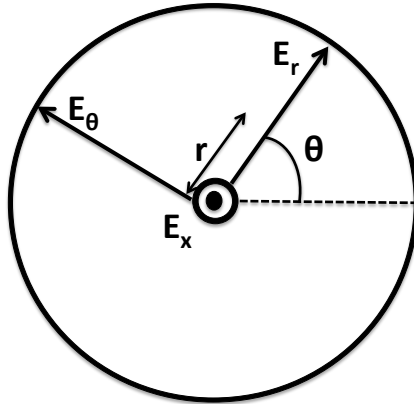


Figure 2.1: The coordinate system used to project the Navier-Stokes equations.

where  $\Delta = \frac{1}{r} \left( \frac{\partial}{\partial r} \left( r \frac{\partial}{\partial r} \right) + \frac{1}{r} \frac{\partial^2}{\partial \theta^2} \right)$  is the 2D Laplacian. The radial and azimuthal velocities are defined by  $u_r = \frac{1}{r} \frac{\partial \Psi}{\partial \theta}$ ,  $u_\theta = -\frac{\partial \Psi}{\partial r}$ . Only the streamfunction equation is forced, based on the results of the study by Jovanovic & Bamieh (2005) which showed that maximum amplification is obtained by forcing in the cross-sectional plane in the linearized NS equations. Thus  $\mathcal{N}_\psi$  represents a forcing term that is required to maintain the perturbation energy in an otherwise stable system, and can be considered to represent “noise” that is always present in experiments, e.g., wall roughness, vibrations, non-alignment of the different sections of the pipe, thermal effects, as well as taking into account the effects not modeled by the streamwise invariance approximation. In the subsequent sections, we consider two of the simplest possible forms for  $\mathcal{N}_\psi$  in order to investigate the origin of the blunting of the mean velocity profile. The nonlinear terms in the governing equation for the streamfunction are neglected in order to obtain the simplest model able to capture the blunting of the velocity profile and also because their effects can be incorporated into the unstructured forcing term  $\mathcal{N}_\psi$ . Moreover the study of Gayme *et al.* (2010) showed that there are no significant differences in the Couette flow statistics obtained from the model based on a linearized streamfunction equation compared to the fully nonlinear 2D/3C model. The bulk velocity is maintained constant by adjusting the pressure gradient  $C_p$ , i.e., the Reynolds number is held constant for each study. The streamwise velocity behaves as a passive scalar convected by the in-plane velocities.

The 2D/3C model with stochastic forcing is discretized using a spectral-collocation method based on Chebyshev polynomials in the radial direction and Fourier modes in the azimuthal direction, associated with a third-order semi-implicit time stepping scheme described in Spalart *et al.* (1991). The singularity at the origin of the polar coordinate system is avoided by re-defining the radius from  $-1$  to  $1$  and using an even number of grid points in the radial direction (Heinrichs, 2004). Three Sylvester equations are written respectively for  $\Delta \Psi$ ,  $\Psi$ , and  $u$ , associated with homogeneous Dirichlet boundary conditions, and are solved using a Fortran code relying on an optimized Sylvester equation solver from the SLICOT numerical library (Jonsson & Kagstrom, 2003). The boundary conditions

(BCs)  $\Psi = 0$  and  $u = 0$  at the wall correspond respectively to no-penetration and no-slip in the axial direction. The no-slip BC in the azimuthal direction is enforced by adding particular solutions to the streamfunction, following the influence matrix method for linear equations (Peyret, 2002), such that the azimuthal velocity  $u_\theta = -\frac{\partial\Psi}{\partial r}$  vanishes at the wall. Under deterministic forcing, the 2D/3C model is reduced to a set of two ordinary differential equations that are solved in Matlab using spectral methods based on a Chebyshev polynomial expansion.

## 2.3 Simplified Streamwise-Constant Model with Deterministic Forcing

We begin by developing a simplified version of the 2D/3C model subject to a steady, deterministic forcing to study momentum transfer between the in-plane and axial velocities. The study of optimal disturbance growth in pipe flow by Schmid & Henningson (2001) demonstrated that the streamwise-constant mode with azimuthal wavenumber  $n = 1$  is the most amplified based on an energy norm. Thus we isolate this mode as a candidate perturbation contributing to the blunting of the velocity profile and consider a forcing with only this one mode in the azimuthal direction, namely

$$N_\psi = N(r) \sin \theta. \quad (2.3)$$

The streamfunction  $\Psi(r, \theta)$  has the same azimuthal dependence as the forcing since its governing equation is linear, i.e.,  $\Psi = \Psi_1(r) \sin \theta$ . The axial velocity can be written in terms of a mean deviation from laminar  $u_0$  and a zero-mean perturbation  $u_1 \cos \theta$  corresponding to the linear response of the system to the forcing,

$$u(r, \theta) = u_0(r) + u_1(r) \cos \theta. \quad (2.4)$$

The 2D/3C model can be simplified as follows to predict the steady state mean deviation from laminar,  $u_0$ , obtained with the deterministic forcing profile  $N(r)$ :

$$\left(\Delta_r - \frac{1}{r}\right)^2 \Psi_1 = -0.5 Re N(r), \quad (2.5)$$

$$\left(\Delta_r - \frac{1}{r}\right) u_1 = 0.5 Re \Psi_1 d_r (U + u_0), \quad (2.6)$$

$$\Delta_r u_0 = -0.5 Re (C_p r - d_r (\Psi_1 u_1)), \quad (2.7)$$

where  $\Delta_r = r d_{rr} + d_r$  is the radial derivative component of the 2D Laplacian, and  $d_r = \frac{d}{dr}$ . In order to obtain the simplest model able to capture the blunting of the velocity profile, we can linearize equation (2.6) under the assumption of small amplitude forcing. The resulting model contains only one nonlinear term in one ODE, the other two ODEs being linear. The presence of at least one

nonlinear term is required to obtain a change in mean flow since linear models always give the same mean flow as the one used for the linearization.

A simple inspection of equations (2.5) - (2.7) leads to the following observations. Conclusions similar to those of Reddy & Ioannou (2000) on the energy transfer between streamwise-constant modes can be recovered, but this time in terms of momentum transfer and for the pipe instead of Couette flow: the mean turbulent mode  $u_0$  cannot extract momentum from the laminar base flow and is sustained by the nonlinear interaction between the axial velocity perturbation  $u_1$  and the streamfunction  $\Psi_1$ , i.e., the  $d_r(\Psi_1 u_1)$  term in equation (2.7). The non-normality of the system manifests itself in the linear coupling between the laminar base flow and the streamfunction which amplifies the disturbances and generates the axial velocity perturbation  $u_1$  by convection of streamwise momentum (see equation (2.6)). The shape of the streamfunction determines the amount of blunting obtained for a given amplitude coefficient.

In order to advance further analytically, we write the streamfunction profile  $\Psi_1$  as a Taylor series at the origin, i.e.,

$$\Psi_1 = \sum_{i=0}^{\infty} \alpha_i r^i, \quad (2.8)$$

and set  $\alpha_0 = 0$  in order to enforce continuity in the limit of  $r$  tending to zero, recalling that  $\Psi(r, \theta) = -\Psi(r, \theta + \pi)$ . The forcing profile generating  $\Psi_1$  is given by

$$N(r) = -\frac{1}{Re} \left( \partial_r + \frac{1}{r} \partial_r - \frac{1}{r^2} \right)^2 \Psi_1(r). \quad (2.9)$$

We rescale the coefficients  $\alpha_i$  by  $\alpha_1$ , i.e.,  $\Psi_1 = \alpha_1[r + \alpha_2 r^2 + \alpha_3 r^3 + \alpha_4 r^4 + \dots]$ , and choose  $\alpha_1$  such that the change in mean flow induced by the forcing has the same amplitude at its maximum as in the experiments of den Toonder & Nieuwstadt (1997) at the same Reynolds number, in order to facilitate comparison of the results. Note that, depending on the streamfunction profile, the coefficient  $\alpha_1$  is not necessarily small in which case the linearization of equation (2.6) is no longer justified. In the following, we solve the nonlinear momentum balance for  $u_1$  (equation (2.6)) regardless of the amplitude of  $\alpha_1$ . A fundamental streamfunction profile  $\Psi_1 = \alpha_1(r - 3r^3 + 2r^4)$  is obtained by truncating the series expansion to the fourth-order term, enforcing the BCs  $\Psi_1 = \frac{d\Psi_1}{dr} = 0$  at the wall, and requiring that the forcing be bounded at the origin.

Streamfunctions given by  $\Psi_{1,a} = \Psi_1$ ,  $\Psi_{1,b} = \Psi_1^2$  and  $\Psi_{1,c} = \Psi_1^3$  were investigated in order to ascertain the ability of such simple functions to capture key aspects of the blunting of the mean profile and to identify the role of the radial streamfunction profile. The amplitude coefficients,  $\alpha_1$ , were chosen such that the same amount of blunting is realized in each case, as described above in terms of the maximum deviation from laminar. The steady-state equations were solved with 64 grid points in the radial direction, and at a Reynolds number of 24,600, matching one of the pipe

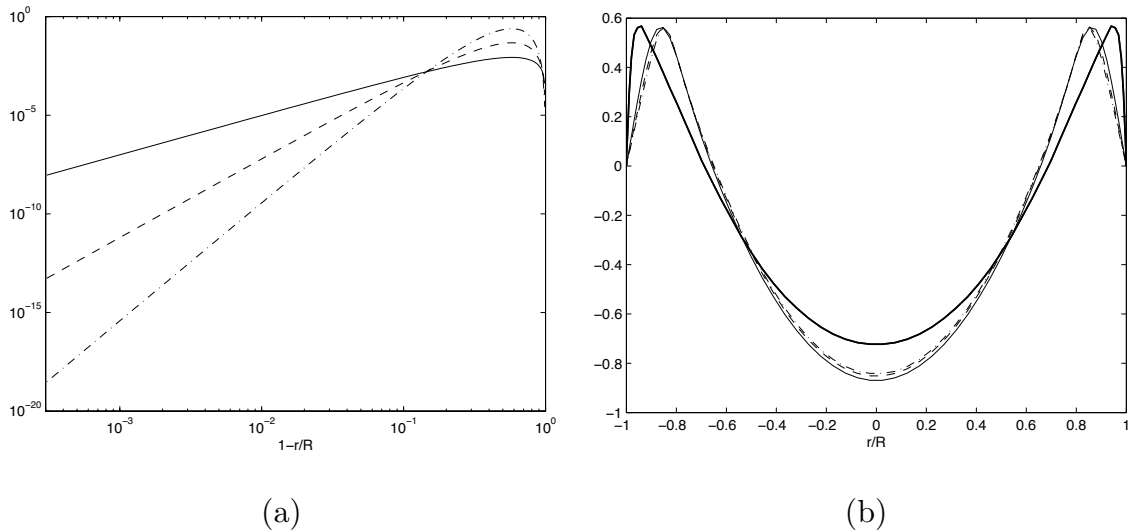


Figure 2.2: (a) Streamfunctions  $\Psi_{1,a-c}(r)$  and (b) corresponding velocity profiles  $u_0(r)$  for  $\Psi_{1,a}(r) = 0.033(r - 3r^3 + 2r^4)$  (thin solid),  $\Psi_{1,b}(r) = 0.7(r - 3r^3 + 2r^4)^2$  (dashed),  $\Psi_{1,c}(r) = 14(r - 3r^3 + 2r^4)^3$  (dash-dot) and experimental velocity profile of den Toonder & Nieuwstadt (1997) at  $Re = 24,600$  (thick solid).

flow experiments of den Toonder & Nieuwstadt (1997). A short convergence study showed that this resolution in the radial direction is sufficient since the maximum relative error compared to the solution computed on 192 grid points is less than one percent.

Figure 2.2 shows the radial forms of the three analytic streamfunctions,  $\Psi_{1,a-c}$ , and the respective resulting variations of the mean deviation from laminar. Streamfunction profiles  $\Psi_{1,b}$  and  $\Psi_{1,c}$  reach maximum amplitudes of about 0.05 and 0.25, respectively, in the core of the pipe, while in comparison  $\Psi_{1,a}$  is relatively flat with a maximum amplitude of 0.0085. Despite such a wide variation in streamfunction amplitude between the three cases, the streamwise velocity profiles are remarkably similar. Even the simple streamfunction profile  $\Psi_{1,a}$  leads to a “good” blunting of the velocity profile, in the sense that the general features of the mean profile are reproduced. The maxima of the velocity profiles are situated further from the wall compared to the experimental data (den Toonder & Nieuwstadt, 1997), which likely corresponds to the neglect of the influence of the small scales near the wall by the streamwise-constant model. The results obtained with the simplified 2D/3C model also show that the velocity profile is relatively independent of the radial shape of the forcing and streamfunction, i.e., the profile can be said to be robust to the shape of the streamfunction.

The in-plane kinetic energy, defined as the integral of  $\frac{u_r^2}{2} + \frac{u_\theta^2}{2}$  over the pipe cross section, varies from  $3.7 \cdot 10^{-4}$  for  $\Psi_{1,a}$  to 0.31 for  $\Psi_{1,c}$  even though the same amount of blunting is realized by the three streamfunctions  $\Psi_{1,a-c}$ . This large variation of the in-plane kinetic energy between different streamfunctions (about 3 orders of magnitude) can be understood by consideration of the influence

of the near-wall region in the pipe on the overall amplification. Amplification is proportional to the mean shear and surface area, which are both maximum at the wall. Hence, the streamfunction  $\Psi_{1,c}$  having a small amplitude near the wall compared to  $\Psi_{1,a}$  (see figure 2.2) does not benefit from the near-wall effects as much as  $\Psi_{1,a}$  and needs to reach a larger amplitude in the core (about 30 times larger) in order to give the same amount of blunting as  $\Psi_{1,a}$ , resulting in a significantly larger in-plane kinetic energy.

The large amplitude reached by  $\Psi_{1,c}$  in the core of the pipe results in a maximum radial velocity amplitude of 64% of the bulk velocity compared to 3.3% for  $\Psi_{1,a}$ , significantly larger than the radial velocity turbulence intensity measured by den Toonder & Nieuwstadt (1997) which is about 1 plus unit or equivalently about 5% of the bulk velocity. A streamfunction that maintains a forcing amplitude comparable to the experimental noise level should therefore have a larger amplitude near the wall and relatively constant amplitude over the whole domain. A similar conclusion can be obtained by considering that blunting results from the advection of axial momentum by the radial velocity so that a large amount of blunting is realized when large radial velocities are present. Taking into account that the radial velocity depends on the azimuthal velocity via the continuity constraint, it can be seen that maximization of the ratio  $|\frac{u_r}{u_\theta}| = |\frac{\Psi}{rd_r\Psi}|$  suggests that the flattest streamfunction profile (or equivalently the simplest radial dependence) results in the largest amplification. In terms of structures, the largest structures corresponding to the modes with the least zero crossings in the radial direction are more able to redistribute momentum over the cross-section of the pipe. The importance of the modes with the least zero crossings is a known feature of turbulent pipe flow: modes with a radial quantum number of 1 in the study of Dugdale *et al.* (2007) were shown to capture most of the energy in their dynamical eigenfunction decomposition of turbulent pipe flow. Likewise, the singular modes that are most amplified in the study of McKeon & Sharma (2010) exhibit the lowest number of zero crossings.

Based on our numerical study, the streamfunction  $\Psi = 0.033(r - 3r^3 + 2r^4)\sin\theta$  leads to a blunting of the velocity profile whose maximum amplitude matches the experimental data at the same Reynolds number and is generated by a forcing profile  $N(r) = -90/Re$  that is constant in the radial direction and whose amplitude over the pipe cross-section is consistent with the experimentally measured rms amplitude of the turbulence fluctuations. The contours of the streamfunction  $\Psi = 0.033(r - 3r^3 + 2r^4)\sin\theta$  are plotted in figure 2.3 together with a vector plot of the corresponding in-plane velocities and the resulting contours of the axial velocity field. The streamfunction exhibits two counter-rotating rolls which advect the mean shear to create a low- and a high-speed streak of axial velocity defined with respect to the laminar base flow. The high-speed streak sits near the wall, whereas the low-speed streak is localized near the centerline. Hence, the flow is on average faster near the wall and slower at the center as is the case for the velocity profile of turbulent pipe flow. The amplification factor between the in-plane and streamwise velocities, defined as the ratio

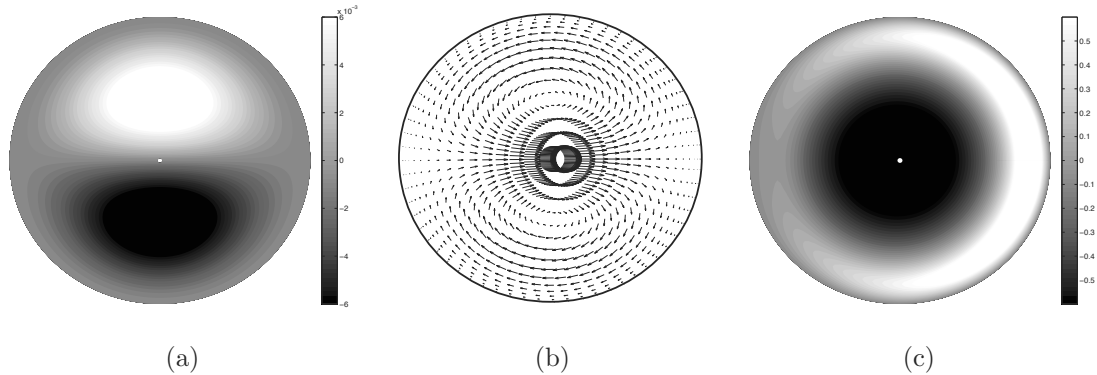


Figure 2.3: Model output for deterministic forcing: (a) contours of the streamfunction  $\Psi = 0.033(r - 3r^3 + 2r^4)\sin\theta$ , (b) vector plot of the corresponding in-plane velocities, and (c) contours of the resulting axial velocity field.

of the extrema, is about 20 in this case.

As a final comment related to this simple, steady, deterministic streamfunction analysis, we note that when the azimuthal wavenumber is chosen to match the azimuthal dependence of the spatial puffs observed by Hof *et al.* (2004) and a new streamfunction model is derived along the lines described above, the velocity fields produced by our model are remarkably similar to the measured velocity fields near the trailing edge of the puffs. For an azimuthal wavenumber equal to six, the lowest-order streamfunction profile that satisfies the BCs and is generated by a forcing profile bounded at the origin is given by  $\Psi_6 = \alpha_1(r^4 - 2r^5 + r^6)$ ; figure 2.4 shows the resulting variation of the axial velocity. The wall-normal position of the high- and low-speed axial velocity streaks compares well with figure 2 (E),(F) in the paper by Hof *et al.* (2004). Moreover our model appears to capture the merging of the low-speed streaks and their congregation near the center of the pipe which is observed in experiments (Hof *et al.*, 2004) but is not present in the traveling wave solutions of the NS equations.

Despite the simplicity of the deterministic streamfunction profiles described in this section, key aspects of the axial velocity variation observed in experiments are recovered. In the following section, we consider a more realistic, time-dependent forcing function in an effort to capture more details associated with the mechanisms of momentum transfer.

## 2.4 Stochastic Forcing of the Streamwise-Constant Model

Effects that are not captured by the (unforced) 2D/3C model and external perturbations that are always present in experiments but not explicitly described by the NS equations are likely much better captured by a stochastic forcing than a deterministic one. In this section, we present the results from a simulation of the 2D/3C model forced by small amplitude white noise, an approach

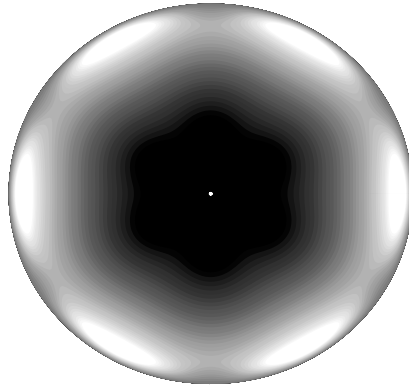


Figure 2.4: Contours of the axial velocity induced by the streamfunction  $\Psi_6(r, \theta) = (r^4 - 2r^5 + r^6) \sin(6\theta)$ , the light and dark filled contours correspond to regions of the flow respectively faster and slower than laminar.

which was successfully explored by Gayme *et al.* (2010) in Couette flow as well as several previous linear studies. Such stochastic forcing has the advantage over deterministic forcing of not relying on any assumption regarding the spatial and temporal dependence of the perturbations, such that the resulting velocity field reflects the direction of maximum (assumed dominant) disturbance amplification. The noise,  $N_\psi$ , is applied at each grid point in space and at every time step and follows a normal distribution with zero mean and a variance that depends on the radius such that the variance per surface area is constant. In order to prevent aliasing in the nonlinear coupling terms in the streamwise velocity equation, we truncate the 2D Fourier transform of the forcing term after the lowest two-third wavenumbers, as described in Canuto (2006).

Representative time traces of the centerline velocity for two different Reynolds numbers are reproduced on figure 2.5 and show numerous sharp drops which we identify as the signature of “streamwise-constant puffs” before increasing smoothly nearly back to its laminar value. (Since there is no grid point at the centerline, we approximate the centerline velocity by averaging the axial velocity in the azimuthal direction over the grid points closest to the center of the pipe.) The signatures of the “streamwise-constant puffs” are remarkably similar to the spatial evolution of the centerline velocity from the trailing to the leading edge of the spatial puffs in the numerical simulations of Shimizu & Kida (2009). We define a puff generation timescale as the time elapsed between two sharp drops of the centerline velocity. At  $Re = 2,200$ , the timescale is about 75 dimensionless time units based on the pipe radius and compares well with the timescale of puffs computed from experimental data (Nishi *et al.*, 2008), in which the puffs are 5 to 20 diameters long depending on Reynolds number and convect at nearly the bulk velocity. A puff of length  $20D$  which is separated from the next puff by a laminar region of length equivalent to one puff would lead to a dimensionless timescale based on the pipe radius of 80.

The puff generation timescale is an increasing function of the Reynolds number, reflecting the

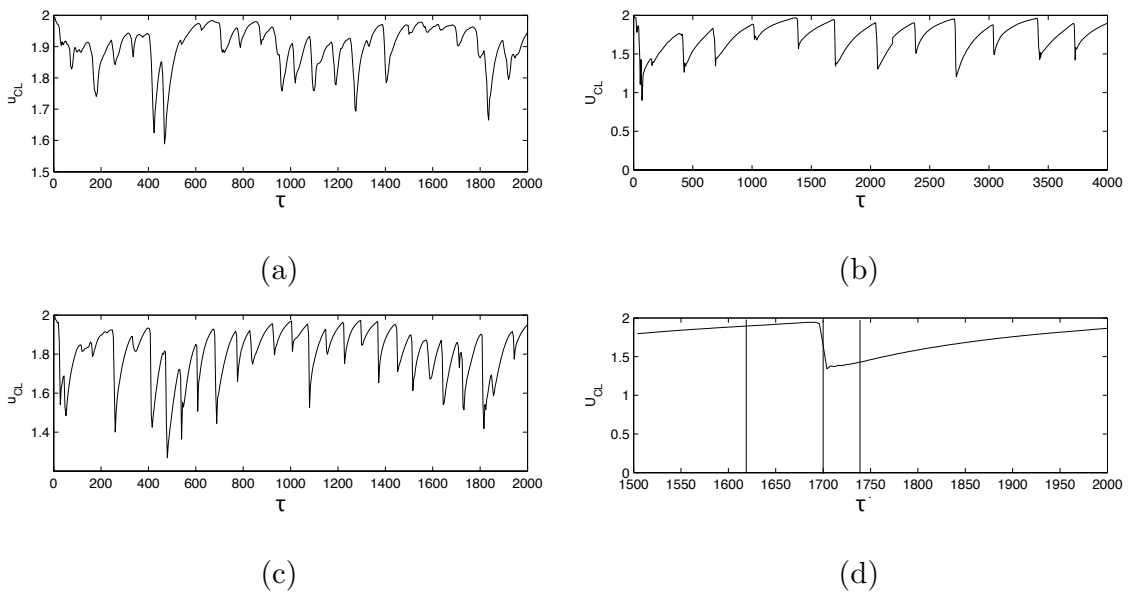


Figure 2.5: Time traces of the centerline velocity from three different simulations respectively at  $Re = 2, 200$  with 0.0005 and 0.002 rms noise levels (a), (c) and at  $Re = 10, 000$  with 0.002 rms noise level (b). The resolution in the radial direction is  $N = 48$ . (d) Zoom on the time interval during which the samples of figure 2.6 are taken. The vertical lines indicate the sampling instants.

fact that puffs tend to be longer in experiments as the Reynolds number increases figures 2.5(a),(b), reaching 330 at  $Re = 10, 000$ , but is relatively independent of the noise amplitude figures 2.5(a),(c). The drop in centerline velocity associated with the trailing edge of a puff can be observed to be sharper and stronger for larger forcing amplitudes. Note that if we relax the BCs to allow for slip in the azimuthal direction, i.e., we use a shear-stress free condition (not shown), the simulations capture the creation of streamwise vortices and streaks as well as the blunting of the velocity profile, but we do not observe clearly the cyclic generation of puffs in the time evolution of the full velocity field or their signature in the time traces of the centerline velocity. However, for a given forcing amplitude, the amount of blunting realized with the slip BC in the azimuthal direction is larger than with no-slip.

The time evolution of the flow field is characterized by the quasi-periodic generation of “streamwise-constant puffs” followed by their decay and the return of the flow close to the laminar state, i.e., each bursting event is followed by quiescent flow equivalent to the laminar regions that separate the puffs in the experiments of Lindgren (1957). The three main stages in the evolution of the flowfield corresponding to a “streamwise-constant puff” are plotted on figure 2.6 in terms of the axial velocity ((a) to (c)) and the swirling strength ((d) to (f)), defined as the magnitude of the imaginary part of the in-plane velocity gradient eigenvalues and representative of coherent vorticity without the influence of mean shear. These instantaneous fields correspond to the time instants

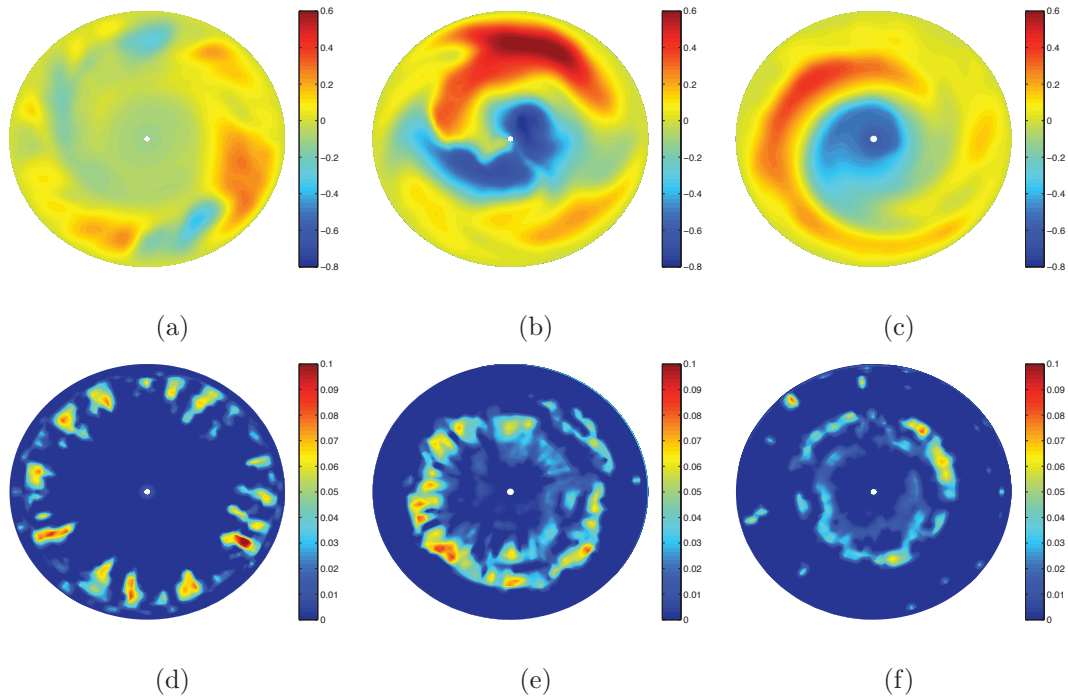


Figure 2.6: Contours of the axial velocity, subfigures (a) to (c), and of the swirling strength for the in-plane velocities, subfigures (d) to (f), computed respectively at  $\tau = 1620$ ,  $\tau = 1700$ , and  $\tau = 1740$  dimensionless time units.

marked with vertical lines in figure 2.5(d). During the first stage, patches of swirl move toward the center of the pipe figures 2.6(d),(e) and create streaks by convection of the axial momentum figure 2.6(a). The radial motion of the coherent swirl corresponds to a lift up of streamwise vortices away from the wall as observed in the simulations of van Doorne & Westerweel (2009) if we consider the evolution of the vorticity field projected in a plane moving at the bulk velocity. The second stage consists of the segregation of the high- and low-speed streaks, the latter being convected toward the center of the pipe, resulting in the blunting of the velocity profile characteristic of turbulent pipe flow, figure 2.6(b). Once a low-speed streak reaches the center, the centerline velocity drops sharply, as can be seen on the time traces on figure 2.5(b). Finally the swirling strength and streaks decay figures 2.6(c),(f) and the flow returns close to the laminar state before the next cycle starts. As the streamwise vortices convect toward the center of the pipe, the sign of the net azimuthal velocity is reversed such that the rotation sign changes from one cycle to the next.

While the output of the 2D/3C model is a temporal variation of a streamwise constant field, a simplistic comparison with spatial experimental results may be made by assuming an appropriate convection velocity to be the bulk velocity. With this in mind, the time evolution of the velocity field is remarkably similar to the flow visualizations by Hof *et al.* (2004) in transitioning pipe flow when a puff is observed in a reference frame moving with the bulk velocity. Streak merging in experiments

was reported by those authors, who showed that the number of streaks in the cross-section decreases due to their merging as the cross-stream observation plane is moved from the trailing edge to the leading edge of a puff. This streak merging, as well as the segregation of the high- and low-speed streaks observed in the experiments is accurately reproduced by the model, as shown in figure 2.5. The time evolution of the vorticity field in our simulations is also consistent with the projection of the three-dimensional vorticity field inside the puff computed by van Doorne & Westerweel (2009) in a plane moving at the bulk velocity, characterized by a lift up of streamwise vortices away from the wall as we move from the trailing to the leading edge of the puff (corresponding to increasing time in our model).

The generation and subsequent decay of the puffs can be described in terms of a simple process driven by background noise, sketched in the inner loop of figure 2.7. In essence, the presence of background noise in the pipe cross-section results in the formation of streamwise-constant vortices which advect axial momentum to create high- and low-speed streaks of axial velocity. The vortices interact nonlinearly with the streaks to segregate them, i.e., to convect the low-speed streaks toward the center and the high-speed streaks toward the wall, leading to the blunting of the velocity profile. We term this a “quasi-self-sustaining process” (QSSP) to reflect the fact that, while there is no feedback from the axial velocity to the evolution of the streamfunction (denoted by the dashed line in the inner loop of figure 2.7) which could sustain the cycle described in figure 2.6, the insertion of small-amplitude stochastic forcing in the cross-stream plane appears to provide an effective replacement for this mechanism. The radial shape of the forcing is directly related to the amount of swirl present in the simulations and therefore suggests a method to control the flow by shaping the noise forcing in the spirit of the simple control mechanism developed by Hof *et al.* (2010) which reduces the inflection points of the velocity profile and leads to a relaminarization of the flow.

A well-studied, fully self-sustaining process has been described for the (3D/3C) NS equations by Waleffe (1997), which relies on the nonlinear interaction of the disturbances developing from the instability of the streaks to force the streamwise vortices. Our results suggest that the blunting of the velocity profile can be considered to be, in essence, a nonlinear, two-dimensional phenomenon in which the directional amplification of the 2D/3C model selects the appropriate disturbance shape from stochastic forcing in order to maintain the QSSP. The model suggests that the sustaining mechanisms are therefore insensitive to the type of (nonlinear) interaction invoked to force the streamwise vortices. Based on the simulations presented here, we argue that it is the presence of appropriate, small disturbances in the flow (necessarily contained in the white noise of stochastic forcing), and not their specific interaction that sustains the streamwise vortices and streaks. Hence, the 2D/3C model shows that using unstructured (stochastic) forcing to generate the streamwise vortices appears to be sufficient to capture the formation of the streaks and their segregation resulting in a blunting of the velocity profile and that the overall flow dynamics are relatively insensitive to the particular

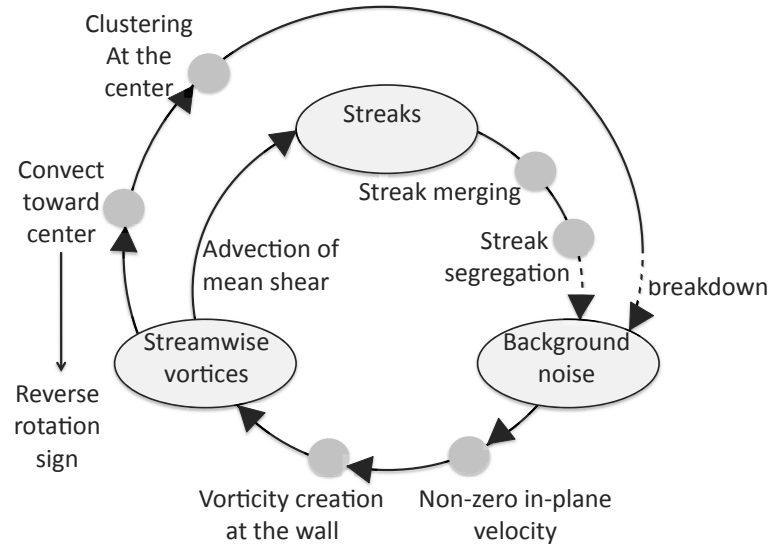


Figure 2.7: Diagram detailing the different stages of the QSSP. The dashed lines represent unmodeled effects.

regeneration process invoked to produce the streamwise vortices. The QSSP is simpler than other processes described in the literature but does appear to capture the minimum turbulence dynamics and produce flow fields dominated by streamwise vortices and streaks whose temporal evolution and topology compares well to experimental visualizations and numerical simulations of puffs, under an appropriate projection onto a plane convecting at the bulk velocity. In addition, our simulations are significantly less computationally intensive than studies of the full NS equations (Shimizu & Kida, 2009; van Doorne & Westerweel, 2009) since our domain is 2D and we do not need to track the position of the puffs in time.

Interestingly, our simulations of the stochastically forced 2D/3C model for pipe flow do not reach fully developed turbulence, regardless of the amount of forcing and Reynolds number, even though the same model applied to Couette flow and described in Gayme *et al.* (2010) reached a steady state with a velocity profile in good agreement with the profiles from full 3D simulations at the same Reynolds number, provided that the amount of forcing is appropriately chosen. Mellibovsky *et al.* (2009) describe pipe flow transition as a two-stage process, the first stage consists in the formation of the puffs and the second in their spreading in space. Those authors argue that the two stages are caused by different instability mechanisms. Our simulations support this point of view since we are able to capture the first stage using a streamwise-constant model but not the second stage for which three-dimensional effects are necessary to allow for the puffs to destabilize and form slugs which will expand to cover the whole flow domain.

## 2.5 Summary

A globally-stable, streamwise-constant model of turbulent pipe flow was investigated, and subject to two types of very simple forcing profiles, namely a deterministic, steady streamfunction and stochastic forcing of the streamfunction equation. By retaining only the nonlinearity coupling the cross-plane streamfunction and the axial velocity, the model permits the study of the physics underlying momentum transfer. This model, which is significantly more tractable than the full Navier-Stokes equations, appears to be capable of capturing key features associated with transition to turbulence, i.e., the blunting of the velocity profile and the generation of streamwise vortices and streaks.

Using the simplest, time-invariant deterministic forcing, the velocity profile was shown to be robust with respect to variations in the forcing profile, and to produce realistic velocity fields that are remarkably similar to the flow visualizations by Hof *et al.* (2004) near the trailing edge of a puff. Thanks to the significant reduction in complexity associated with the 2D/3C projection compared to the full Navier-Stokes equations, several observations can be made by examination of the governing equations: momentum is extracted from the laminar base flow by (zero-mean) perturbations via linear non-normal mechanisms and redistributed via nonlinear interactions of the perturbations to result in a change in mean flow. Hence, the simplistic model allowed for the isolation of the basic mechanisms leading to the blunting of the velocity profile in pipe flow.

Under stochastic forcing, the model generates “streamwise-constant puffs” at a frequency that depends on the Reynolds number but not on the forcing amplitude. The model captures the first stage of pipe flow transition as described in Mellibovsky *et al.* (2009), i.e., the formation of puffs, but not the second stage (spreading of the puffs in space) for which some three-dimensional effects are necessary. The time evolution of the velocity fields produced by the simulations is remarkably similar to flow visualizations in transitioning pipe flow (Hof *et al.*, 2004) when a puff is observed in a reference frame moving at the bulk velocity. The segregation of the high- and low-speed streaks observed in experiments is accurately captured by the model as well as the streak merging and the lift up of the streamwise vortices away from the wall.

The essential dynamics governing the generation of puffs in pipe flow transition were captured by the streamwise-constant model and are relatively insensitive to the particular regeneration mechanisms invoked to produce the streamwise vortices, permitting the introduction of a “quasi-self-sustaining process” to describe the generation of puffs and the blunting of the mean velocity profile.

## Chapter 3

# Efficient Representation of Wall-Bounded Turbulence Using Compressive Sampling

### 3.1 Introduction

The frequency spectrum of wall-bounded turbulence measured locally in space is known to be broadband. For that reason, numerous samples need to be acquired to resolve the frequency content of the flow and, usually, to satisfy the Nyquist criterion. Most of the samples are, in fact, just needed to resolve the high-frequency, low-energy modes of the flow, to prevent their aliasing onto lower frequency modes. The main objective of this chapter is to present and validate a technique, called compressive sampling, to extract the most energetic frequency modes in wall-bounded turbulence, using significantly less samples than predicted by the Nyquist criterion. This particularly efficient technique makes possible the full modal decomposition of turbulent pipe flow in the three spatial directions and in time, described in the next chapter, by drastically reducing the data storage and post-processing requirements.

When a sinusoidal signal of frequency  $f_0$  is sampled periodically at a rate  $f_s$ , all the sinusoids of frequency  $|f_0 - Nf_s|$ , where  $N$  is an integer, fit the samples, and are called aliases of the fundamental signal. Bilinskis (2007) suggested that aliasing effects can be eliminated by sampling randomly in time, because the aliases do not fit the randomized samples. Randomized sampling thereby provides a way, by sampling at a lower rate than predicted by the Nyquist criterion, to reduce the number of samples required for perfect reconstruction of the signal. However, if a Fast Fourier Transform (FFT) is used to extract the frequency content of the samples, fuzzy aliasing (i.e., aliasing that is more diffuse than in the case of periodic sampling) will occur, because the Fourier basis functions are not orthogonal on the set of randomized samples. Bilinskis (2007) described several techniques to remove, or at least attenuate, fuzzy aliasing when a FFT is applied to non-periodic samples. If

the signal happens to be sparse in the frequency domain, a compact representation can be efficiently obtained by applying compressive sampling, instead of using a FFT and correcting for fuzzy aliasing. In this chapter, it is shown that, if wall-bounded turbulence is decomposed as a sum of propagating waves (corresponding to Fourier modes in the streamwise and azimuthal directions, and in time), as explored by McKeon & Sharma (2010), a compact representation can be found, by applying compressive sampling to identify the dominant frequencies of the most energetic spatial Fourier modes.

Compressive sampling has been successfully applied to approximately sparse signals in the temporal domain, e.g., for data compression, and in the spatial domain, mainly for image processing, to decrease the data storage and postprocessing requirements, see for example Candès *et al.* (2006), Lustig *et al.* (2007), Candès & Wakin (2008). However, the broadband spectrum observed in wall-bounded turbulence based on spatially localized spectral measurements has previously presented a barrier to the use of compressive sampling which requires sparsity for efficient performance.

Compressive sampling consists of acquiring randomly in time (or space) a signal that is approximately sparse in the frequency domain (respectively in wavenumber space), and reconstructing it by solving a constrained minimization problem. In this thesis, a signal is defined to be sparse if most of its energy is concentrated in a few basis functions (frequencies), typically 5 or less, implying that a compact representation of the signal can be obtained by truncating its series representation, keeping only the most energetic basis functions. This definition of sparsity corresponds to “approximate sparsity” in the compressed sensing literature. A temporal Fourier basis is chosen to reconstruct the signal as it is known that, for statistically steady signals, the Fourier basis is optimal in the sense that it maximizes the energy captured for a given number of basis functions (Liu *et al.*, 2001; Berkooz *et al.*, 1993).

The Fourier coefficients to reconstruct the signal are obtained by solving a constrained minimization problem. The constraints enforce that the reconstructed signal matches the input signal at the sampling time instants. The minimization problem is based on the  $\ell_1$ -norm of the signal, defined as the sum of the absolute value of its coefficients. Chen *et al.* (1998) mention that the  $\ell_1$ -norm is particularly adapted to sparse signals as, among all the solutions that meet the constraints, it favors one with a few large coefficients and a lot of small coefficients. The  $\ell_1$ -norm is also convex, implying that the minimization problem can be solved as a convex optimization problem (Chen *et al.*, 1998), for which a unique solution exists, provided that the signal is sparse and that the number of samples is large enough (Candès *et al.*, 2006).

The number of samples,  $N_s$ , required for perfect reconstruction of a signal can be estimated using an empirical relationship by Tropp *et al.* (2010), henceforth referred to as the sparsity relationship,

$$N_s \geq 1.7 K \log \left( \frac{\Omega}{K} + 1 \right), \quad (3.1)$$

where  $K$  is the number of frequencies present in the approximately sparse signal and  $\Omega$  the bandwidth or ratio of the highest to lowest frequency of interest. The empirical relationship indicates that the number of samples increases with the signal bandwidth and the number of sparse frequencies. The numerical constant 1.7 results from a linear regression on the experimental data obtained by Tropp *et al.* (2010), and may be problem specific. The number of samples scales as the logarithm of the input signal bandwidth, in contrast to the linear scaling associated with periodic sampling, implying that a significant reduction of the number of samples required to reconstruct the signal can be obtained for broadband signals containing only a few sparse frequencies.

In practical application of the compressive sampling technique to a randomly sampled signal, the input frequency range for the constrained minimization problem should be chosen such that the sparsity relationship is satisfied (equation (3.1)). The minimum and maximum frequencies (Fourier modes) used to reconstruct the signal can, respectively, be lower than the inverse of the sampling duration and higher than the mean sampling rate. In contrast, in the case of periodic sampling, the minimum and maximum frequencies of the Fourier series representing the input signal are directly related to the sampling parameters: the minimum frequency corresponds to the inverse of the sampling duration, and the maximum frequency equals the sampling rate for complex-valued signals and half the sampling rate for real-valued signals.

In this chapter, it is shown using 3D periodically sampled turbulent pipe flow DNS data that, if the flow fields are Fourier transformed in the homogeneous spatial (wall-parallel) directions, the frequency content of each Fourier mode is approximately sparse, implying that compressive sampling can be applied to identify the dominant frequencies. The use of compressive sampling in wall-bounded turbulence is demonstrated by a series of tests, based on synthetic velocity fields with known frequency content, aimed at verifying the output from the compressive sampling routine. A new randomly sampled turbulent pipe flow DNS is analyzed via compressive sampling and shown to have a compact representation in the form of a superposition of energetic propagating waves. The frequency content of energetic spatial Fourier modes is shown to be sparse, and can be resolved using significantly less samples compared to periodic sampling. Results also show that compressive sampling resolves frequencies up to several times higher than the mean sampling rate.

## 3.2 Methodology

Two different types of data sets were used to investigate the application of compressive sampling to wall-bounded turbulence and were based, respectively, on synthetic velocity fields with known frequency content and turbulent pipe flow DNS data. The cylindrical coordinate system used to project the flow fields is shown on figure 4.2. The synthetic velocity fields were used to check that compressive sampling extracts the right frequencies and to determine the optimal sampling

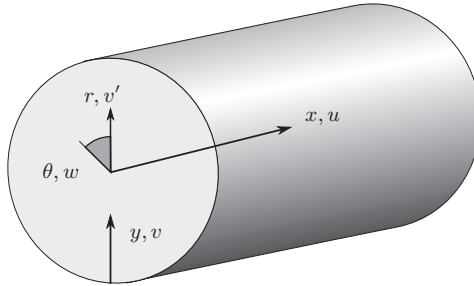


Figure 3.1: Schematic of pipe geometry and nomenclature (McKeon & Sharma, 2010).

parameters for a new DNS run with velocity fields recorded at random instants in time. Frequency analysis of the periodically and randomly sampled DNS data was performed to ensure that the frequency content is approximately sparse and validate the use of compressive sampling in wall-bounded turbulence, respectively. In the following section, the data sets used in this study are presented, and the methods to analyze the frequency content of the different flow fields are described.

### 3.2.1 Synthetic Velocity Fields

Synthetic velocity fields that approximate the DNS propagating waves but have a known frequency content were generated using the framework of McKeon & Sharma (2010). Generation of these fields required low computational and storage resources compared to the DNS flow fields, thus they were used to identify the influence of the sampling parameters on the frequencies extracted via compressive sampling, for a known set of input frequencies.

McKeon & Sharma (2010) considered a gain analysis of the Navier-Stokes (NS) equations to obtain a basis for the wall-normal coherence of propagating waves in turbulent pipe flow. In this approach, the full synthetic velocity field  $\hat{\mathbf{u}}(x, r, \theta, t)$  was decomposed into a series of propagating waves defined by their streamwise and azimuthal wavenumbers  $(k, n)$  and angular frequency  $\omega = 2\pi f$ ,

$$\hat{\mathbf{u}}(x, r, \theta, t) = \sum_{k, n, \omega} a_{k, n, \omega} \mathbf{c}_{k, n, \omega}(r) e^{i(kx + n\theta - \omega t)}, \quad (3.2)$$

where the  $a_{k, n, \omega}$  are complex-valued coefficients denoting the relative magnitude and phase of the waves. The wavenumbers and frequencies are non-dimensionalized based on the pipe radius and bulk velocity. Berkooz *et al.* (1993) showed that the Fourier series decomposition in the homogeneous (spatial and temporal) directions (equation (3.2)) is optimal in the sense that it maximizes the turbulent kinetic energy captured for a given number of basis functions and the Fourier modes are known to be the eigenmodes of the linear NS equations. Under this formulation, the nonlinear terms in the NS equations for the velocity fluctuations act as an unknown forcing on the linear part of

the equations. A divergence-free basis was used in the radial direction to project the NS equations, resulting in the elimination of the pressure term. The radial distribution of momentum  $\mathbf{c}_{k,n,\omega}(r)$  for the propagating waves is described by the forced NS equations

$$i\omega\mathbf{c}_{k,n,\omega}(r) = \mathcal{L}_{k,n,\omega}(r)\mathbf{c}_{k,n,\omega}(r) + \mathbf{f}_{k,n,\omega}(r), \quad (3.3)$$

where  $\mathbf{f}_{k,n,\omega}(r)$  and  $\mathcal{L}_{k,n,\omega}(r)$  are the projection of the nonlinear terms and of the linear part of the NS equations onto the Fourier basis, respectively. The propagating wave  $\mathbf{c}_{k,n,\omega}(r)e^{i(kx+n\theta-\omega t)}$  can be seen as a response of the mean turbulent flow to the forcing  $\mathbf{f}_{k,n,\omega}(r)$  via the transfer function  $(i\omega I - \mathcal{L}_{k,n,\omega}(r))^{-1}$ , i.e.,

$$\mathbf{c}_{k,n,\omega}(r) = (i\omega I - \mathcal{L}_{k,n,\omega}(r))^{-1}\mathbf{f}_{k,n,\omega}(r). \quad (3.4)$$

The analysis identifies the forcing and response modes that are most amplified based on a turbulent kinetic energy norm, at each given wavenumber pair and frequency, via singular value decomposition (SVD) of the transfer function.

The framework of McKeon & Sharma (2010) was used to generate response modes to represent wall-bounded turbulence. The synthetic velocity fields were constructed by superposition of response modes computed with three different  $(k, n)$  wavenumber pairs chosen to represent the large scales (1, 10) modes, the near-wall type modes (4.3, 43) corresponding to a streamwise and azimuthal extent of 1,000 and 100 viscous wall-units at  $Re = 24,580$ , and the small dissipative scales (16.75, 60), respectively. For each wavenumber pair, several convection velocities (frequencies) were chosen arbitrarily in a range varying from a few viscous units to the centerline velocity. The propagating waves generated with the three wavenumber pairs and the various frequencies span the broad range of scales present in wall-bounded turbulence, and their superposition results in realistic velocity fields due to the coherence in the wall-normal direction. The relative phase of the waves was randomly chosen and the magnitude was set to one. The propagating waves were computed using the spectral code of Meseguer & Trefethen (2003) modified by McKeon & Sharma (2010) to allow for the input of any velocity profile and the decomposition into singular modes. The velocity profile from the DNS of Wu & Moin (2008) at  $Re = 24,580$  was used as an input to the model. The synthetic fields can be sampled at any time instant and require low computational and storage resources compared to the DNS flow fields, allowing for the test of numerous sampling parameters to use compressive sampling in wall-bounded turbulence.

Compressive sampling was applied to the streamwise velocity component of the synthetic velocity fields sampled randomly in time. The velocity fields were decomposed as a Fourier series in the streamwise and azimuthal directions, and each 2D Fourier mode  $c_{k,n}(r, t_s)$  was written as a Fourier

series in time with unknown coefficients,

$$c_{k,n}(r, t_s) = \sum_{j=1}^{N_{opti}} c_{k,n,2\pi jdf}(r) e^{i2\pi jdf t_s}, \quad (3.5)$$

where  $N_{opti}$  and  $df$  are optimization variables (to be determined) corresponding respectively to the number of frequencies and the frequency increment for the optimization. The coefficients of the temporal Fourier series  $c_{k,n,2\pi jdf}(r)$  are the solution of an optimization problem that consists of minimizing the sum of the absolute value of the Fourier coefficients  $c_{k,n,2\pi jdf}(r)$ , i.e., minimizing

$$\sum_{j=1}^{N_{opti}} |c_{k,n,2\pi jdf}(r)|, \quad (3.6)$$

at each wall-normal location separately, under the constraint that the reconstructed signal

$$\sum_{j=1}^{N_{opti}} c_{k,n,2\pi jdf}(r) e^{i2\pi jdf t_s}$$

matches the input signal  $c_{k,n}(r, t_s)$  at every sampling time instant  $t_s$ . The dominant Fourier coefficients  $c_{k,n,2\pi jdf}(r)$  identified via compressive sampling correspond to the streamwise component of the propagating waves  $\mathbf{c}_{k,n,\omega}(r)$  constituting the synthetic flow field.

Contrarily to periodic sampling, the frequency range for the optimization  $[df, N_{opti} \times df]$  is not directly related to the sampling parameters, and was chosen to maximize the frequency resolution, while still satisfying the sparsity relationship (equation (3.1)). For simplicity, the frequencies were chosen to be equi-spaced within the optimization frequency range (but this is not required in order to apply compressive sampling). The maximum and minimum frequencies can be respectively higher than the mean sampling rate and lower than the inverse of the sampling duration. The lower the number of sparse frequencies present in the input signal the broader the frequency range that can be resolved with compressive sampling.

The minimization problem was solved with Matlab using the CVX toolbox for convex optimization, and an example of the code used is shown in appendix A. The frequency spectrum was computed at each wall-normal location, and integrated in the radial direction to identify the energetically dominant frequencies, and to check whether the dominant frequencies matched the input frequencies. The optimization frequency range and sampling parameters were adjusted to find the optimal number of samples and sampling duration leading to the recovery of the signal.

### 3.2.2 DNS Velocity Fields

The DNS velocity fields were kindly provided by X. Wu who used the second-order finite difference code described in Wu & Moin (2008) at  $Re = 24,580$  ( $Re_\tau = 685$ ), and with a domain length of  $30R$  ( $k_{min} = 0.21$ ). The number of grid points in the streamwise, wall-normal, and azimuthal directions was respectively  $2048 \times 256 \times 1024$ . The DNS data was subsampled by a factor of 4 in the streamwise and azimuthal directions to decrease the size of the data files. The flow domain is large enough for the spatial-averaged velocity profile and streamwise turbulence intensity profile to be converged, even with the subsampling.

Two sets of velocity fields were available. For the first set, the flow was periodically sampled in time at a rate of 1 sample every 7.2 dimensionless time units, based on the pipe radius and bulk velocity. A total of 21 samples was taken over 150 dimensionless time units. The number of samples and sampling duration for the first data set could not be chosen by the authors and constrained the number of Fourier modes that could be resolved with the data. The second set was randomly sampled based on the parameters derived in the present study in order to apply compressive sampling.

The 21 periodically sampled DNS velocity fields were used to check whether the frequency content of the Fourier modes was indeed sparse. Each velocity field was Fourier transformed in the streamwise and azimuthal directions by applying a 2D FFT,

$$u(x, r, \theta, t) = \sum_{k,n} c_{k,n}(r, t) e^{i(kx+n\theta)}, \quad (3.7)$$

and normalized such that

$$\sum_{k=0}^{255k_{min}} \sum_{n=-128}^{127} c_{k,n}(r) c_{k,n}^*(r) = u'^2(r), \quad (3.8)$$

where  $*$  denotes the complex conjugate and  $k_{min} = 0.21$  for a domain length of  $30R$ . The 2D spatial Fourier modes are referred to by their wavenumber pair  $(k, n)$ . Only the positive  $k$  half plane was kept since the spectrum of a real-valued signal is symmetric. The 2D Fourier spectrum was integrated in the wall-normal direction and averaged in time to identify the 2D Fourier modes that contribute most to the streamwise turbulence intensity, effectively a crude POD over a limited resolvable parameter space.

The range of 2D Fourier modes that were free from aliasing effects was estimated based on their streamwise wavenumber by comparing the frequency range that can be resolved with the available DNS data to the empirical bounds on the frequency content of the flow. The dynamically significant frequency content in wall-bounded turbulence was estimated as a function of the streamwise wavenumber by assuming that the highest and lowest convection velocities correspond respectively to the centerline velocity and 10 times the friction velocity. The upper bound comes from the analysis of the Orr-Sommerfeld equation by Joseph (1968) showing that, for laminar channel flow, the

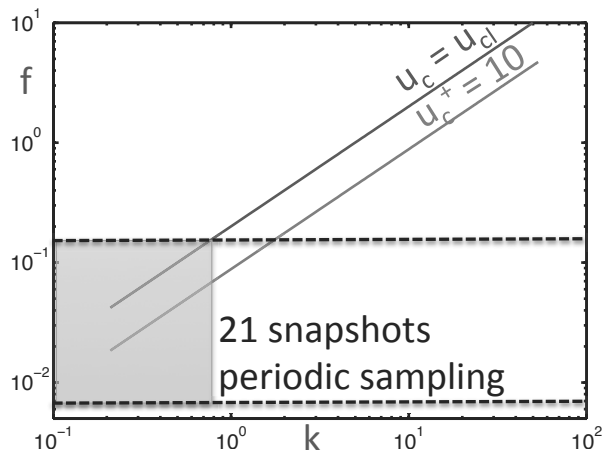


Figure 3.2: Frequency range resolved by the periodically sampled DNS data (delimited by the two horizontal dashed lines) compared to the empirical upper and lower bounds on the DNS frequency content (solid lines) as a function of the streamwise wavenumber  $k$ . The shaded area shows the time-resolved streamwise wavenumber range for the available data.

real part of the eigenvalues, which corresponds to the convection velocity of the disturbances, is restricted to the range set by the mean flow. The lower bound was estimated based on the results of Morrison *et al.* (1971), who used experimental data to decompose the buffer layer as a sum of propagating waves, and found that the lowest convection velocity is about 10 times the friction velocity,  $u = 10u_\tau$ , or  $0.44\bar{U}$  at  $Re = 24,580$ . The value for the lowest convection velocity is broadly supported in the literature, as summarized by LeHew *et al.* (2011).

The upper and lower bounds on the frequency content as a function of the streamwise wavenumber are depicted on figure 3.2. The highest frequency that could be resolved with the available DNS data is given by the inverse of the sampling rate  $f_{max} = \frac{1}{7.2} = 0.14$  and is reached at  $k = 0.69$  for modes convecting at the centerline velocity. All the modes with  $k \geq 0.69$  have part of their frequency content aliased to lower frequencies, such that only the frequency content of the lowest three streamwise wavenumbers  $k = 0.21, 0.42,$  and  $0.63$ , for various azimuthal wavenumbers, could accurately be extracted from the available DNS data by applying a FFT in time, because the Nyquist criterion is satisfied for these three modes.

Similarly to the periodically sampled DNS velocity fields, the randomly sampled fields were decomposed as a Fourier series in the streamwise and azimuthal directions using a 2D FFT, and the 2D Fourier spectrum was integrated in the wall-normal direction and averaged in time, to identify the most energetic spatial modes. Compressive sampling was used to extract the frequency content of these most energetic modes at each wall-normal location, following the same methodology as for the synthetic velocity fields. The frequency spectrum was integrated in the wall-normal direction to identify the sparse frequencies, defined as the frequencies containing not less than 10% of the energy

in the peak frequency.

As an alternative approach, compressive sampling was also applied globally on the  $\ell_2$ -norm of the temporal Fourier coefficients in the wall-normal direction, i.e., to minimize

$$\sum_{j=1}^{N_{opti}} \int_0^1 c_{k,n,2\pi jdf}(r) c_{k,n,2\pi jdf}^*(r) r dr, \quad (3.9)$$

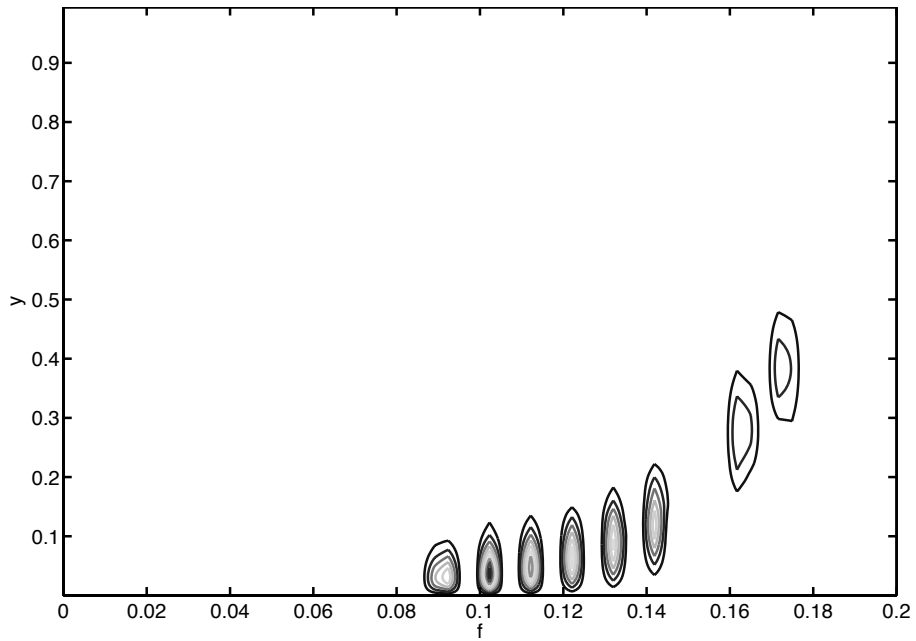
where  $*$  denotes the complex conjugate. The 2D Fourier modes were interpolated on a uniform grid in the radial direction and premultiplied by  $\sqrt{r}$ , such that the  $\ell_2$ -norm corresponds to the energy norm in cylindrical coordinates. The latter method only needs to be applied once, instead of at each wall-normal location separately, and tends to select frequencies that are energetic over a wide range of wall-normal locations. However, the optimization algorithm converges significantly slower due to the significant increase in the number of constraints from  $N_s$  (the number of samples) to  $N_s \times N_r$  (the number of samples times the number of grid points in the radial direction). The results obtained with the two methods were compared to identify the best method to use in wall-bounded turbulence.

### 3.3 Results

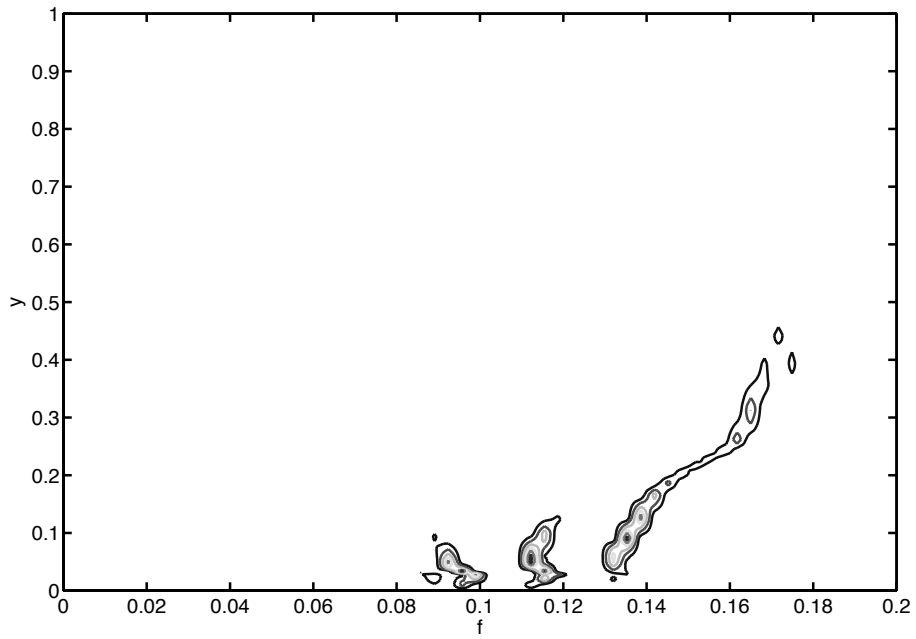
#### 3.3.1 Demonstration of Compressive Sampling Using Synthetic Velocity Fields

The use of compressive sampling in wall-bounded turbulence was demonstrated by a series of tests, based on synthetic velocity fields with known frequency content, aimed at verifying the output from the compressive sampling routine. The frequency content of the synthetic velocity fields was analyzed to identify the combination of sampling and optimization parameters leading to the correct estimation of the input frequencies. A representative frequency spectrum is shown on figure 3.3(a). It was found that taking 30 samples randomly distributed over 100 dimensionless time units was enough to resolve the frequency content of the synthetic velocity fields. The frequencies inferred via compressive sampling are reported on table 3.1, and compared to the input frequencies. The relative error between the input and predicted frequencies is about 1% or less. The frequency increment  $df$  and the number of frequencies for the optimization  $N_{opti}$  result from a balance between satisfying the sparsity relationship (equation (3.1)) and increasing the frequency resolution. Their value can be chosen separately for each 2D Fourier mode and is reported on table 3.1.

As a result of the synthetic field tests, the frequency range resolved by compressive sampling was shown to be significantly broader than the range that could be resolved using periodic sampling, with the same number of samples and sampling duration. The highest frequency was about 6 times higher than the mean sampling frequency ( $f_s = 0.3$ ). The limit on the number of sparse frequencies



(a)



(b)

Figure 3.3: Frequency spectrum pre-multiplied by  $r$  as a function of the wall-normal distance  $y$ , for the large-scale mode  $(k, n) = (1, 10)$ , with the 8 input frequencies reported on table 3.1, sampled during 100 (a) and 25 (b) dimensionless time units. The distorted contours (b) indicate that the sparsity relationship is not satisfied.

<b>Large-scale mode (1,10), <math>N_{opti} = 600</math>, <math>df = 0.0033</math></b>								
Input frequencies	0.091	0.102	0.113	0.122	0.132	0.142	0.163	0.173
Output frequencies	0.090	0.103	0.113	0.123	0.133	0.143	0.163	0.173
Relative error	1.1%	1.0%	0	0.8%	0.8%	0.7%	0	0

<b>Wall-type mode (4.3,43), <math>N_{opti} = 900</math>, <math>df = 0.0033</math></b>								
Input frequencies	0.309	0.325	0.342	0.488	0.520	0.651	0.813	0.895
Output frequencies	0.310	0.327	0.340	0.487	0.520	0.650	0.814	0.892
Relative error	0.3%	0.6%	0.6%	0.2%	0	0.2%	0.1%	0.3%

<b>High <math>k</math> mode (16.75,60), <math>N_{opti} = 900</math>, <math>df = 0.0056</math></b>					
Input frequencies	0.618	0.651	0.683	1.627	1.789
Output frequencies	0.615	0.650	0.683	1.628	1.788
Relative error	0.5%	0.2%	0	0.1%	0.1%

Table 3.1: Parameters and optimization results for the three test cases. The input frequencies come from the content of the synthetic velocity fields, the output frequencies are those recovered by optimized compressive sampling.

that could be resolved for a given number of samples and sampling duration was evaluated by adding more and more sparse frequencies to the synthetic velocity fields. Based on the sparsity relationship (equation (3.1)) the highest frequency that could be resolved is  $f_{max} = 0.64$  for the large-scale and wall-type modes and  $f_{max} = 1.66$  for the high  $k$  mode. The difference comes from the lower number of sparse frequencies in the high  $k$  mode. The estimated maximum frequencies are close to the ones used in the test cases, supporting that the test cases represent the best that can be done with the given sampling parameters, and especially that no more than 5 frequencies can be resolved for the high  $k$  mode. Compressive sampling seemed to perform slightly better in the present study than predicted by the sparsity relationship (equation (3.1)), possibly because the amplitude of the coefficients was not required to match the input signal up to machine precision as was the case in the analysis by Tropp *et al.* (2010), but rather to contain at least 10% of the peak frequency energy.

Figure 3.3 illustrates how the method degrades when the sparsity relationship is no longer satisfied. The frequency spectrum for the large-scale mode is plotted on figure 3.3(a) and exhibits vertical contours corresponding to frequency peaks that are distinct and relatively far apart. When the number of sparse frequencies is increased, or the sampling duration (which is related to the resolvable bandwidth  $\Omega$  of the signal in equation (3.1)) decreased, such that the sparsity relationship is violated, the convex optimization does not recover all the input frequencies, and instead generates spurious frequencies. As a result, the contours of the frequency spectrum on figure 3.3(b) obtained by sampling during 25 dimensionless time units (instead of 100) are slanted and contain several incorrect frequency peaks. The longest timescale of the input signal is 8.85 dimensionless time units, i.e., about third of the sampling duration.

Based on the frequency analysis of the synthetic velocity fields for various sets of sampling and

optimization parameters, it was predicted that 50 samples randomly distributed over 100 dimensionless time units are sufficient to resolve via compressive sampling all the dynamically significant time scales in turbulent pipe flow at  $Re = 24,580$ . (To be conservative, the number of samples was increased from the value of 30 used in the test cases to 50.)

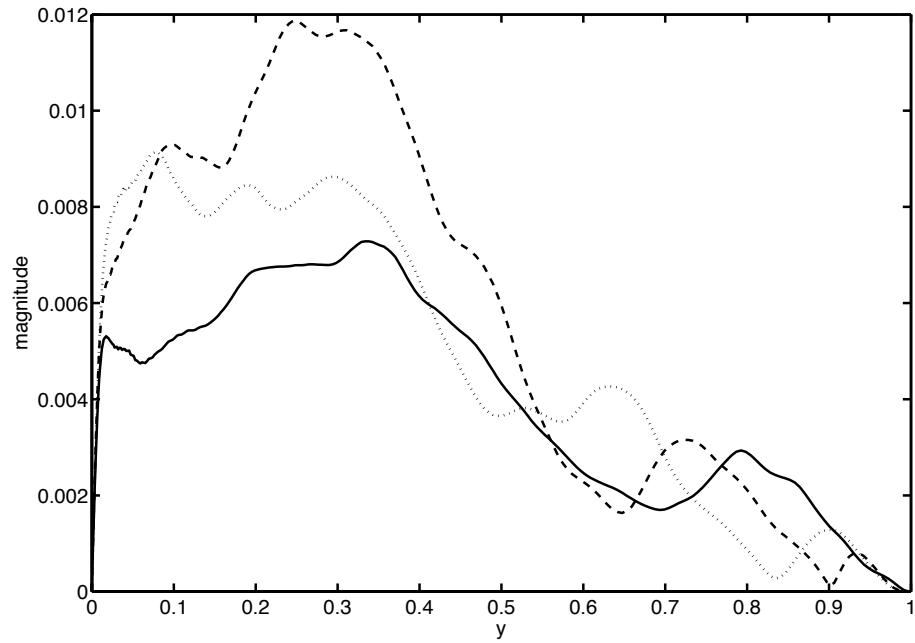
### 3.3.2 Sparsity Check Based on Periodically Sampled DNS Data

Since the compressive sampling technique requires approximate sparsity, in this case in the frequency domain, an explicit check for this condition in wall-bounded turbulence was performed using periodically-sampled DNS data. The frequency spectrum of the most energetic 2D Fourier modes was computed as a function of the wall-normal distance by performing a FFT of the 21 samples available, in time, at each wall-normal location. Only the modes with  $k \leq 0.63$  which are free from aliasing effects were considered.

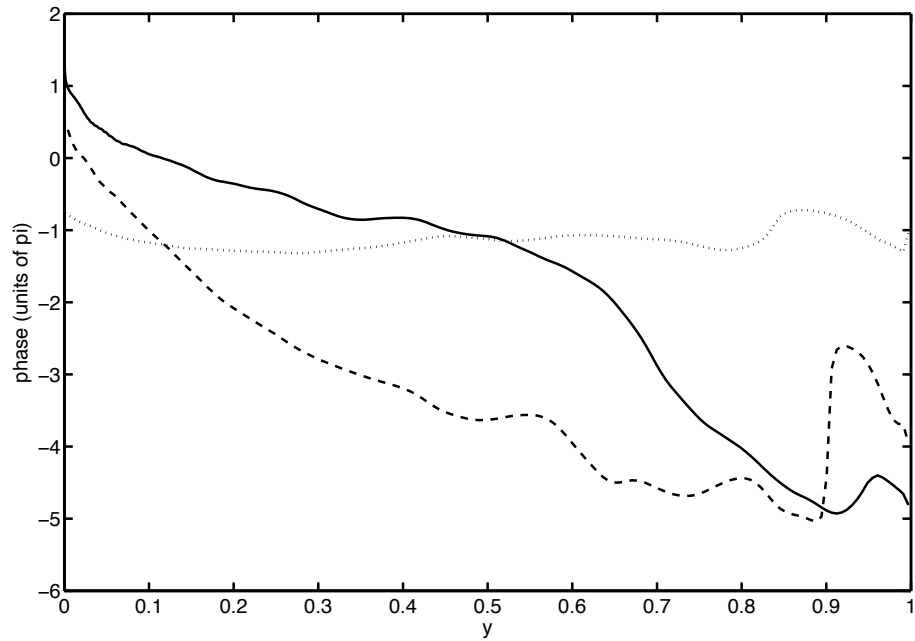
The time average wall-normal profiles of the three most energetic 2D Fourier modes are plotted on figure 3.4. The modes are tall in the wall-normal direction and extend to the centerline. A representative frequency spectrum corresponding to the mode  $(0.42, 5)$  is plotted on figure 3.5 as a function of the wall-normal distance, together with the empirical bounds on the frequency content, corresponding to convection velocities equal to the centerline velocity and 10 times the friction velocity, or equivalently  $0.44U_{CL}$  at  $Re = 24,580$ . The frequency spectrum exhibits vertical contours highlighting that the most energetic 2D Fourier modes correspond to a superposition of propagating waves with constant phase speed, which are coherent in the wall-normal direction. The frequency content of all the modes studied is always sparse, exhibiting between one and three dominant frequencies, all the other frequencies contain at least an order of magnitude less energy than the dominant frequency. The dominant frequencies fall in between the two empirical bounds on the frequency content. Hence, even though turbulent pipe flow exhibits a continuous frequency spectrum when measured locally in space, as a result of the sparsity of the 2D Fourier modes in the frequency domain, compressive sampling can be used in wall-bounded turbulence if the flow fields are Fourier transformed in the homogeneous directions first.

### 3.3.3 Frequency Analysis of Randomly Sampled DNS Data via Compressive Sampling

A new run of the turbulent pipe flow DNS was performed by Xiaohua Wu, and the velocity fields were recorded at the 50 sampling time instants shown on figure 4.1 and randomly distributed over 100 dimensionless time units. The time instants were computed using the optimal sampling parameters derived using the synthetic velocity fields. Convex optimization problems were solved using



(a)



(b)

Figure 3.4: Wall-normal profile of the magnitude (a) and phase (b) for the first three most energetic modes  $(k, n) = (0.21, -2)$  (dotted),  $(k, n) = (0.42, 3)$  (dashed), and  $(k, n) = (0.21, 2)$  (solid) of the periodically sampled DNS flow field.

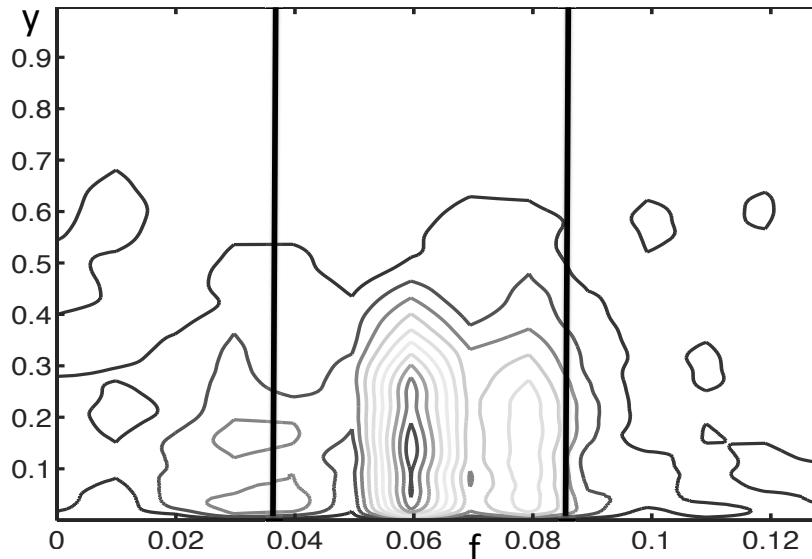


Figure 3.5: Representative frequency spectrum corresponding to the 2D Fourier mode  $(k, n) = (0.42, 5)$  as a function of the wall-normal distance, with the empirical upper and lower bounds on frequency, corresponding to convection velocities equal to the centerline velocity and 10 times the friction velocity, demarcated by the two vertical lines.

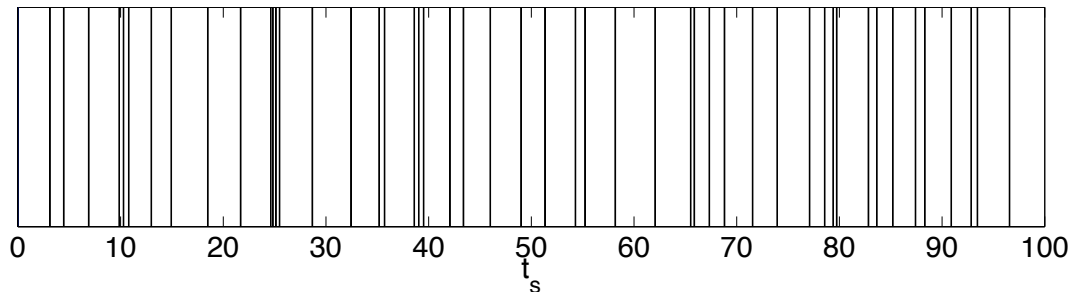


Figure 3.6: The 50 DNS sampling time instants randomly distributed over 100 dimensionless time units based on the radius and bulk velocity. The last sampling time instant is at  $\tau = 96.57$ .

CVX, for each energetic 2D Fourier mode extracted from the 50 velocity fields, to obtain their frequency content. The optimization parameters resulting in the highest frequency resolution that still satisfies the sparsity relationship were determined by analysis of the frequency content of several 2D Fourier modes. The capabilities of compressive sampling were further tested by investigating how the method degrades when the sparsity relationship is violated. The optimization can be performed at each wall-normal location separately, or globally by minimizing the  $\ell_2$ -norm of the temporal Fourier coefficients in the wall-normal direction. The two methods were compared and the best one was chosen to analyze the frequency content of a broad range of 2D Fourier modes.

It was found by analyzing the frequency content of the DNS 2D Fourier modes that an optimization frequency range from  $-1$  to  $1$  allows for both upstream and downstream propagating waves, and with a frequency increment of  $0.005$ , results in the highest frequency resolution that can

be obtained with the given number of samples. Only the downstream propagating waves carry a significant fraction of the streamwise turbulence intensity, but the noise is spread over both upstream and downstream propagating waves, leading to a sparser solution. The fundamental frequency is  $f_{min} = 0.005$  or half the inverse of the sampling duration and the number of optimization frequencies is 400. Using periodic sampling, the flow would have to be sampled for 200 dimensionless time units in order to obtain a fundamental frequency of 0.005 and 400 samples would be required instead of 50 in the case of compressive sampling.

The solution to the convex optimization problem was shown to be robust with respect to variations of the fundamental and maximum frequencies, as long as the sparsity relationship is satisfied, and the maximum frequency is high enough to resolve the noise. When the resolution is increased by lowering the fundamental frequency, the width of the peak in the power spectral density stays constant, but the number of frequencies within the peak increases, resulting in a violation of the sparsity relationship (equation (3.1)). Figure 3.7 shows that, when the resolution is doubled, the number of sparse frequencies within the peak increases from 2 to 4, and the frequency spectrum as a function of the wall-normal distance exhibits distorted contours, indicative of a violation of the sparsity relationship. The minimum number of samples required to resolve correctly the spectrum on figure 3.7(b) is 32, whereas for the spectrum on figure 3.7(d) 57 samples are needed, but only 50 are available.

When the sparsity relationship is violated, the results degrade differently depending on whether a global or local minimization is used. In the case of global minimization, the energy is spread over more frequencies, and the contribution of each dominant frequency to the streamwise turbulence intensity decreases. The wall-normal profiles of the temporal Fourier modes are still smooth and span the whole radius. In the case of local minimization, the dominant frequencies can vary slightly from one wall-normal location to the next, leading to distorted profiles that span only a portion of the radius, as can be seen on figures 3.8(c),(d) and 3.7(a),(c). The 2D Fourier modes reconstructed based on the sparse frequencies extracted via compressive sampling do not change when the sparsity relationship is no longer satisfied, implying that the same amount of energy is captured by the sparse frequencies, but distributed differently among them. The sparse frequencies do not change when the maximum optimization frequency is doubled, keeping the fundamental frequency constant, illustrating the robustness of the method once the sparsity relationship is satisfied.

Based on the study of several 2D Fourier modes, the sparse frequencies obtained using either the local or global minimizations were shown to be identical, as were the reconstructed 2D Fourier modes based on the sparse frequencies. However, the wall-normal profiles of the temporal Fourier modes were smoother in the case of global minimization (see figure 3.8), justifying the choice of the global minimization method to analyze the 2D Fourier modes. The frequency content of a broad range of energetic 2D Fourier modes was analyzed via compressive sampling using the global opti-

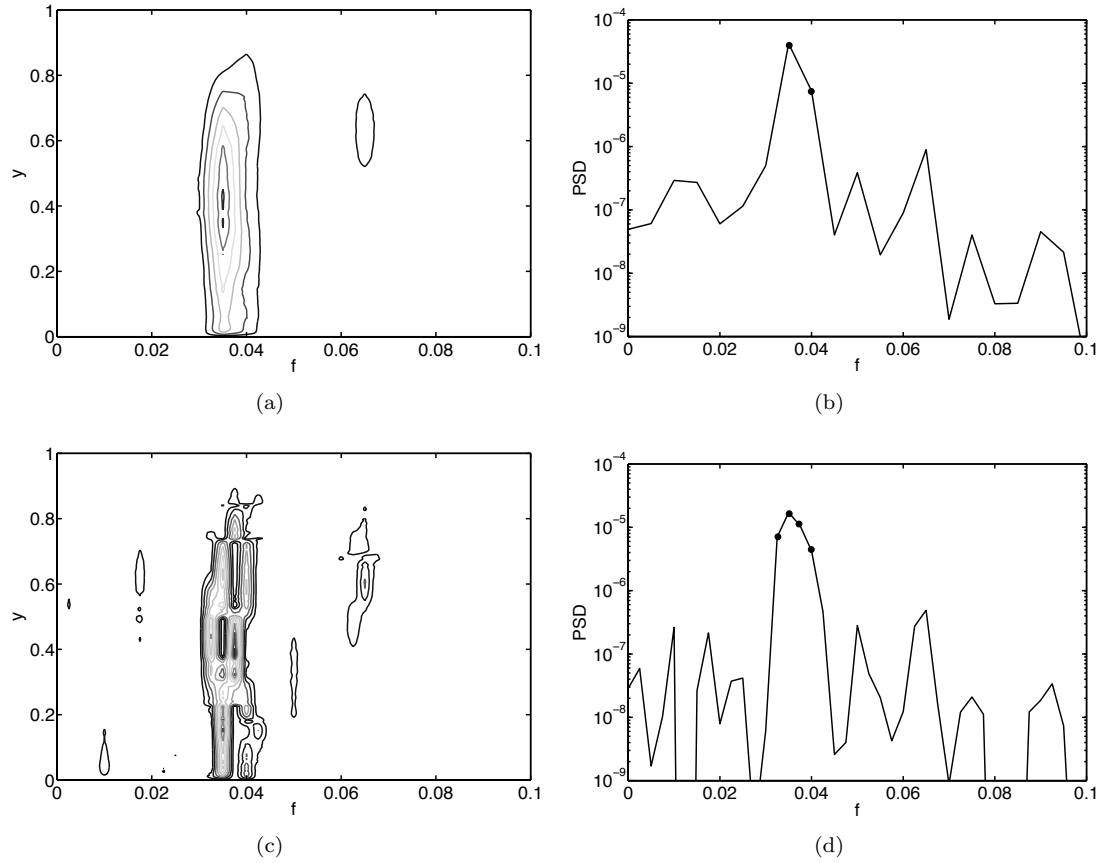


Figure 3.7: Power spectral density over the frequency range  $f \in [0, 0.1]$  as a function of the wall-normal distance (a),(c) and integrated in the wall-normal direction (b),(d) for the 2D Fourier mode  $(k, n) = (0.21, 2)$  from the randomly sampled DNS. The top and bottom rows correspond to a local minimization with respectively 400 and 800 optimization frequencies. The dots (b),(d) indicate the sparse frequencies.

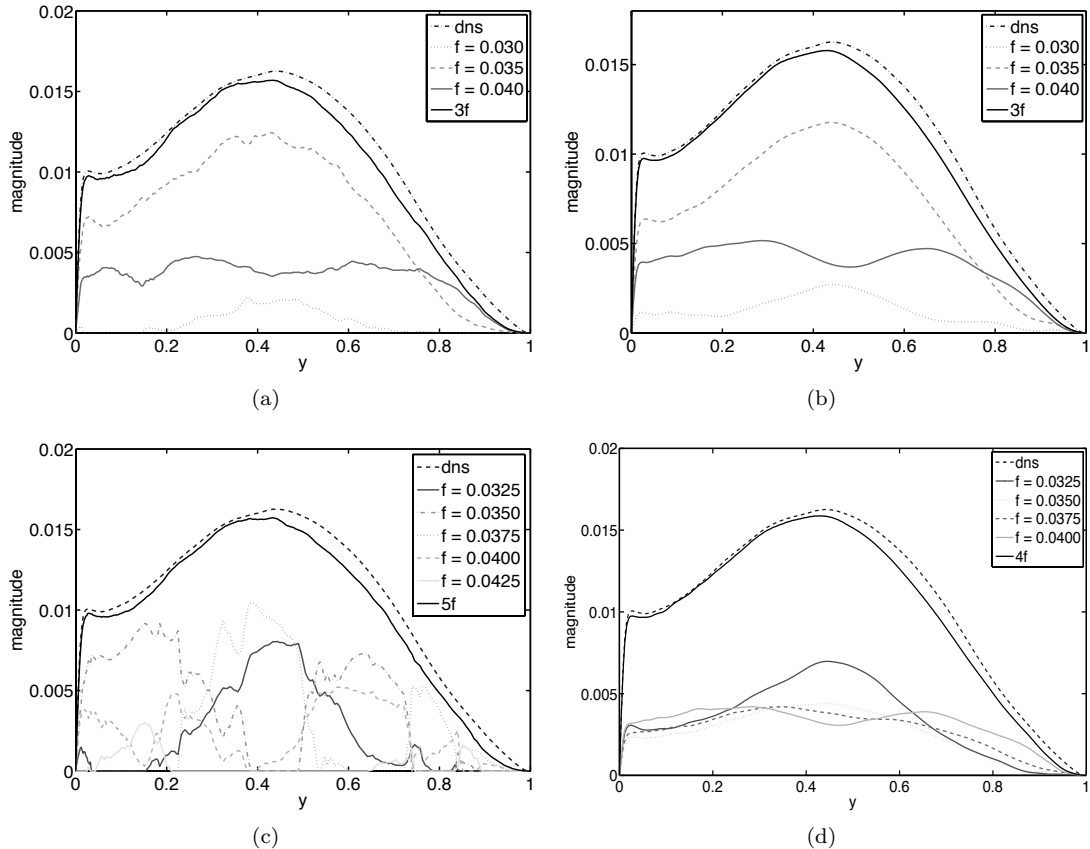


Figure 3.8: Wall-normal profiles of the Fourier modes  $(k, n, \omega) = (0.21, 2, 2\pi f)$  from the randomly sampled DNS, for the different dominant frequencies, compared to the time average of the original and reconstructed signals computed using the local (a) and global (b) minimizations with 400 optimization frequencies, and the local (c) and global (d) minimizations with 800 optimization frequencies. The maximum frequency for the optimization is 1 in both cases.

mization method and the optimization parameters  $df = 0.005$  and  $f \in [-1, 1]$ .

The most energetic 2D Fourier mode  $(0.21, 2)$  was considered as a representative example of the low streamwise wavenumber modes. Figure 3.7(b) shows that the frequency spectrum in the range  $[0, 0.1]$  contains two sparse frequencies  $f = 0.035$  and  $0.040$ , with an energy content of not less than 10% of the peak value. The power spectral density over the full frequency range used for the optimization is shown on figure 3.9. Most of the energy is concentrated in the range  $[0, 0.1]$  and the higher frequencies, as well as the negative frequencies corresponding to upstream propagating modes, only capture the noise. The noise floor is about 5 orders of magnitude lower than the peak. The presence of negative optimization frequencies is required for the optimization to converge, unless the highest optimization frequency is increased. It is found that sparser solutions are obtained using both positive and negative optimization frequencies, instead of increasing the upper bound on the optimization frequencies. The optimization will not converge if the frequency range is restricted to  $[0, 0.1]$  because the high frequency noise above the noise floor cannot be resolved. The temporal

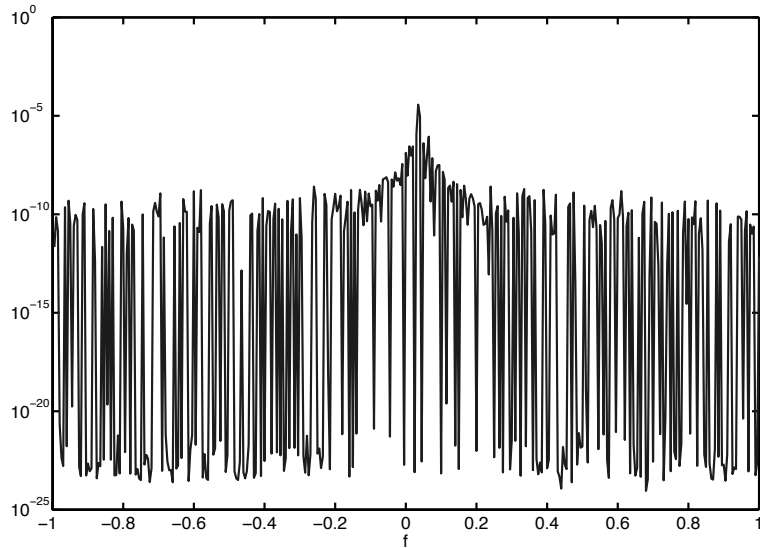


Figure 3.9: Power spectral density for the 2D Fourier mode  $(k, n) = (0.21, 2)$  from the randomly sampled DNS obtained via optimal compressive sampling.

Fourier modes corresponding to the three dominant frequencies  $f = 0.030, 0.035,$  and  $0.040$  of the 2D Fourier mode  $(0.21, 2)$  are plotted on figure 3.8(b), and together contain 91% of the streamwise turbulence intensity compared to 52% for the peak frequency alone. The frequency  $f = 0.030$  is not considered to be a sparse frequency, based on the criterion that sparse frequencies need to contain at least 10% of the peak energy, but is retained as a dominant frequency such that the superposition of the three dominant frequencies captures over 90% of the energy in the 2D Fourier mode  $(0.21, 2)$ .

The 2D Fourier modes can be reassembled by summation over the temporal Fourier modes corresponding to the sparse frequencies. The presence of dominant frequencies adjacent to the peak frequency provides for the amplitude modulation of the 2D Fourier modes. Figure 4.8(a),(b) shows that the 2D Fourier mode  $(0.21, 2)$  can be reconstructed with only three temporal Fourier modes (sparse frequencies) and the relative phase of the modes captures the increase in magnitude of the 2D Fourier mode observed particularly from the first to the second period.

Another two 2D Fourier modes  $(1.05, 2)$  and  $(3.14, 4)$  were selected for illustration purposes and represent the range of streamwise wavenumbers that can be analyzed with the 50 velocity fields available. The contours of the real part of the two 2D Fourier modes in a wall-normal-temporal plane are plotted on figure 3.11(a),(c) and the wall-normal profile of their dominant temporal Fourier modes is shown on figure 3.11(b),(d). A comparison between figures 4.8 and 3.11 shows that the extent of the uniform momentum zones in the wall-normal direction decreases as the streamwise wavenumber increases, and the reconstructed modes contain less and less energy near the wall, due to the appearance of two different types of uniform momentum zones in the wall-normal direction, identified visually on figure 3.11(c) above and below  $y = 0.1R$ . Close to the wall, the uniform momentum

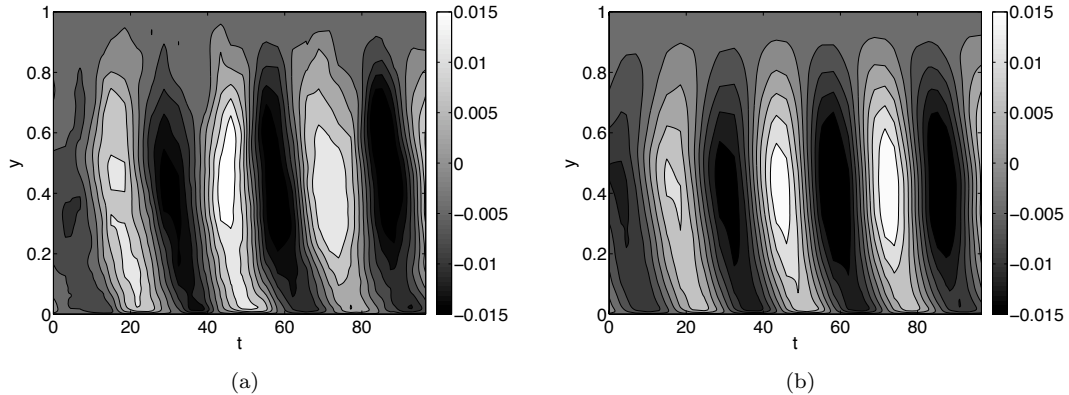


Figure 3.10: Contours of the real part of the 2D Fourier mode  $(k, n) = (0.21, 2)$  from the randomly sampled DNS, as a function of the wall-normal distance and time, with all the frequencies included (a) and with only three dominant frequencies recovered from compressive sampling included (b).

zones are short in the wall-normal direction whereas further from the wall, the uniform momentum zones have a radial wavelength of about a quarter radius inferred from the sharp peak in the radial power spectrum in figure 3.12(a). The spectrum is obtained by applying a FFT to the data without windowing since the profiles vanish at the boundaries (the wall and the centerline), and can therefore be assumed periodic with a fundamental wavelength equal to  $R$ . Using a sharp Fourier filter with a cutoff at the fourteenth mode, the near-wall type uniform momentum zones were separated from the core uniform momentum zones in the wall-normal direction. Figure 3.12(b),(c) shows the contours of the real part of the 2D Fourier mode  $(3.14, 4)$  Fourier filtered in the radial direction. The sharp Fourier filter successfully separated between the two different types of uniform momentum zones, as can be seen by comparing figure 3.12(b),(c) to figure 3.12(a). A minimization problem was solved separately for the two types of uniform momentum zones to extract their respective frequency content. The frequency content of the near-wall uniform momentum zones was shown to be broadband and could not be captured using compressive sampling with the chosen sampling parameters, justifying the decrease in the energy captured near the wall as  $k$  increases observed on figure 3.11(b),(d).

Compressive sampling was applied to a broad range of 2D Fourier modes, and successfully captured the frequency content in the core of the pipe for most of the energetic 2D Fourier modes ranging in size from the largest modes ( $k = 0.21$ ) all the way down to the near-wall type modes of size  $\lambda^+ = 1,000$  ( $k = 4.3$ ), supporting that the frequency content is indeed sparse. The frequency content of all the dominant modes studied is represented on figure 3.13(a) as a function of the streamwise wavenumber. Within a resolution error of  $df = \pm 0.0025$ , all the frequencies fall in between the lower and upper empirical bounds corresponding to convection velocities equal to respectively 10 times the friction velocity and the centerline velocity.

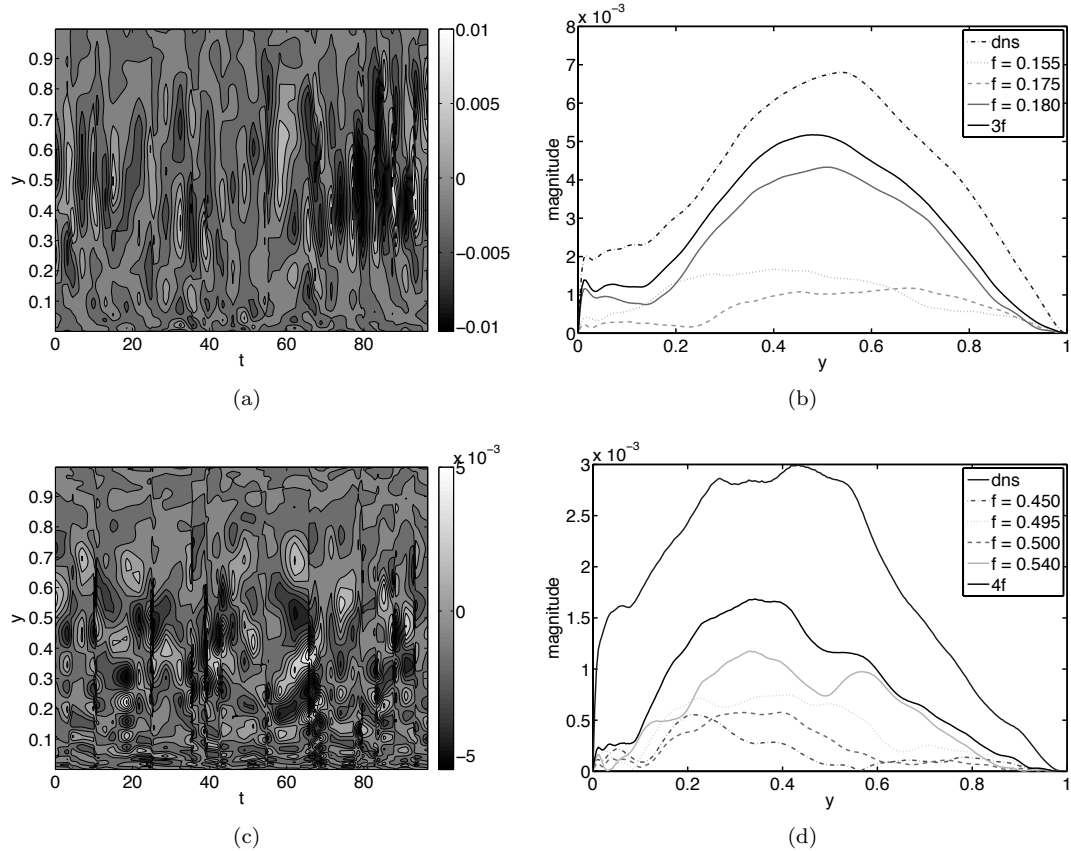
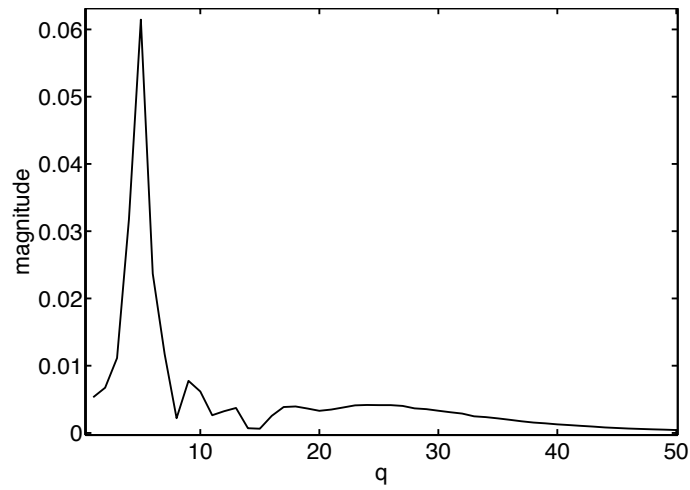
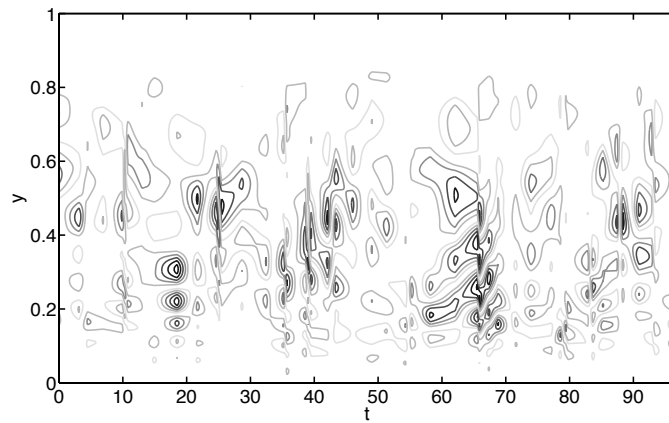


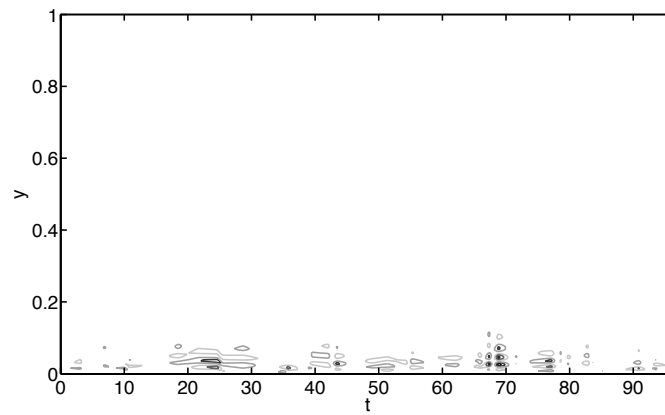
Figure 3.11: Contours of the real part of the 2D Fourier modes  $(k, n) = (1.05, 2)$  (a) and  $(k, n) = (3.14, 4)$  (c) from the randomly sampled DNS as a function of the wall-normal distance and time. Wall-normal profiles of the Fourier modes  $(k, n, \omega) = (1.05, 2, 2\pi f)$  (b) and  $(k, n, \omega) = (3.14, 4, 2\pi f)$  (d) for the different sparse frequencies compared to the time average of the original and reconstructed signals.



(a)



(b)



(c)

Figure 3.12: (a) Time-averaged power spectral density in the wall-normal direction for the 2D Fourier mode  $(k, n) = (3.14, 4)$  from the randomly sampled DNS. (b) Contours of the real part of the 2D Fourier mode  $(k, n) = (3.14, 4)$  low-pass filtered and (c) high-pass filtered showing the two different types of uniform momentum zones present in the wall-normal direction.

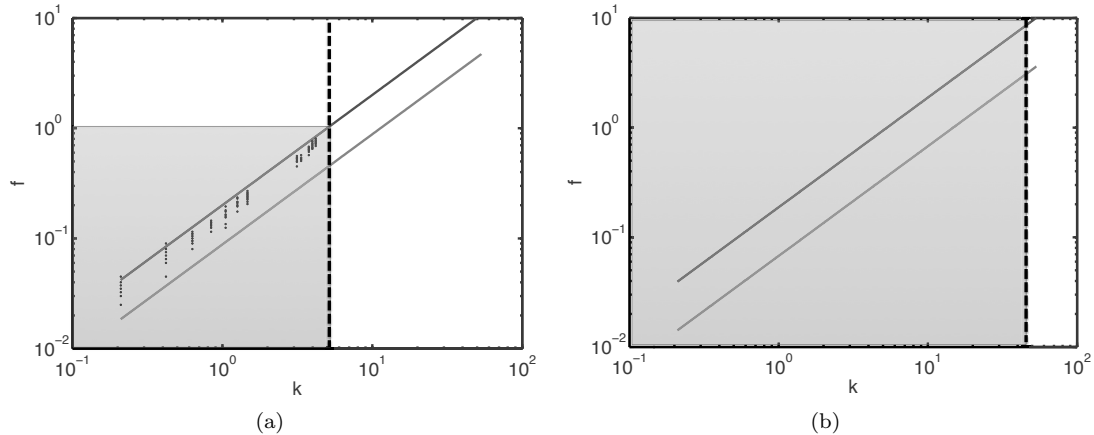


Figure 3.13: Frequency content of the 2D Fourier modes as a function of the streamwise wavenumber for various azimuthal wavenumbers (a). The two solid lines indicate the upper and lower empirical bounds on the frequency content and the dashed line shows the streamwise wavenumber corresponding to the near-wall type modes. The shaded areas highlight the dynamically significant bandwidth and streamwise wavenumber range at  $Re = 24, 580$  (a) and extrapolated to  $Re = 300,000$  (b).

### 3.3.4 Comparison with Periodic Sampling

Compressive sampling was compared with periodic sampling to emphasize the superiority of the former method in resolving the frequency content of the most energetic 2D Fourier modes, when only a limited amount of data is available. The data set corresponding to the periodically sampled DNS run contained 21 velocity fields distributed over 150 dimensionless time units, whereas for the randomly sampled DNS run, 50 fields were available and distributed over 100 dimensionless time units. The first 14 velocity fields of the periodically sampled DNS run were used to estimate the frequency content of the most energetic 2D Fourier modes via a FFT of the data in time. The minimum and maximum frequencies for the FFT are given by  $f_{min} = 0.01$  and  $f_{max} = 0.13$ . Only the 2D Fourier modes corresponding to the lowest three streamwise wavenumbers could be resolved, the other modes have their frequencies aliased to the range  $[0.01, 0.13]$ .

Compressive sampling was applied on 14 velocity fields randomly chosen among the 50 fields available to match the sampling duration and number of samples of the periodic data. The frequency content of the most energetic 2D Fourier modes could be resolved for  $k \leq 1.47$  instead of  $k \leq 4.3$  when the 50 samples were used. The dominant frequencies and their energy content are reported on table 3.2 for 5 representative 2D Fourier modes. The frequencies obtained match relatively well the results from the FFT, especially for the first two modes studied, even though two different runs of the DNS were used to generate the samples. The sparse frequencies obtained by compressive sampling with either 14 or 50 samples are identical, but the wall-normal profiles of the temporal Fourier modes vary slightly, see figure 3.14. The energy content of the sparse frequencies is higher when 14 samples are used instead of 50, and is also higher than for the frequencies obtained

(k,n)	f (CS)	% $u'^2$ (CS)	f (FFT)	% $u'^2$ (FFT)
(0.21,2)	0.035	82	0.03	51
	0.040	14	0.04	20
(0.42,-3)	0.065	95	0.06	21
			0.07	58
(0.63,-2)	0.09	23	0.08	50
	0.105	29	0.110	27
	0.110	23	–	–
(1.05,2)	0.180	59	–	–
(1.47,2)	0.255	15	–	–
	0.260	25	–	–
	0.265	8	–	–

Table 3.2: Frequency analysis of 5 representative modes using only 14 snapshots acquired over 100 dimensionless time units from two different runs of the turbulent pipe flow DNS. The dominant frequencies obtained via compressive sampling analysis of the randomly sampled DNS and their streamwise energy content are reported in the second and third columns, respectively. The fourth and fifth columns correspond to the frequencies and respective energy content obtained by FFT of the periodically sampled DNS.

via FFT with respectively 96% vs. 71% of the energy in the dominant frequencies for the first mode, and 95% vs. 79% for the second. In other words, the compressive sampling solution requires less basis functions (frequencies) to capture a set percentage of streamwise turbulence intensity than the solution obtained with periodic sampling.

The advantage of compressive sampling over periodic sampling in the case of approximately sparse data will become even more evident at higher Reynolds number, because the dynamically significant frequency range increases with Reynolds number. Figure 3.13(b) shows the broadening of the frequency range resulting from an increase in Reynolds number by one order of magnitude compared to figure 3.13(a), implying that ten times more samples are needed to resolve the frequency content via periodic sampling. The number of samples required for compressive sampling scales as the logarithm of the bandwidth, leading to an exponential gain in terms of number of samples compared to periodic sampling.

Compressive sampling also provides a way to increase the frequency resolution as many more frequencies can be chosen to perform the optimization than the number of samples available. Figure 3.15 illustrates how the frequency resolution can be increased by using compressive sampling as opposed to periodic sampling. The sampled signal is composed of three Fourier modes  $e^{i2\pi ft}$  with frequencies  $f = 0.035, 0.052, 0.087$  and unit magnitude, sampled 50 times over 100 time units. In the case of periodic sampling, the minimum and maximum frequencies are given by  $f_{min} = 0.01$  and  $f_{max} = 0.49$ , and the PSD is shown on figure 3.15(a). The maximum frequency nearly equals the sampling frequency (not half the sampling frequency because the input signal is complex-valued). In the case of compressive sampling, two different resolutions were tested. The first one matches the periodic sampling case,  $df = f_{min} = 0.01$  and the second one is ten times higher  $df = 0.001$ .

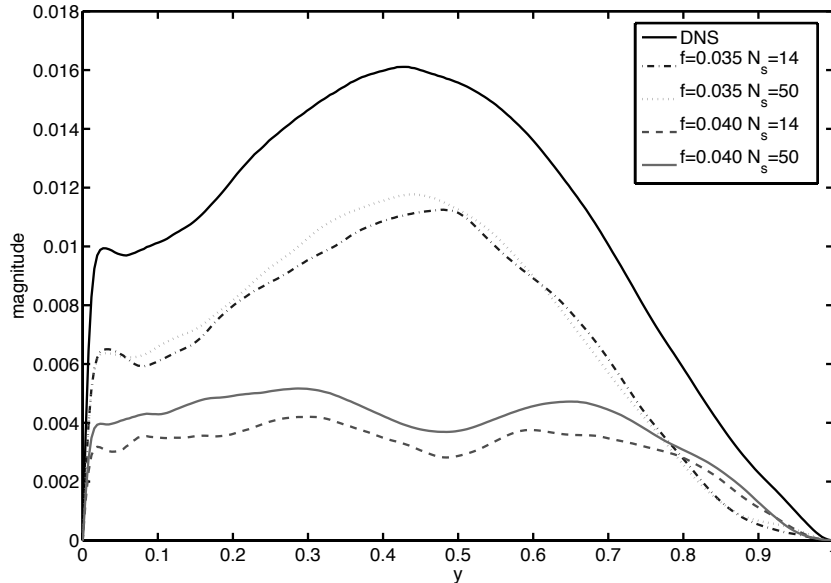


Figure 3.14: Comparison between the time-averaged wall-normal profile of the 2D Fourier mode  $(k, n) = (0.21, 2)$  from the randomly sampled DNS and its two sparse frequencies obtained using compressive sampling with 14 and 50 snapshots.

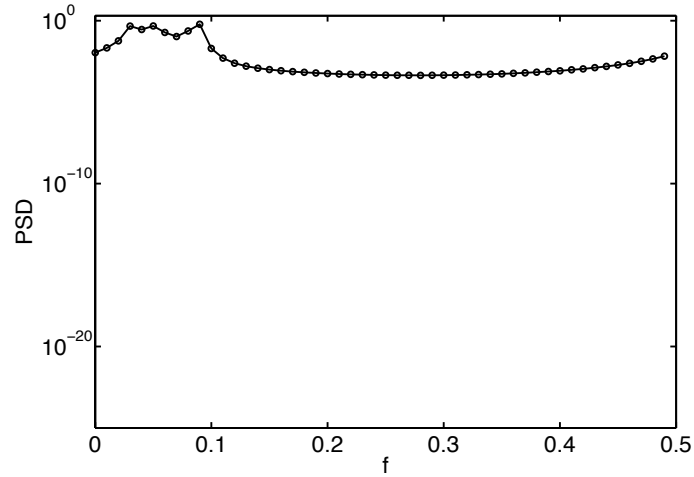
The PSDs are plotted on figure 3.15(b),(c) and show that for the higher-resolution case the three input frequencies were recovered exactly, because the set of Fourier modes used for the optimization includes the three input frequencies. For the lower resolution case, the PSD obtained via compressive sampling exhibits a lower level of noise, or equivalently, a sparser solution than the PSD obtained via FFT of periodic samples.

### 3.4 Summary

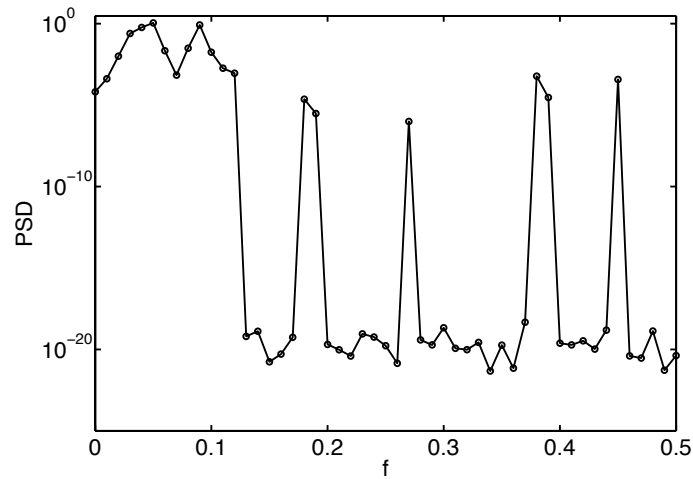
A novel application of compressive sampling to extract the frequency content of energetic modes in wall-bounded turbulence was presented. It was shown that compressive sampling can be applied if the flow field is expanded as a Fourier series in the homogeneous wall-parallel directions, as proposed by McKeon & Sharma (2010).

The use of compressive sampling in wall-bounded turbulence was validated by performing tests based on synthetic velocity fields with known frequency content that approximate the DNS flow fields. Compressive sampling successfully extracted the correct frequencies from the synthetic flow fields, and did so with significantly fewer samples than predicted by the Nyquist criterion. Equivalently, compressive sampling was shown to be able to resolve frequencies up to six times higher than the mean sampling rate.

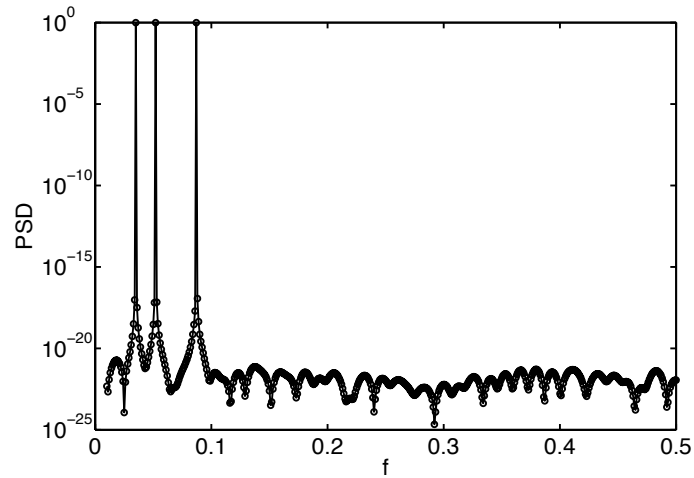
Frequency analysis of periodically sampled turbulent pipe flow DNS data revealed that the fre-



(a)



(b)



(c)

Figure 3.15: Power spectral density of a superposition of three Fourier modes with unit magnitude and frequencies  $f = 0.035, 0.052, 0.087$  sampled 50 times during 100 time units computed using (a) periodic sampling with FFT, and (b) compressive sampling with a frequency increment of  $df = 0.01$  and (c)  $df = 0.001$ .

quency content of each 2D Fourier mode is indeed approximately sparse. The 2D Fourier modes correspond to a superposition of propagating waves that are coherent in the wall-normal direction, and convect downstream at a speed between 10 times the friction velocity and the centerline velocity. It was predicted that 50 samples, randomly distributed over 100 dimensionless time units, are sufficient to resolve via compressive sampling all the dynamically significant time scales in turbulent pipe flow at  $Re = 24,580$ .

Compressive sampling was applied to a broad range of energetic 2D Fourier modes of streamwise extent varying from the longest modes ( $k = 0.21$ ) to the near-wall type modes ( $k = 4.3, \lambda^+ = 1,000$ ) at  $Re=24,580$ . The frequency content was shown to be approximately sparse, and falls in between the two empirical bounds on the convection velocity, corresponding to modes convecting at 10 times the friction velocity and the centerline velocity. The frequencies obtained via compressive sampling are robust with respect to variations of the optimization parameters, as long as the sparsity relationship is satisfied.

When only a limited amount of data is available, compressive sampling can resolve more 2D Fourier modes than periodic sampling, and results in higher frequency resolution. The advantage of compressive sampling over periodic sampling will become even more evident as higher Reynolds numbers are reached by numerical simulations resulting in broader dynamically significant bandwidths, since the number of samples required to resolve a given bandwidth with compressive sampling scales as the logarithm of the bandwidth instead of linearly.

Compressive sampling is used in the next chapter to significantly reduce the data requirements for a full modal decomposition of turbulent pipe flow, in the three spatial directions and in time, and results in sparse representations of the flow in the frequency domain.

## Chapter 4

# Sparse Representation of Turbulent Pipe Flow by Propagating Waves and a Model-Based Radial Basis

### 4.1 Introduction

A variety of measurements in wall-bounded turbulence has revealed the presence of coherent and persistent structures extending over large regions of the flow domain. While many definitions of coherent structures exist in the literature, Berkooz *et al.* (1993) offer a description of organized spatial features which repeatedly appear and evolve in time in a characteristic way; this is the definition we will adopt in this work.

Recently, Smits *et al.* (2011) categorized coherent structures in order of increasing streamwise lengthscale as follows: the well-known (and well-studied) near-wall streaks identified by Kline *et al.* (1967), the horseshoe or hairpin vortices described by Theodorsen (1952), large scale motions (LSMs) of the order of the outer flow lengthscale that are thought to constitute the packets of hairpins detailed by Adrian (2007), and the very large scale motions (VLSMs) of order ten times the outer lengthscale, e.g., Kim & Adrian (1999). Experimental capture of this full range of coherent structures can be extremely challenging due to their large extents in the wall-parallel directions, evolution and varying degree of localization in the wall-normal direction. This translates to the requirement for high spatial resolution, large field-of-view, time-resolved simultaneous volumetric measurements of the velocity field, a challenge even for the state-of-the-art volumetric experimental techniques such as tomographic or holographic particle image velocimetry (PIV). Planar measurements that meet the spatial resolution requirements have been reported in the literature for several years, e.g., the streamwise wall-normal plane measurements of Meinhart & Adrian (1995), while relatively recent advances in the temporal capability of commercial systems have enabled time-resolved measurements in the wall-parallel plane, albeit at relatively low turbulent Reynolds numbers (Dennis & Nickels,

2008; LeHew *et al.*, 2011).

While significant progress has been made in identifying each class of coherent structures over the past couple of decades, efforts to assemble low-order models that capture both statistical and structural information have been generally less successful. In particular, the correct bases by which to characterize them remains a question of current investigation.

One such approach is the decomposition of wall-bounded turbulence into modes ranked by energetic contribution, obtained by Proper Orthogonal Decomposition (POD). POD is defined based on an inner product  $(\mathbf{g}^a, \mathbf{g}^b)$ , a norm  $\|\mathbf{g}\|$ , and an averaging operation  $\langle \cdot \rangle$  (Berkooz *et al.*, 1993). In turbulence, the inner product is usually chosen to correspond to the turbulent kinetic energy

$$(\mathbf{g}^a, \mathbf{g}^b) = \int_{\Omega_{fl}} \sum_{i=1}^3 g^{a,i}(X)g^{b,i}(X)dX, \quad (4.1)$$

where  $\mathbf{g}^a$  and  $\mathbf{g}^b$  are zero-mean 3-component velocity fields,  $\Omega_{fl}$  is the flow domain, and the norm is defined as  $\|\mathbf{g}\| = (\mathbf{g}, \mathbf{g})^{\frac{1}{2}}$ . Liu *et al.* (2001) showed that the POD basis is optimal in the sense that the POD expansion converges faster than any other modal expansion based on the energy norm (equation (4.1)). The 3 components of velocity POD modes  $\Phi(X)$  correspond to the eigenmodes of the ensemble averaged velocity cross-correlation tensor

$$\int_{\Omega_{fl}} \langle \mathbf{u}(X)\mathbf{u}(X') \rangle \Phi(X')dX' = \lambda \Phi(X). \quad (4.2)$$

The POD modes for the streamwise velocity fluctuations are denoted  $\phi(X)$  and are eigenmodes of

$$\int_{\Omega_{fl}} \langle u(X)u(X') \rangle \phi(X')dX' = \lambda \phi(X). \quad (4.3)$$

In the statistically homogeneous directions, Berkooz *et al.* (1993) showed that the POD modes correspond to Fourier modes. Thus, for a fully-developed case such as turbulent pipe flow, for which the only inhomogeneous direction is the wall-normal one, the full POD modes take the form

$$\Phi(x, r, \theta, t) = \sum_{k,n,\omega} \mathbf{c}_{k,n,\omega}(r) e^{i(kx+n\theta-\omega t)}, \quad (4.4)$$

where  $(x, r, \theta)$  are the streamwise, radial and azimuthal directions normalized by the pipe radius, respectively, and  $(k, n, \omega)$  are the streamwise and spanwise wavenumbers and the temporal (angular) frequency. The wall-normal distance  $y$  is also normalized by the pipe radius (or the channel half-height when referring to channel flow studies). The wall-normal coherence of the structures is captured through the functions  $\mathbf{c}_{k,n,\omega}(r)$ , the basis for which is to be determined. This representation enforces homogeneity in the streamwise and azimuthal/spanwise directions and statistical steadiness.

The POD kernel is then parameterized by  $(k, n, \omega)$ , and depends only on the wall-normal distance; however determining this full kernel from observations involves averaging over many time-resolved flow realizations, which requires acquiring and processing a very significant amount of data.

To reduce the data requirements, averaging in one or more homogeneous directions or in time is commonly used instead of Fourier decomposition to approximate the POD kernel. Duggleby *et al.* (2009) compared the Fourier method (based on time average) to the method of snapshots (based on spatial average) to compute the POD modes, and showed that the former method converges faster, but requires more modes to capture a set percentage of the energy in a given finite-time realization. Those authors emphasized that the two methods should yield the same basis functions as the sampling duration tends to infinity. Here, we review some recent studies to highlight the implementation and effects of decreasing amounts of averaging.

Baltzer & Adrian (2011) performed a POD of the streamwise velocity fluctuations of a Direct Numerical Simulation (DNS) of turbulent channel flow at  $Re_\tau=180, 395, \text{ and } 934$ , based on averaging in the two homogeneous directions  $(x, z)$  and in time. The POD modes then simplify to functions of the wall-normal distance,  $y$ , alone,

$$\phi(x, y, z, t) = \bar{c}(y), \quad (4.5)$$

and are solutions of the eigenvalue problem

$$\int_{-1}^1 \langle u(y)u(y') \rangle \bar{c}(y') dy' = \lambda \bar{c}(y), \quad (4.6)$$

where  $\langle \cdot \rangle$  denotes an average over the streamwise and spanwise directions and in time. The resultant POD modes were characterized as either large scale or small scale. The large-scale modes captured most of the energy and were specific to the flow configuration, whereas the small-scale modes contributed most to the energy dissipation and were hypothesized to be asymptotically self-similar and universal.

Hellstroöm *et al.* (2011) used 2D+time Particle Image Velocimetry (PIV) in the cross-stream plane in a turbulent pipe flow at  $Re=12,500$  ( $Re_\tau \approx 375$ , computed based on the friction factor measured at  $Re=13,650$  by Swanson *et al.* (2002)) to perform a POD of the streamwise velocity fluctuations in physical space, without spatial averaging or Fourier decomposition, to investigate the structure of the VLSMs. There the POD modes took the form

$$\phi(x, r, \theta, t) = \phi(r, \theta, t), \quad (4.7)$$

such that

$$\int_0^T \int_0^{2\pi} \int_0^1 \langle u(r, \theta, t)u(r', \theta', t') \rangle \phi(r', \theta', t') r' dr' d\theta' dt' = \lambda \phi(r, \theta, t), \quad (4.8)$$

where  $\langle \cdot \rangle$  here denotes an average over several flow realizations. The time evolution of the POD modes was converted into streamwise evolution using Taylor's hypothesis and the local mean velocity, leading to a set of three-dimensional POD modes. The results showed that only a small number of modes was required to reconstruct characteristics of the VLSMs.

Duggleby *et al.* (2007) performed a POD analysis of turbulent pipe flow DNS data at  $Re = 4300$  ( $Re_\tau = 150$ ) using a Fourier decomposition in the streamwise and azimuthal directions and a time average. The POD modes,

$$\Phi(x, r, \theta, t) = \sum_{k,n} \mathbf{c}_{k,n}(r) e^{i(kx+n\theta)}, \quad (4.9)$$

were obtained by solving

$$\int_0^1 \langle \mathbf{u}_{k,n}(r) \mathbf{u}_{k,n}^*(r') \rangle \mathbf{c}_{k,n}(r') r' dr' = \lambda_{k,n} \mathbf{c}_{k,n}(r), \quad (4.10)$$

where  $\langle \cdot \rangle$  here denotes a time average, and \* the complex conjugate. The full flow field was represented as a sum of POD modes

$$\mathbf{u}(x, r, \theta, t) = \sum_{k,n,q} a_{k,n,q}(t) \mathbf{c}_{k,n,q}(r) e^{i(kx+n\theta)}, \quad (4.11)$$

where  $q$  is the POD mode order, or quantum number (corresponding in this case to the number of zero crossings of the mode amplitude plus one) and the  $a_{k,n,q}(t)$  are amplitude coefficients obtained by projection of the POD modes onto the flow field. The POD modes were classified either as propagating or nonpropagating. The propagating modes had a constant phase speed and time-varying magnitude; such modes were shown to capture 89% of the total turbulent kinetic energy. The physical interpretation is of propagating waves that evolve (grow and decay) in time, highlighting that the statistical steadiness of the flow is not enforced and a manifestation of lack of temporal convergence.

When the Fourier decomposition is applied in all homogeneous directions and in time, the resulting modal expansion of the flow field associated with the modes given by equation (4.4),

$$\mathbf{u}(x, r, \theta, t) = \sum_{k,n,\omega} \mathbf{c}_{k,n,\omega}(r) e^{i(kx+n\theta-\omega t)}, \quad (4.12)$$

can be interpreted as a sum of propagating waves with complex-valued coefficients  $\mathbf{c}_{k,n,\omega}(r)$ , parameterized by a wavenumber pair and frequency, and with variation in the wall-normal distance. Such a parametrization is consistent with the usual spectral representation of data obtained in experiments and simulation. However, further physical insight can also be obtained; Morrison *et al.* (1971) used experimental data to decompose the buffer layer as a sum of propagating waves, and concluded that the propagating waves are of dynamical importance due to their coherence in the wall-normal

direction.

In practice, the numerous time-resolved 3D realizations of the flow required to assemble the ideal POD kernel and to ensure the data independence of the basis functions have precluded the use of a data-based POD kernel for the modal decomposition of the propagating waves. One method of reducing the data requirements is to introduce a model basis for the radial direction and form what we will term a model-based kernel. McKeon & Sharma (2010) described such a basis in their systems analysis of turbulent pipe flow. Since this basis will be used in the work described below, we will give a brief introduction to the approach here.

The analysis presented by McKeon & Sharma (2010) utilized a Fourier decomposition of the Navier-Stokes (NS) equations in the homogeneous directions (for the reasons given above, these are the optimal bases), such that the velocity field can be written as the sum of propagating waves

$$\mathbf{u}(x, r, \theta, t) = \sum_{k,n,\omega} a_{k,n,\omega} \mathbf{c}_{k,n,\omega}(r) e^{i(kx+n\theta-\omega t)}, \quad (4.13)$$

where the  $a_{k,n,\omega}$  are complex-valued coefficients representing the relative magnitude and phase of the waves. The (normalized) radial basis functions, called velocity response modes,  $\mathbf{c}_{k,n,\omega}(r)$ , are to be determined but are constrained to be divergence free in order to eliminate the influence of pressure. For each  $(k, n, \omega)$ , then, the NS equations can be written in the form

$$i\omega \mathbf{c}_{k,n,\omega}(r) = \mathcal{L}_{k,n,\omega}(r) \mathbf{c}_{k,n,\omega}(r) + \mathbf{f}_{k,n,\omega}(r), \quad (4.14)$$

where  $\mathbf{f}_{k,n,\omega}(r)$  is the projection of the nonlinear terms onto the Fourier basis and

$$\mathcal{L}_{k,n,\omega}(r) = \begin{bmatrix} \mathcal{A}Re^{-1} + ikU & \mathcal{B}Re^{-1} & 0 \\ -\mathcal{B}Re^{-1} & \mathcal{A}Re^{-1} + ikU & 0 \\ -\partial_r U & 0 & (\mathcal{A} - r^{-2})Re^{-1} + ikU \end{bmatrix}, \quad (4.15)$$

where  $\mathcal{A} = -\partial_{rr} - r^{-1}\partial_r + n^2r^{-2} + k^2 + r^{-2}$ ,  $\mathcal{B} = 2inr^{-2}$  and the mean flow velocity profile  $\mathbf{U} = (0, 0, U)^T$  constitutes an input to the analysis. The first to third lines of the resolvent correspond to the radial, azimuthal, and streamwise velocity components, respectively.

Under this formulation, the velocity can be seen as a response of the flow system to the forcing  $\mathbf{f}_{k,n,\omega}(r)$  via the transfer function  $H_{k,n,\omega} = (i\omega I - \mathcal{L}_{k,n,\omega}(r))^{-1}$ , commonly called the resolvent (Trefethen & Embree, 2005), i.e.,

$$\mathbf{c}_{k,n,\omega}(r) = H_{k,n,\omega} \mathbf{f}_{k,n,\omega}(r) = (i\omega I - \mathcal{L}_{k,n,\omega}(r))^{-1} \mathbf{f}_{k,n,\omega}(r). \quad (4.16)$$

McKeon & Sharma (2010) utilized the discrete version of the Schmidt decomposition, the singular value decomposition (SVD), and a turbulent kinetic energy norm to decompose the transfer function into a set of orthonormal forcing and response modes (the left and right singular vectors, respectively)

$$(i\omega I - \mathcal{L}_{k,n,\omega}(r))^{-1} = \sum_{q=1}^{\infty} \mathbf{c}_{k,n,\omega,q}(r) \sigma_{k,n,\omega,q} \mathbf{f}_{k,n,\omega,q}^*(r), \quad (4.17)$$

where \* denotes the complex conjugate, and with

$$\int_0^1 \mathbf{f}_{k,n,\omega,q}(r) \mathbf{f}_{k,n,\omega,l}^*(r) r dr = \delta_{ql}, \quad (4.18)$$

$$\int_0^1 \mathbf{c}_{k,n,\omega,q}(r) \mathbf{c}_{k,n,\omega,l}^*(r) r dr = \delta_{ql}, \quad (4.19)$$

and subject to the normalizations

$$\int_0^1 f_{k,n,\omega,q}^r(r) f_{k,n,\omega,q}^{r*}(r) r dr + \int_0^1 f_{k,n,\omega,q}^\theta(r) f_{k,n,\omega,q}^{\theta*}(r) r dr + \int_0^1 f_{k,n,\omega,q}^x(r) f_{k,n,\omega,q}^{x*}(r) r dr = 1, \quad (4.20)$$

and

$$\int_0^1 c_{k,n,\omega,q}^r(r) c_{k,n,\omega,q}^{r*}(r) r dr + \int_0^1 c_{k,n,\omega,q}^\theta(r) c_{k,n,\omega,q}^{\theta*}(r) r dr + \int_0^1 c_{k,n,\omega,q}^x(r) c_{k,n,\omega,q}^{x*}(r) r dr = 1. \quad (4.21)$$

At each  $(k, n, \omega)$ , the forcing mode  $\mathbf{f}_{k,n,\omega,q}(r)$  gives rise to a corresponding response mode  $\mathbf{c}_{k,n,\omega,q}(r)$  with amplification  $\sigma_{k,n,\omega,q}$ , with  $\sigma_q \geq \sigma_{q+1} \geq 0$ , where the mode order, called the quantum number in Duggeby *et al.* (2007), is denoted here by  $q$ . Thus, the first singular velocity response mode corresponds to the forcing mode that gives rise to the largest amplification (quantified by the first singular value), and so on. For an arbitrary forcing mode

$$\mathbf{f}_{k,n,\omega}(r) = \sum_{q=1}^{\infty} a_{k,n,\omega,q} \mathbf{f}_{k,n,\omega,q}(r), \quad (4.22)$$

the response is given by

$$\mathbf{c}_{k,n,\omega}(r) = \sum_{q=1}^{\infty} a_{k,n,\omega,q} \sigma_{k,n,\omega,q} \mathbf{c}_{k,n,\omega,q}(r). \quad (4.23)$$

McKeon & Sharma (2010) employed a rank-1 approximation of the resolvent, considering only the first singular mode and unstructured (unit) forcing, under the hypothesis that the first singular velocity response mode would be likely to be observed in a real flow if it contained a nonzero component of forcing in the direction of the first singular mode and the first singular value satisfied  $\sigma_1 \gg 1$  and  $\sigma_1 \gg \sigma_2$ . They showed that the first velocity response modes displayed characteristics in close agreement with key known features of wall turbulence, from the near-wall motions to the

VLSMs, and appeared to obey the scalings obtained from classical (viscous) critical layer analysis, despite the cylindrical coordinate system in the pipe.

Experimental mean flow velocity profiles,  $\mathbf{U} = (0, 0, U)^T$ , were used to form the resolvent in this study, but the analysis can be made self-consistent in the sense that the mean profile is supported by the Reynolds stresses associated with all  $(k, n, c, q)$  modes if the  $a_{k,n,\omega,q}$  are chosen appropriately (equivalent to structuring the forcing correctly for maintenance of the turbulence). While the work of McKeon & Sharma (2010) was analytical, a data-driven approach can be used to project out the  $a_{k,n,\omega,q}$  coefficients from direct numerical simulation; this is the primary function of the present chapter.

The previous chapter explored the use of compressive sampling in wall-bounded turbulence to perform such a projection (in essence equivalent to obtaining the full POD kernel described earlier), and the concomitant reductions in data storage required to project out the velocity response modes from direct numerical simulations of turbulent pipe flow. We apply this technique here in order to obtain sparse representations of the flow to investigate the structure of turbulence and its sustaining mechanisms.

In what follows, we describe the use of a model-based modal decomposition of turbulent pipe flow that preserves the coherence of the structures in the wall-normal direction, and significantly reduces the data requirements compared to a classical POD analysis, because of the use of a new POD kernel and compressive sampling. This consists, in essence, of the application of the modeling approach of McKeon & Sharma (2010) to the velocity field output from a direct numerical simulation. In section 4.2, we describe our approach and the data set under consideration. The results of the analysis after decomposition in each component are presented in section 4.3, in order to facilitate comparison with results in the literature for which the full decomposition in  $(x, y, \theta, t)$  is rarely presented. A discussion of the success and limitations of the approach of McKeon & Sharma (2010), and in particular the usefulness of the SVD in forming a radial basis for decomposition of the data, and the implications of the results for understanding of the flow dynamics future modeling is given in section 4.4.

## 4.2 Methodology

Fully developed turbulent pipe flow DNS velocity fields for this study were kindly provided by X. Wu, as an extension of the study reported in Wu & Moin (2008), where full details of the (second-order finite difference) code can be found. The simulation was performed at  $Re = 24,580$ . The corresponding friction Reynolds number was  $Re_\tau = 685$ . All the lengthscales were normalized with respect to the pipe radius. The domain length was  $30R$  and the coordinate system is sketched in figure 4.2. The velocity fields were subsampled by a factor of 4 in the streamwise and azimuthal

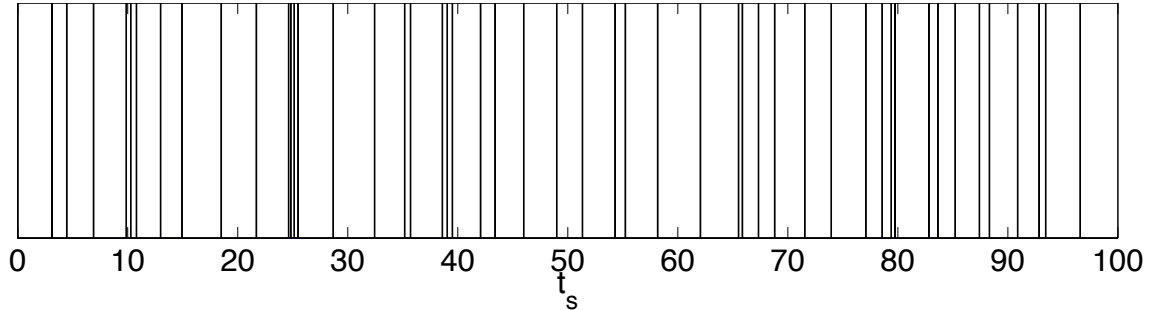


Figure 4.1: The 50 DNS sampling time instants randomly distributed over 100 dimensionless time units based on the radius and bulk velocity. The last sampling time instant is at  $t = 96.57$ .

directions for data reduction purposes, such that the number of grid points in the streamwise, azimuthal, and radial directions was respectively  $512 \times 256 \times 256 \approx 33 \times 10^6$  compared to  $\approx 540 \times 10^6$  for the full field. This subsampling was shown to have negligible effect on the streamwise velocity profile and streamwise turbulence intensity.

The dataset under consideration consisted of fifty velocity fields randomly distributed over 100 dimensionless time units based on the pipe radius and bulk velocity, as shown in figure 4.1. The number of samples and sampling duration were chosen based on extensive testing and validation of compressive sampling in wall-bounded turbulence, presented in the previous chapter, in order to resolve most of the energetic timescales of the streamwise velocity fluctuations. The sampling duration of 100 dimensionless time units based on the pipe radius and bulk velocity corresponds to twice the timescale associated with the longest structures ( $L = 30R$ ) traveling at the lowest convection velocity observed in wall turbulence  $u_c = 10 u_\tau$  (Morrison *et al.*, 1971), or  $0.45 U_{CL}$  at this Reynolds number. The data set containing the fifty velocity fields constitutes one time-resolved realization of turbulent pipe flow. The focus in this study is on the long wavelength structures of the streamwise velocity field due to this imposed data constraint and the important role they play in the dynamics of turbulent pipe flow. The streamwise velocity component is the only velocity component considered in this study, because the frequency content of the azimuthal and radial velocity fields could not be resolved with the available data.

The analysis consisted of a Fourier decomposition of the velocity field information in the homogeneous streamwise and azimuthal directions, using a 2D Fast Fourier Transform (FFT), followed by the use of compressive sampling to recover the energetic temporal frequencies,  $\omega$ , corresponding to the convection velocities  $u_c = \frac{\omega}{k U_{CL}}$ , at each spatial wavenumber pair,  $(k, n)$ . Decomposition in the final, wall-normal direction was achieved using the SVD of the appropriate resolvent operator,  $H_{k,n,\omega}$ . A schematic of the approach is shown in figure 4.3, and we describe each decomposition step in the following subsections.

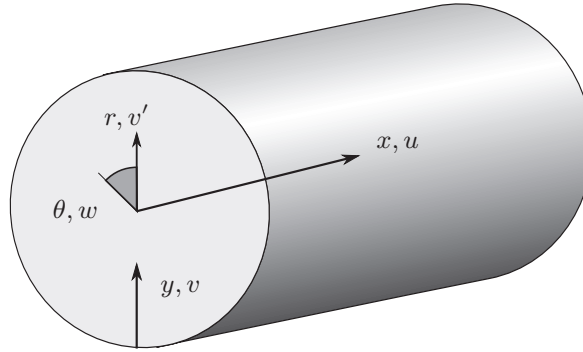


Figure 4.2: Schematic of pipe geometry and nomenclature.

### 4.2.1 Decomposition in the Streamwise and Azimuthal Directions

The streamwise velocity fields were Fourier transformed in the streamwise and azimuthal directions using a 2D FFT

$$u(x, r, \theta, t) = \sum_{k,n} c_{k,n}(r, t) e^{i(kx+n\theta)}, \quad (4.24)$$

and normalized such that

$$\sum_{k=0}^{255k_{min}} \sum_{n=-128}^{127} c_{k,n}(r) c_{k,n}^*(r) = u'^2(r), \quad (4.25)$$

where  $k$  and  $n$  denote the streamwise and azimuthal wavenumbers, respectively, and  $k_{min} = \frac{\pi}{15}$  for a domain length of  $30R$ . These 2D spatial Fourier modes will be referred to by their wavenumber pair, henceforth “ $(k, n)$  modes” or 2D Fourier modes.

The 2D spectrum is symmetric because the velocity field is real, hence only the positive  $k$  half plane was retained. Another symmetry is present in the time-averaged spectrum, due to the statistical invariance of turbulent pipe flow under azimuthal reflection, allowing the  $(k, n)$  parameter space to be reduced to one quadrant. (Note, however, that this symmetry does not apply to the instantaneous spectra, i.e., those obtained from only one velocity field.)

The 2D Fourier spectrum corresponding to each velocity field was integrated in the wall-normal direction to identify the  $(k, n)$  modes that contribute most to the streamwise turbulence intensity, and a time average formed over the fifty samples. The  $(k, n)$  modes were ranked by their time averaged contribution to the streamwise turbulence intensity, and only the energetically dominant modes were considered for further study.

### 4.2.2 Decomposition in Time

The dominant 2D Fourier,  $(k, n)$ , modes were decomposed as a Fourier series in time with minimum  $\ell_1$ -norm using compressive sampling, following the technique described in the previous chapter. Instead of applying compressive sampling at each wall-normal location separately, the minimization

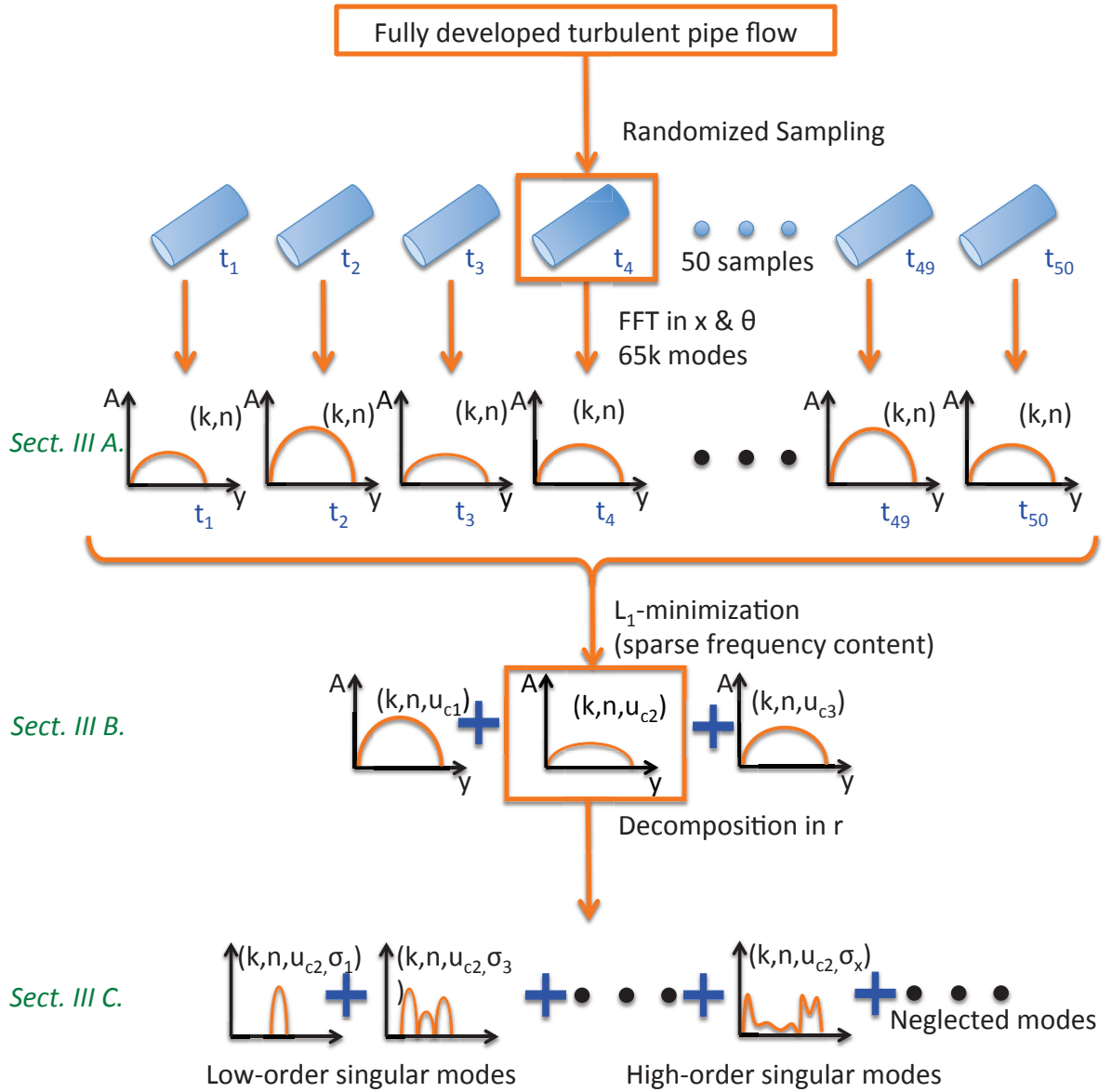


Figure 4.3: Block diagram representing the decomposition of fully developed turbulent pipe flow as a sum of propagating waves.

was performed only once on the  $\ell_2$ -norm of the 2D Fourier modes in the wall-normal direction, under the constraint that the reconstructed signal should equal the input signal at every sampling time instant  $t_s$  (figure 4.1) and wall-normal location  $r_q$ , i.e.,

$$\sum_{j=1}^{N_{opti}} c_{k,n,2\pi jdf}(r_q) e^{i2\pi jdf t_s} = c_{k,n}(r_q, t_s), \forall t_s, \forall r_q. \quad (4.26)$$

Here,  $N_{opti}$  and  $df$  are optimization variables corresponding respectively to the number of frequencies and the frequency increment for the optimization, which were set to  $N_{opti} = 400$  and  $df = 0.005$  based on the discussion in the previous chapter, as these parameters constituted a good balance between increasing the resolution and satisfying the sparsity relationship (equation (3.1)). The resulting frequency range for the minimization is from  $-1$  to  $1$ . Note that the 2D Fourier modes were interpolated on a uniform grid in the radial direction, and the coefficients premultiplied by  $\sqrt{r}$ , prior to performing the optimization, such that the  $\ell_2$ -norm corresponded to the energy norm in cylindrical coordinates. After the optimization, the mode coefficients were divided by  $\sqrt{r}$ .

The minimization problem of equation (4.26), i.e., the minimization of

$$\sum_{j=1}^{N_{opti}} \int_0^1 c_{k,n,2\pi jdf}(r) c_{k,n,2\pi jdf}^*(r) r dr, \quad (4.27)$$

was solved with Matlab using the CVX toolbox for convex optimization, to determine the sparse frequency content of the energetically dominant 2D Fourier modes. A sparse frequency was defined for this study to contain not less than 10% of the peak value at the most energetic frequency. Note that the temporal Fourier modes determined by compressive sampling are velocity field specific and are not orthogonal on the set of randomized sampling time instants, such that Parseval's theorem does not apply.

The resultant (three-dimensional) Fourier modes were parameterized by  $(k, n, u_c)$  where  $u_c = \frac{\omega}{kU_{CL}} = \frac{2\pi f}{kU_{CL}}$  is a convection velocity normalized by the centerline velocity. These  $(k, n, u_c)$  Fourier modes are complex-valued and depend only on the radial coordinate. Based on the sampling parameters chosen for the DNS, it was observed that only the streamwise velocity component had a sparse frequency content for a broad range of 2D Fourier modes.

### 4.2.3 Decomposition in the Radial Direction

The SVD of the resolvent was used to obtain a set of basis functions for expansion of the velocity field in the wall-normal direction. The singular velocity response modes were computed using a version of the spectral code of Meseguer & Trefethen (2003) modified by McKeon & Sharma (2010) to allow for the input of any velocity profile, and the decomposition into singular modes of the

resolvent. The mean velocity profile from the DNS (Wu & Moin, 2008) was used as an input to the spectral code. McKeon & Sharma (2010) showed that the leading singular modes are extremely robust to numerical error, and the SVD exists if the resolvent has no purely imaginary eigenvalue, which is the case for both the laminar and turbulent pipe flow velocity profiles. The former case is a consequence of the linear stability of laminar pipe flow (Meseguer & Trefethen, 2003), and the latter case was checked numerically for the DNS turbulent pipe flow velocity profile at  $Re = 24,580$ .

For a given resolution  $N$ , the basis contains  $2(N + 1)$  modes discretized on  $N + 3$  grid points in the radial direction. The resolution was chosen to be  $N = 256$ , high enough for the leading singular modes to be converged. The DNS Fourier modes and the singular modes were interpolated onto the same equispaced grid before projecting the former onto the latter.

In the case of the projection of three velocity component Fourier modes from the DNS onto the singular response modes, the projection coefficients,  $P_q$ , would be given by

$$P_q = \frac{(\mathbf{c}_{k,n,c}, \mathbf{c}_{k,n,c,q})}{(\mathbf{c}_{k,n,c}, \mathbf{c}_{k,n,c})^{\frac{1}{2}}}, \quad q = 1, 2, \dots, 514, \quad (4.28)$$

where  $\mathbf{c}_{k,n,c}$  is the DNS Fourier mode,  $\mathbf{c}_{k,n,c,q}$  is the  $q^{\text{th}}$  singular mode and the  $\mathbf{c}_{k,n,c,i}$ 's are orthonormal such that

$$(\mathbf{c}_{k,n,c,i}, \mathbf{c}_{k,n,c,j}) = \int_0^1 (c_{k,n,c,i}^r c_{k,n,c,j}^r + c_{k,n,c,i}^\theta c_{k,n,c,j}^\theta + c_{k,n,c,i}^x c_{k,n,c,j}^x) r dr = \delta_{ij}. \quad (4.29)$$

The inner product  $(\mathbf{g}_{k,n,c}^a, \mathbf{g}_{k,n,c}^b)$ , based on the modal turbulent kinetic energy, is given by

$$(\mathbf{g}_{k,n,c}^a, \mathbf{g}_{k,n,c}^b) = \int_0^1 (g_{k,n,c}^{a,r} g_{k,n,c}^{b,r} + g_{k,n,c}^{a,\theta} g_{k,n,c}^{b,\theta} + g_{k,n,c}^{a,x} g_{k,n,c}^{b,x}) r dr, \quad (4.30)$$

where  $\mathbf{g}_{k,n,c}^a, \mathbf{g}_{k,n,c}^b$  are complex-valued, three components of velocity Fourier coefficients depending on the radial coordinate only.

However, in this study, only the streamwise velocity component was investigated, so the singular modes were modified to satisfy the scalar orthonormality condition

$$(c_{k,n,c,i}, c_{k,n,c,j}) = \int_0^1 c_{k,n,c,i}^x c_{k,n,c,j}^x r dr = \delta_{ij}, \quad (4.31)$$

by performing a QR decomposition of the streamwise velocity component of the singular modes interpolated on an equispaced grid and premultiplied by  $\sqrt{r}$ , such that the  $\ell_2$ -norm corresponds to the energy norm in cylindrical coordinates. The resulting mode coefficients, divided by  $\sqrt{r}$ , are referred to as the streamwise singular modes. The first 3 - 4 modes were not affected by the QR decomposition, at least to plotting accuracy as shown on figure 4.4; however the amplitude distribution of the higher-order singular modes was distorted nonuniformly over the radius, reflecting

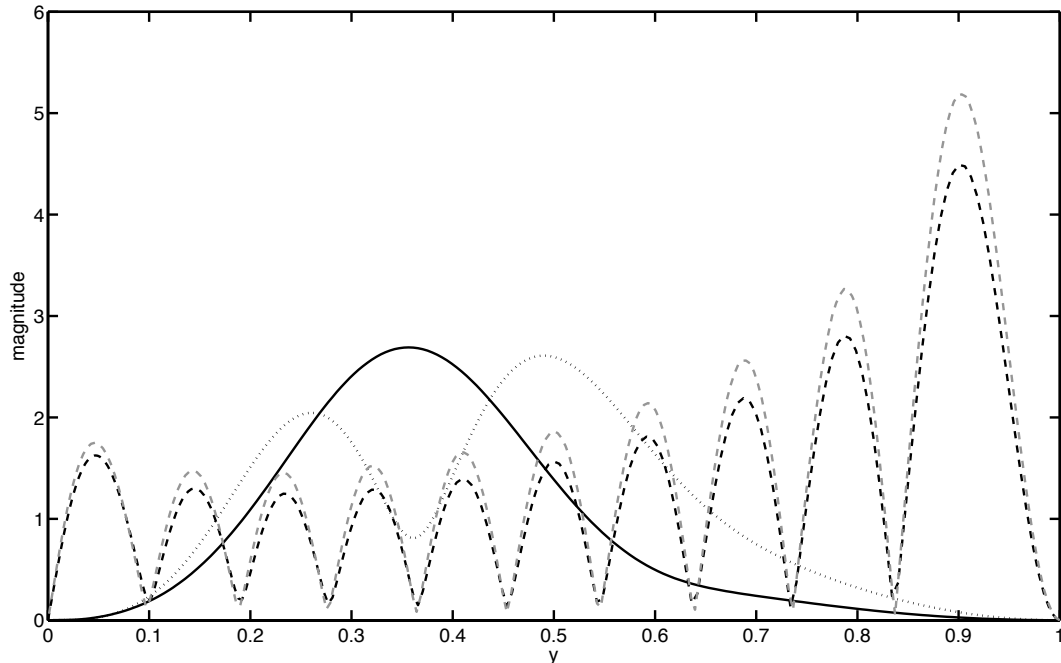


Figure 4.4: Comparison of the first (solid), second (dotted), and tenth (dashed) singular mode profiles of the streamwise velocity component before (black) and after (gray) applying the QR decomposition for the set of parameters (0.21, 2, 0.83). For the first two modes, the profiles before and after QR decomposition are identical to plotting accuracy.

the relative energetic content of the cross-stream velocity components in these modes. The model-based radial decomposition of the DNS Fourier modes corresponds to a truncated series of singular modes with relative magnitude and phase given by the projection coefficients.

#### 4.2.4 Proper Orthogonal Decomposition

A POD of the DNS data used in this study was performed as a benchmark for comparison with the model-based modal decomposition described here. The POD kernel is based on the velocity cross-correlation tensor, Fourier transformed in the streamwise and azimuthal directions to take into account the flow homogeneity in these directions. The kernel is parameterized by  $(k, n)$ , and assembled by averaging in time the energy of the 2D Fourier coefficients  $\langle c_{k,n}(r, t)c_{k,n}^*(r, t) \rangle$ , following the method described in Duggeby *et al.* (2007), but using samples randomized in time instead of periodic. The POD modes correspond to the eigenmodes of the kernel, and depend only on the wall-normal distance. The time information is captured by the amplitude coefficients, obtained by projection of the POD modes onto the velocity fields. The POD modes are then multiplied by their time-varying amplitude coefficients for comparison to the propagating waves extracted using the full modal decomposition.

$(k, n)$	% $u'^2$	$(k, n)$	% $u'^2$
(0.21,2)	1.97	(0.21,-1)	0.49
(0.42,-3)	1.11	(0.63,-5)	0.48
(0.42,3)	0.96	(0.21,3)	0.45
(0.21,-3)	0.79	(0.42,-2)	0.43
(0.21,4)	0.51	(0.63,-2)	0.43

Table 4.1: Top 10  $k \neq 0$  2D Fourier modes and percentage of the time-average (over the 50 randomly sampled velocity field) streamwise turbulence intensity captured.

## 4.3 Results

The results associated with the complete decomposition of turbulent pipe flow, in the three spatial directions and in time, described above, are presented piecewise in this section, with emphasis placed on the information obtained by each decomposition step, as sketched in figure 4.3. For each stage, an evaluation of the number of modes required to capture a significant fraction of the streamwise turbulence intensity is given, followed by a comparison of the wall-normal profiles and contours of the streamwise velocity fluctuations in a streamwise wall-normal plane between the truncated modal decomposition and the original signal. At the end of the section, a comparison between the classical POD analysis and the present modal decomposition steps is presented.

### 4.3.1 Two-dimensional Fourier Modes ( $\mathbf{k}, \mathbf{n}$ )

Before considering the shapes of individual 2D Fourier modes, the variation of the cumulative turbulence intensities for the three velocity components, and of the cumulative turbulent kinetic energy, as a function of the number of  $(k, n)$  modes, was investigated for a single snapshot. Figure 4.5 shows that 485 and 8692 2D Fourier modes are required to capture respectively 50% and 90% of the streamwise turbulence intensity, compared to the 65,536 modes resolved in the (subsampling) DNS field. The streamwise turbulence intensity converges faster than the azimuthal and wall-normal intensities and so is particularly suited to low-order approximations and the type of modeling effort undertaken here.

Analysis of the radially integrated, 2D  $(k, n)$  spectrum for one representative DNS velocity field shows that the 2D Fourier modes contributing most to the integrated streamwise turbulence intensity have low streamwise and azimuthal wavenumbers. (The streamwise-constant modes are not considered in this study, due to the aliasing of the modes longer than  $30R$  onto  $k = 0$ .) The ten  $(k, n)$  modes with  $k \neq 0$  contributing most to the time-averaged streamwise intensity (averaged over the 50 available DNS velocity fields), accounting for 7.6% of  $u'^2$ , are listed in table 4.1; the first 51 modes all have a wavelength longer than  $4R$  and contain 20% of the streamwise turbulence intensity. A representative wall-normal profile of these modes is shown for  $(k, n) = (0.21, 2)$  in figure 4.6. These most energetic 2D Fourier modes are tall in the wall-normal direction, extending from the

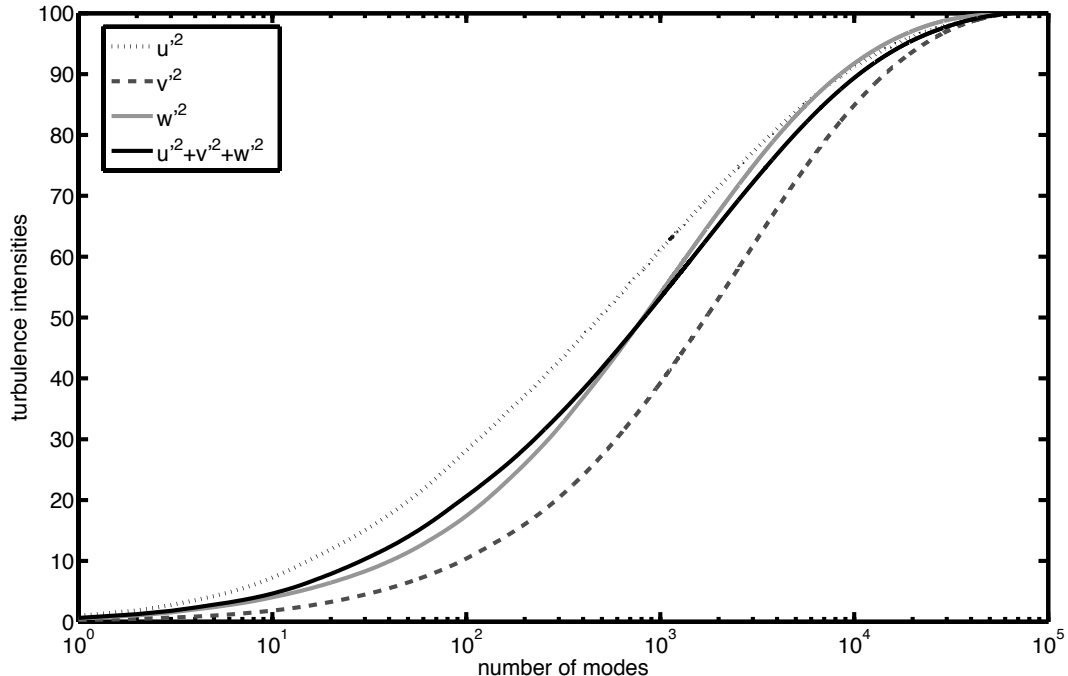


Figure 4.5: Convergence of the turbulence intensities and kinetic energy as a function of the number of 2D Fourier modes for one representative DNS snapshot.

wall all the way to the core of the pipe.

Figure 4.7 shows a comparison between contours of streamwise velocity fluctuations in a streamwise wall-normal plane ( $\theta = 0$ ) from a single DNS velocity field, Fourier filtered in the streamwise direction to remove small scales above  $k = 2$ , using a sharp cutoff after the ninth streamwise Fourier mode, and a reconstructed field using a superposition of only the first 51 most energetic 2D Fourier modes. Both fields exhibit streamwise-inclined, large-scale regions of high and low momentum, extending from the wall up to  $y = 1 - r \approx 0.7$ , and reminiscent of the streamwise velocity fields computed in wall-bounded turbulence by Chung & McKeon (2010) using conditional averaging based on the large-scale velocity and a filter width equal to the channel half height. The correlation coefficient between the Fourier filtered velocity field in a streamwise-azimuthal plane and the reconstructed flow field, averaged in the streamwise and azimuthal directions, is higher than 70%. The large value of the correlation coefficient implies that, although the 2D Fourier modes were ranked by their contribution to the *radially-integrated* streamwise turbulence intensity, they are also locally dominant in the sense that are highly correlated with the full DNS field throughout the flow, with the exception of the regions very close to the wall and centerline area, as can be observed visually in figure 4.7.

In this subsection, we showed that the most energetic 2D Fourier modes ( $k, n$ ) are coherent in the wall-normal direction. The magnitude and phase of the modes evolve in time in a nonsimple way, such that identification of the temporal harmonic components is required to obtain a time-invariant decomposition, and is described in the next subsection.

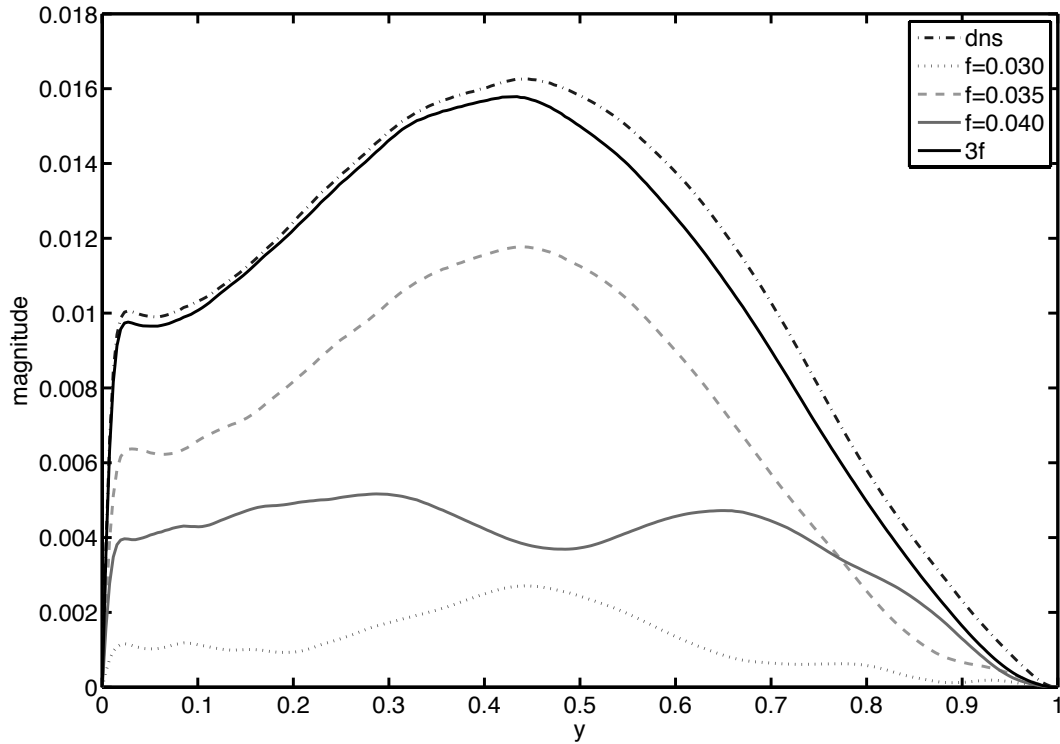


Figure 4.6: Time average wall-normal profile of the 2D Fourier mode  $(k, n) = (0.21, 2)$  compared to the reconstructed profile using only the three dominant frequencies. The profiles of the Fourier modes  $(0.21, 2, u_c)$  at the three dominant frequencies corresponding to the convection velocities  $u_c = 0.71, 0.83, 0.95$  are also shown for comparison.

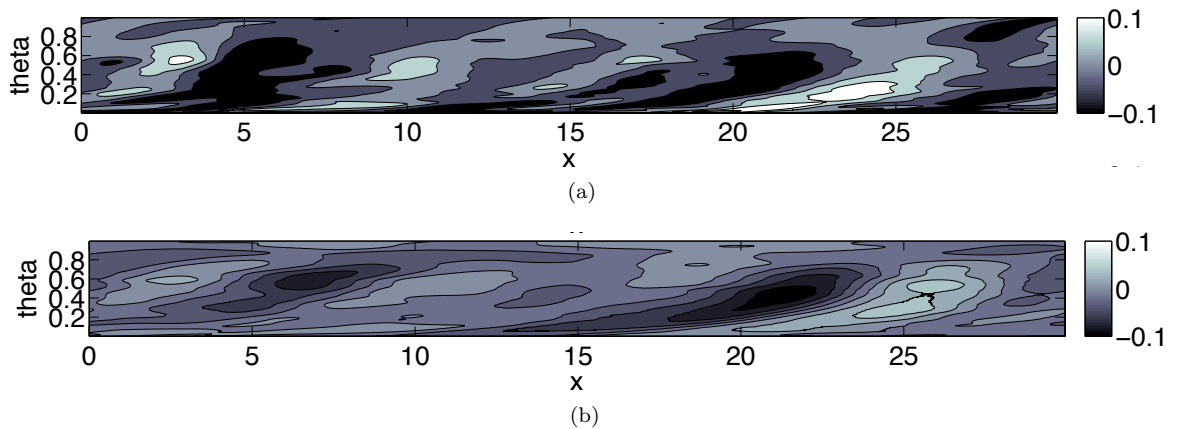


Figure 4.7: Contour plots of streamwise velocity fluctuations at  $\theta = 0$  for the DNS flow field Fourier filtered in the streamwise direction (a) and the Fourier series approximation with 51  $(k, n)$  modes capturing 20% of the streamwise turbulence intensity (b).

### 4.3.2 Fourier Modes ( $\mathbf{k}, \mathbf{n}, \mathbf{u}_c$ )

Application of compressive sampling to the temporal variation of the 2D Fourier modes revealed sparse frequency content; under the definition in section 4.2.2, each 2D Fourier mode considered was found to contain between 1 and 5 sparse frequencies, within the resolution error of  $df = \pm 0.0025$ . The frequencies fell in a range bounded by those corresponding to the lowest and highest convection velocities identified in wall turbulence, namely  $u_{c,min} = 0.45$  and  $u_{c,max} = 1$  at  $Re=24,580$ .

Figure 4.6 shows the wall-normal variation of the amplitude of three dominant frequency components identified for the  $(k, n, u_c) = (0.21, 2, u_c)$  mode, which are representative of observations for the other energetic modes. Three sparse frequencies, corresponding to the convection velocities  $u_c = 0.71, 0.83,$  and  $0.95$ , were identified, which together capture 91% of the streamwise turbulence intensity compared to 52% for the peak frequency alone. For each frequency component, energy is distributed across the whole radius, and the reconstructed mode, namely the superposition of these three dominant frequencies, gives a good representation of the time-averaged profile associated with the  $(k, n)$  mode.

Figure 4.8 shows a comparison of the time evolution of the reconstructed mode amplitude, and of the 2D Fourier mode amplitude, as a function of the wall-normal distance. The presence of multiple frequencies in the reconstructed mode leads to temporal amplitude variation, in good agreement with the variation observed in the 2D Fourier mode.

The structures reconstructed by superposition of increasing numbers of  $(k, n, u_c)$  modes, henceforth “propagating waves,” with all the sparse frequencies included are visualized by the contours of streamwise momentum in a wall-normal streamwise plane in figure 4.9. Two different time instants are shown, separated by half a period of the longest structures, or equivalently 14.3 dimensionless time units, in order to demonstrate the evolution of the structural coherence. As the number of propagating waves increases, the resemblance between the reconstructed flow and the DNS flow field under the spatial Fourier filter described above increases, with 16  $(k, n)$  combinations leading to a reasonable reproduction of at least the large-scale features of the flow field. The reconstructed flow field is dynamic and evolves in time in a manner akin to the flow realization. The propagating waves have constant magnitude in time, but their relative motion leads to the growth and decay of the structures, which can only be captured if the time evolution of the flow is resolved. The 16 2D Fourier modes included in the reconstructed flow field on figure 4.9 constitute only 0.025% of the total number of modes in the subsampled DNS, but they contain about 10% of the time-averaged streamwise turbulence intensity.

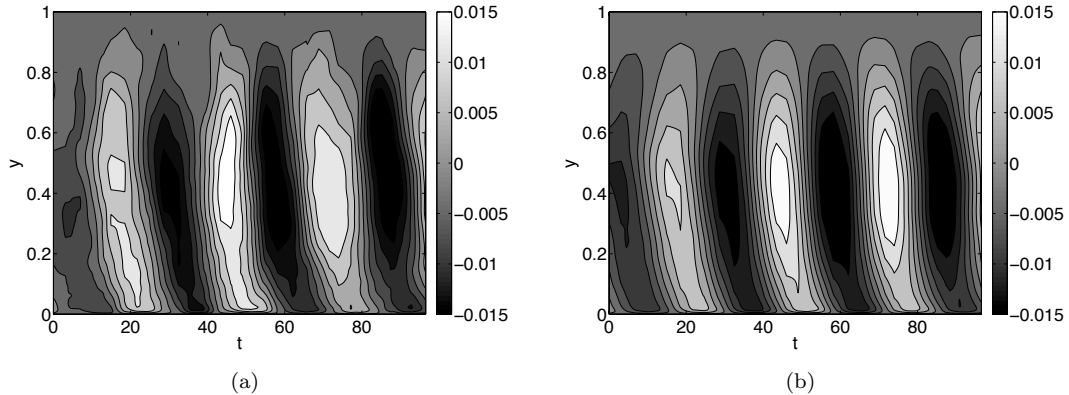


Figure 4.8: Contours of the real part of the 2D Fourier mode  $(k, n) = (0.21, 2)$  as a function of the wall-normal distance and time with all the frequencies included (a) and with only the three dominant frequencies included (b). The contours are obtained by interpolation between the randomly sampled velocity fields, and plotted at  $\theta = 0$  and  $x = 0$ .

### 4.3.3 Streamwise Singular Modes $(k, n, u_c, q)$

The final decomposition of the propagating waves,  $(k, n, u_c)$ , in the radial direction into streamwise singular modes,  $(k, n, u_c, q)$ , revealed additional sparsity. Figure 4.10(a) – (d) shows the distributions of amplitude and phase for the first six singular modes associated with the propagating wave  $(k, n, u_c) = (0.21, 2, 0.83)$ , which will be analyzed in detail as a representative example of the long, energetic streamwise wavelength structures. The first singular mode has only one peak, centered near the critical-layer, and has a phase that decreases with wall-normal distance in the region where the magnitude is large, indicating that the mode is inclined in the downstream direction. The singular modes of order  $q \leq 6$  for this set of parameters  $(k, n, u_c) = (0.21, 2, 0.83)$  have  $q - 1$  local minima inside the flow domain (excluding the centerline) and vanish at the wall and centerline. The separation between the local peaks situated, respectively, closest to the wall and to the centerline, increases with  $q$ , implying that the energy of the singular modes is spread over a wider region in the wall-normal direction. A phase jump is associated with each local minimum. In between the jumps, the phase decreases or stays constant in the wall-normal direction, again indicating that the modes are leaning in the downstream direction. The energy and cumulative energy captured as a function of the streamwise singular mode order  $q$  are plotted on figure 4.10(e),(f). The energy decreases monotonically with  $q$  such that the modes of order higher than 10 represent less than 1% of the amount of energy contained in the first mode. The cumulative energy plot shows that only 6 modes are required to capture 95% of the Fourier mode energy, suggesting that the decomposition of the propagating waves as a sum of singular modes leads to a sparse representation in the wall-normal direction. The projection method is robust with respect to the number of fields included in the Fourier decomposition.

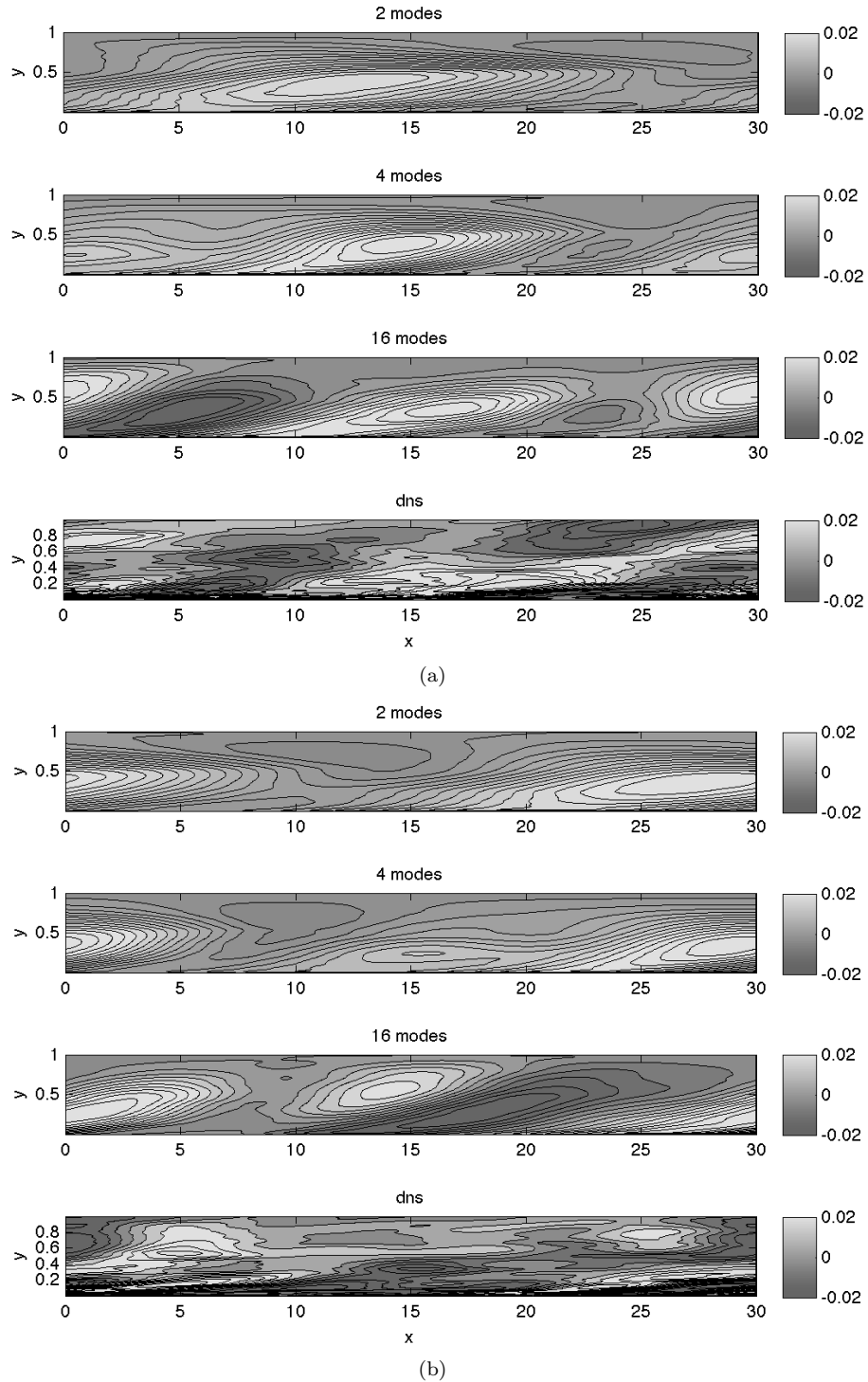


Figure 4.9: Contours of the streamwise velocity fluctuations in the streamwise and wall-normal directions at two different time instants separated by half a period of the longest structures or about 14.3 dimensionless time units. The velocity fields from top to bottom are reconstructed based on a superposition of respectively the top 2, 4, and 16 dominant  $(k,n)$  wavenumber pairs with all the sparse frequencies included. The bottom velocity field correspond to the DNS data Fourier filtered to remove the small scales.

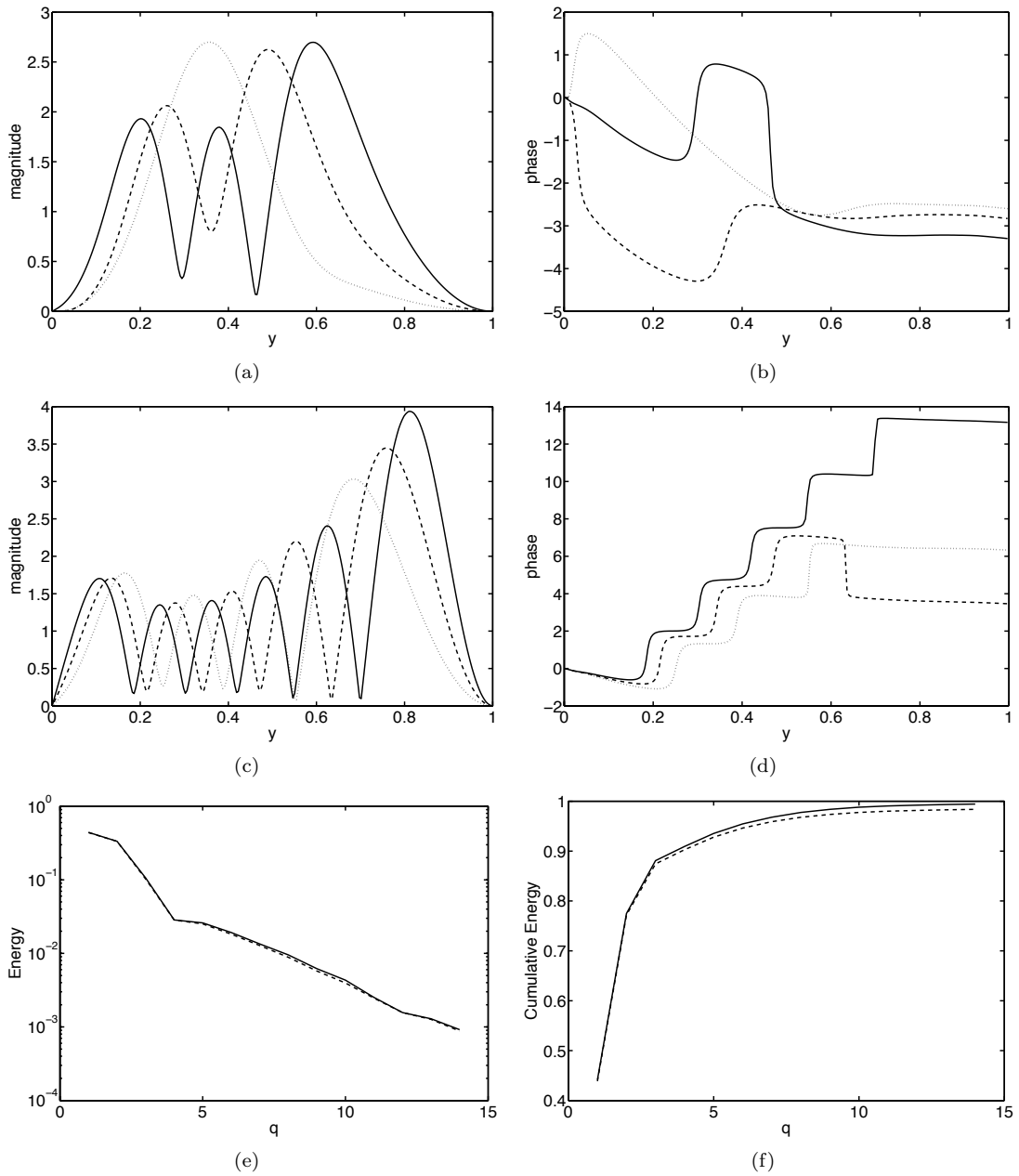
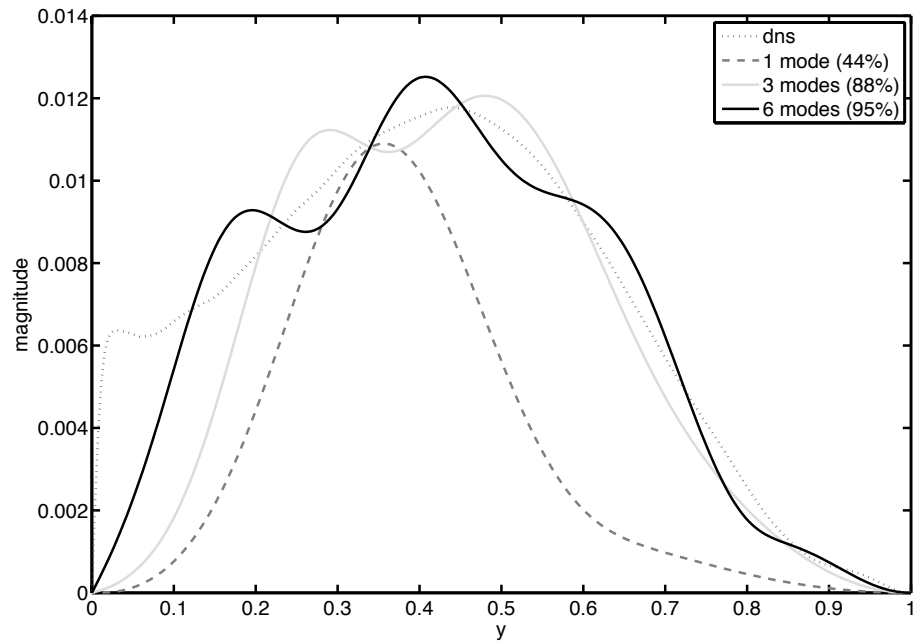
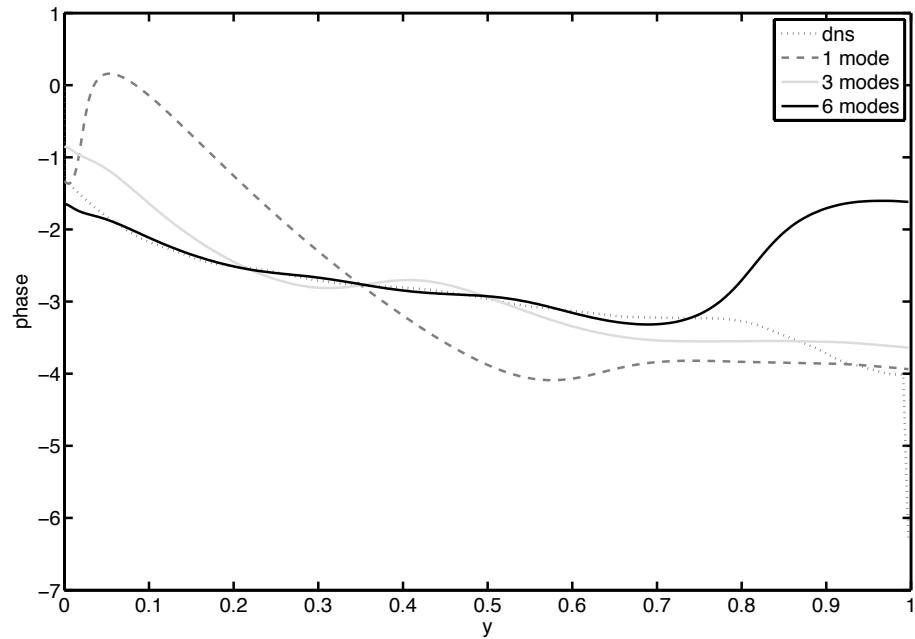


Figure 4.10: Wall-normal profiles for the magnitude (a),(c) and phase (in radians) (b),(d) of the singular modes (a),(b)  $(k, n, u_c, q) = (0.21, 2, 0.83, 1)$  (dotted),  $(0.21, 2, 0.83, 2)$  (dashed), and  $(0.21, 2, 0.83, 3)$  (solid); and (c),(d)  $(0.21, 2, 0.83, 4)$  (dotted),  $(0.21, 2, 0.83, 5)$  (dashed), and  $(0.21, 2, 0.83, 6)$  (solid). Energy (e) and cumulative energy (f) captured as a function of the mode order and normalized by the DNS mode energy  $u'^2$  with (solid) and without (dashed) QR orthonormalization.



(a)



(b)

Figure 4.11: Wall-normal profiles for the magnitude (a) and phase (in radians) (b) of a superposition of 1  $(k, n, u_c, q) = (0.21, 2, 0.83, 1)$ , 3  $(0.21, 2, 0.83, 1 : 3)$ , and 6  $(0.21, 2, 0.83, 1 : 6)$  singular modes compared to the Fourier mode  $(k, n, u_c) = (0.21, 2, 0.83)$  magnitude and phase profiles.

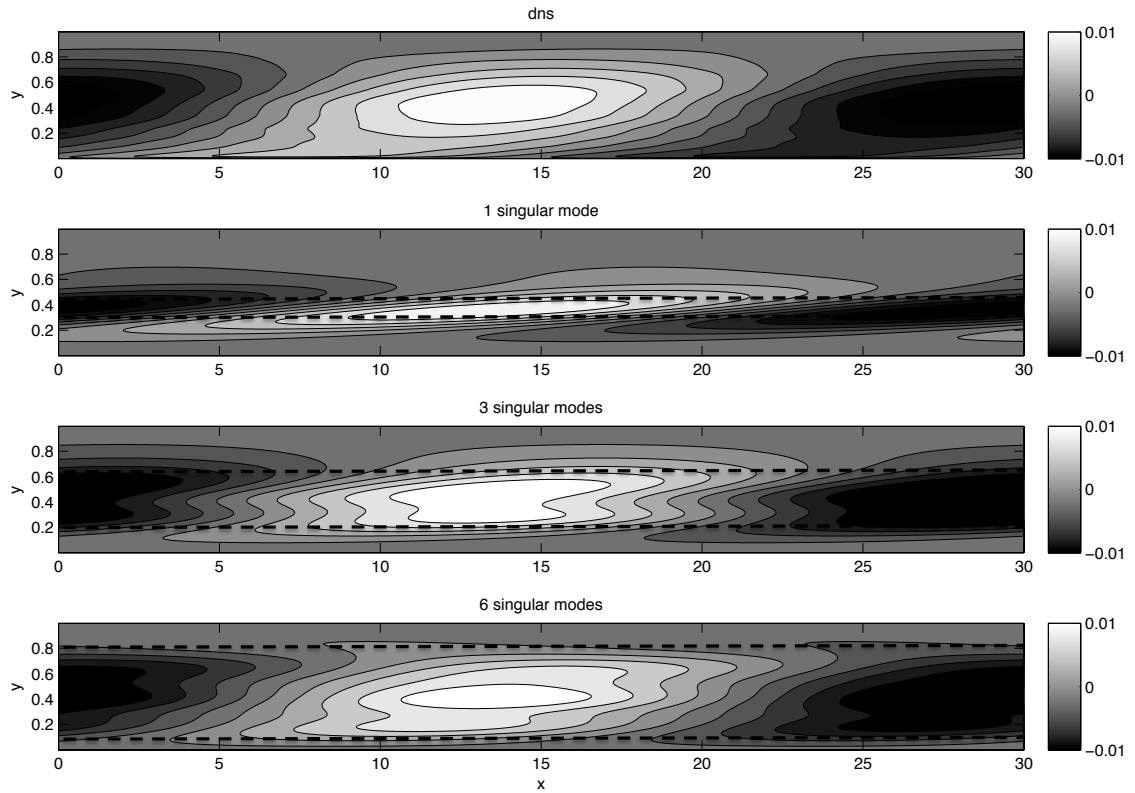


Figure 4.12: Contours of the streamwise velocity fluctuations in a streamwise wall-normal plane for the Fourier mode  $(k, n, u_c) = (0.21, 2, 0.83)$  and its representation as a sum of respectively 1  $(k, n, u_c, q) = (0.21, 2, 0.83, 1)$ , 3  $(0.21, 2, 0.83, 1 : 3)$ , and 6  $(0.21, 2, 0.83, 1 : 6)$  singular modes (top to bottom). The horizontal dashed lines delimitate the region where the Fourier mode and its representation are in phase.

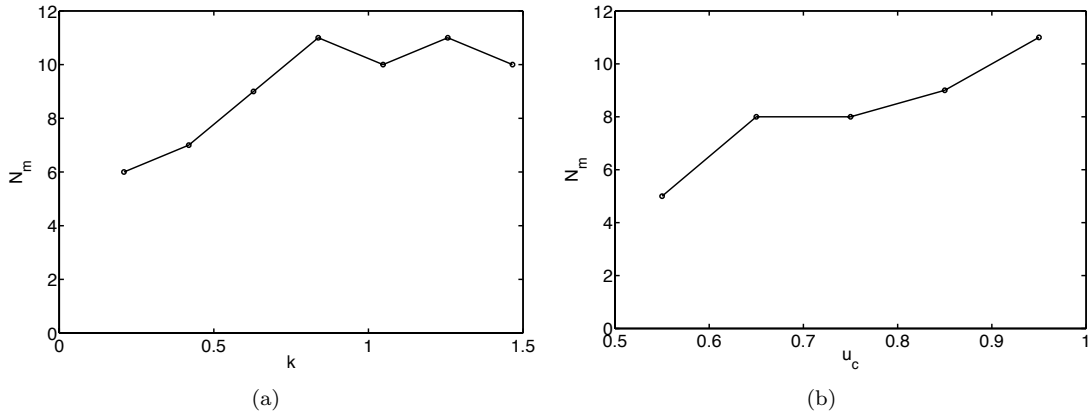


Figure 4.13: Average number of singular modes  $N_m$  required to capture 95% of  $u'^2$  as a function of the streamwise wavenumber (a) and convection velocity (b) based on the decomposition of 134 Fourier modes from the DNS turbulent pipe flow realization.

Figure 4.11(a),(b) shows the magnitude and phase of the DNS propagating wave  $(k, n, u_c) = (0.21, 2, 0.83)$  as a function of the wall-normal distance, compared to the series approximation truncated after the first, third, and sixth streamwise singular mode. The truncated series representation becomes broader, and matches the DNS phase over a wider region in the wall-normal direction, as the number of streamwise singular modes is increased. The corresponding velocity fields in the streamwise/wall-normal plane are shown in figure 4.12. The horizontal dashed lines delineate the region in the wall-normal direction where the phase of the series representation matches the DNS mode phase. As expected, the resemblance between the DNS mode and its series approximation improves as the number of singular modes is increased, particularly in the region where the phase variation is similar.

The average number of streamwise singular modes required to represent each Fourier mode, specifically to capture 95% of the energy of the streamwise fluctuations, was investigated by considering this projection method applied to 134 long streamwise wavelength Fourier modes. All the 134 Fourier modes have an azimuthal wavenumber lower or equal to 6. The results show that from 6 to 11 singular modes are required on average, depending on  $k$  and  $c$  for the range of streamwise wavenumbers  $k \in [0.21, 1.47]$ , compared to a total of 514 basis functions. The first singular mode captures from 40 to 50% of the propagating wave energy, for most of the long streamwise waves, i.e., for  $k \in [0.21, 1.47]$ . The number of streamwise singular modes required to capture 95% of the energy increases with  $k$  from 6 at  $k = 0.21$  to 10 - 11 for  $0.84 \leq k \leq 1.47$  and also increases with  $u_c$  from 5 at  $u_c = 0.55$  to 11 at  $u_c = 0.95$ , see figure 4.13. The increase in the number of streamwise singular modes required to capture a set percentage of energy with  $k$  can be explained by considering that the basis functions become narrower in the wall-normal direction with increasing  $k$ , but the radial extent of the propagating waves extracted from the DNS data appears independent of  $k$ , within the range

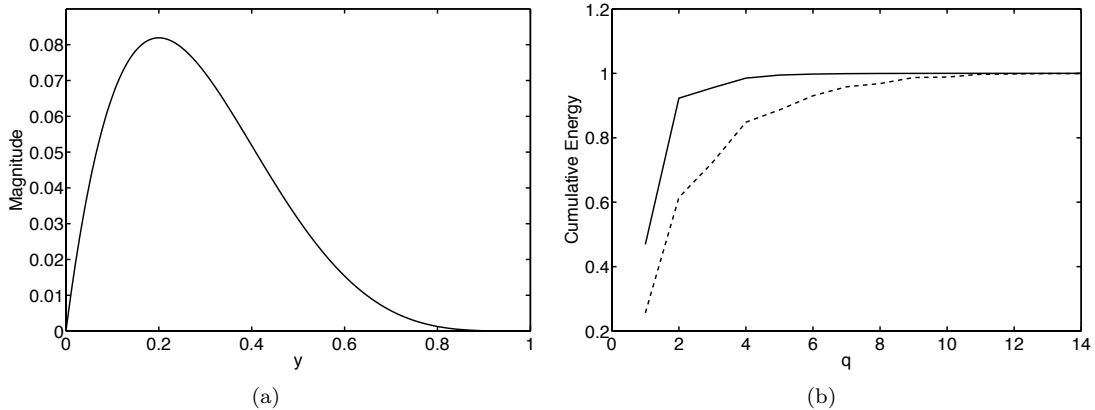


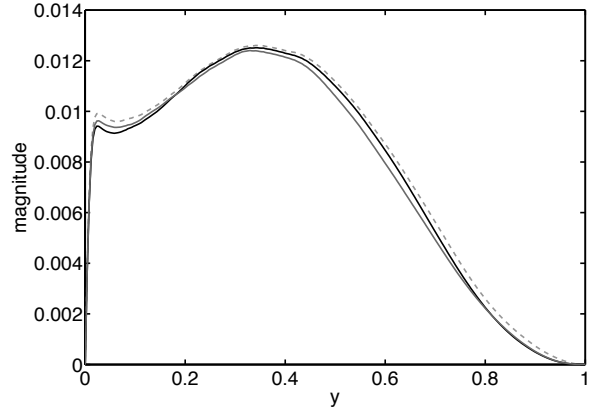
Figure 4.14: Wall-normal profile of the synthetic Fourier coefficient  $c_{k,n,\omega}(r) = (1-r)r^4$  (a). Number of streamwise singular modes required to capture 99% of the analytic Fourier coefficient energy at  $(k, n, u_c) = (0.21, 2, 0.77)$  (solid) and  $(k, n, u_c) = (1.47, 2, 0.77)$  (dashed) (b).

of streamwise wavenumbers  $k \in [0.21, 1.47]$  that could be resolved with the available DNS data. At higher  $k$ , we expect the radial extent of the propagating waves to depend on  $k$ . The increase with  $u_c$  is due to the shift of the critical layer location away from the wall, in regions where the DNS propagating waves have lower energy. An synthetic Fourier coefficient  $c_{k,n,\omega}(r) = (1-r)r^4$ , plotted on figure 4.14(a), which is independent of  $k$  and representative of the Fourier coefficients extracted from the DNS, was used to demonstrate that the number of streamwise singular modes required to capture 99% of the energy increases with  $k$ . Figure 4.14(b) shows that the number of streamwise singular modes increases from 5 at  $k = 0.21$  to 11 at  $k = 1.47$ , keeping  $u_c$  and  $n$  constant. The success of such a small number of singular modes (less than 5% of the total number of singular modes) in capturing a large amount of the energy suggests a reduction in order of the resolvent.

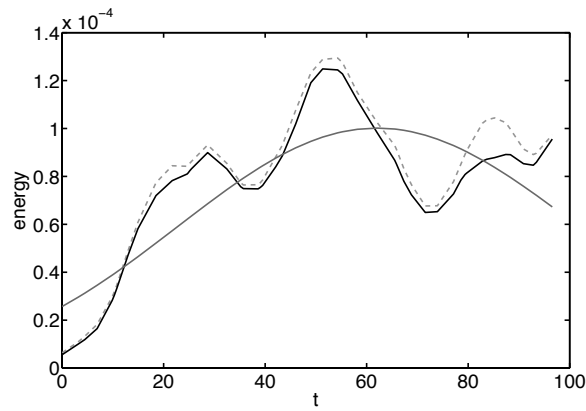
#### 4.3.4 Comparison with Proper Orthogonal Decomposition

The model-based modal decomposition presented in this chapter is compared to a POD of the same DNS data and to the POD analysis of turbulent pipe flow DNS data at  $Re = 4300$  by Dugleby *et al.* (2007), to identify the differences between these two methods, in terms of time-dependence of the modes and convergence of modal energy, when only a limited amount of data is available. The POD modes are computed following the method described in section 4.2.4.

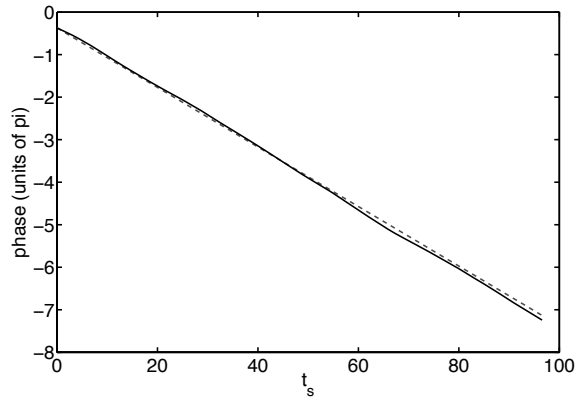
POD analysis of the most energetic 2D Fourier modes from the present DNS data shows that the first POD modes capture more than 95% of the streamwise turbulence intensity contained in each 2D Fourier mode. A representative example of the wall-normal profile, magnitude, and phase of first POD mode is shown on figure 4.15 for the 2D Fourier mode  $(0.21, 2)$ . This first POD mode has a constant phase speed and time-varying magnitude, similarly to the POD modes computed by Dugleby *et al.* (2007). In the case of compressive sampling, three frequencies are required to



(a)



(b)



(c)

Figure 4.15: Time-averaged wall-normal profile (a) and energy integrated in the wall-normal direction as a function of time (b) of the 2D Fourier mode  $(k, n) = (0.21, 2)$  (dashed) together with the first POD mode (solid, black) and the reconstructed 2D Fourier mode based on three dominant frequencies (solid, grey). Note that the temporal Fourier basis functions are not orthogonal on the set of randomized sampling time instants such that Parseval's theorem does not apply, i.e., the time average profile differs from the square root of the sum of the square of the three frequency components. (c) Phase of the time-varying amplitude coefficient of the first POD mode compared to the phase of the most energetic Fourier mode  $(k, n, u_c) = (0.21, 2, 0.83)$ . The phase of the Fourier mode depends on the wall-normal distance but the phase speed is constant. The origin of phase is chosen to match the POD mode.

	Duggleby <i>et al.</i> (2007)	Present Study
Re	4,300	24,580
$R^+$	150	685
L	20R	30R
$T_s$	5000	100
DOF	$2.6 \times 10^6$	$31 \times 10^6$
$N_{modes}$	2763	8700
Decomposition	$(k, n, q)$	$(k, n, u_c, q)$

Table 4.2: Comparison of the parameters for the Duggleby *et al.* (2007) POD analysis and the present modal decomposition including the sampling duration  $T_s$ , the number of degrees of freedom DOF (grid points) used to compute the modes, and the number of modes  $N_{modes}$  required to capture 90% of the TKE /  $u'^2$  for the two analyses, respectively. The last row indicates the order of the successive decompositions performed on the data.

capture more than 90% of the 2D Fourier mode energy, compared to one POD mode. However, the magnitude of each propagating wave, resulting from the modal decomposition, is constant, whereas the magnitude of the POD coefficients varies in time, in a non-simple way, due to the finite-time averaging. When the sampling duration tends to infinity, the coefficients of the POD modes should converge to the temporal Fourier modes obtained by compressive sampling, because the flow is statistically steady (Berkooz *et al.*, 1993).

The time evolution of the streamwise turbulence intensity, contained in the reconstructed 2D Fourier mode (0.21, 2) based on the three propagating waves, obtained by integrating the square of the amplitude in the wall-normal direction, is plotted on figure 4.15(b), and compared to the magnitude squared of the first POD mode. The smoother time-variation of the reconstructed mode is a consequence of the truncation of the Fourier series representation in time after the third-most energetic mode, i.e., the use of three sparse frequencies and neglect of other, significantly less energetic frequencies. The phase speed of the first POD mode is shown on figure 4.15(c) and matches the convection velocity of the most energetic propagating wave (0.21, 2, 0.83). We observed that there is a definite period to the DNS 2D Fourier mode and POD mode variations corresponding to an amplitude modulation of the signal at the same timescale as the one visualized on figure 4.8. However, for other 2D Fourier modes, the timescale of the first POD mode amplitude variations differs from the period of the Fourier mode. Although the POD and the propagating wave decomposition both converge, they do so in different ways.

The POD analysis of turbulent pipe flow DNS data by Duggleby *et al.* (2007) required 2763  $(k, n, q)$  modes to capture 90% of the turbulent kinetic energy (TKE) at a significantly lower Reynolds number of 4300 and over a domain length of  $20R$ , as opposed to 8700 2D Fourier modes in the present decomposition. The relevant parameters for the two decompositions are summarized in table 4.2. These two decompositions showed that the low  $(k, n)$  modes are the most energetic and are also tall in the wall-normal direction. Among the POD modes computed by Duggleby *et al.* (2007), the modes with  $q = 1$ , i.e., with no zero crossing, are the most energetic. Similarly, in the present

decomposition, about 40% to 50% of the energy is contained in the first singular mode with no zero crossing.

The time-varying POD coefficients need to be extracted from the data and saved at every sampling time instant, whereas for the propagating waves, only their relative magnitude and phase need to be saved. In addition, the flow decomposition as a superposition of propagating waves with model-based radial basis functions provides a link between the flow structures and the governing equations, described in the next section, allowing, for example, for the identification of the dominant amplification mechanisms sustaining the waves.

## 4.4 Discussion

The preceding section contained observations concerning the decomposition of real DNS velocity fields, using appropriate bases in all four dimensions. In this section, we advance the analytical treatment of the NS equations, in order to identify physical mechanisms sustaining different classes of modes, which can be identified as propagating waves with a radial amplitude variation. More precisely, we investigate the relative importance of non-normality and criticality on the amplification of the propagating waves, as a function of their streamwise wavenumber and mode order, and the constraints imposed by the dominant amplification mechanisms on the radial extent of the waves.

### 4.4.1 Componentwise Form of the Input-Output Relationship

The input-output relationship formulated by McKeon & Sharma (2010) (equation (4.16)) can be expanded to give

$$\begin{bmatrix} c_{k,n,\omega}^r \\ c_{k,n,\omega}^\theta \\ c_{k,n,\omega}^x \end{bmatrix} = \mathcal{R} \begin{bmatrix} f_{k,n,\omega}^r \\ f_{k,n,\omega}^\theta \\ f_{k,n,\omega}^x \end{bmatrix}, \quad (4.32)$$

where

$$\mathcal{R} = \begin{bmatrix} Re \mathcal{T}_1(\mathcal{D} + \mathcal{C} + r^{-2})^{-1} & Re \mathcal{T}_1(\mathcal{D} + \mathcal{C} + r^{-2})^{-1} \mathcal{B}(\mathcal{D} + \mathcal{C} + r^{-2})^{-1} & 0 \\ -Re \mathcal{T}_1(\mathcal{D} + \mathcal{C} + r^{-2})^{-1} \mathcal{B}(\mathcal{D} + \mathcal{C} + r^{-2})^{-1} & Re \mathcal{T}_1(\mathcal{D} + \mathcal{C} + r^{-2})^{-1} & 0 \\ -Re^2(\mathcal{D} + \mathcal{C})^{-1} DU \mathcal{T}_2(\mathcal{D} + \mathcal{C} + r^{-2})\mathcal{B}^{-1} & -Re^2(\mathcal{D} + \mathcal{C})^{-1} DU \mathcal{T}_2 & Re(\mathcal{D} + \mathcal{C})^{-1} \end{bmatrix}, \quad (4.33)$$

and

$$\mathcal{T}_1 = (\mathcal{I} + (\mathcal{D} + \mathcal{C} + r^{-2})^{-1} \mathcal{B} (\mathcal{D} + \mathcal{C} + r^{-2})^{-1} \mathcal{B})^{-1}, \quad (4.34)$$

$$\mathcal{T}_2 = (\mathcal{B} + (\mathcal{D} + \mathcal{C} + r^{-2}) \mathcal{B}^{-1} (\mathcal{D} + \mathcal{C} + r^{-2}))^{-1}, \quad (4.35)$$

$$\mathcal{B} = 2inr^{-2}, \quad (4.36)$$

$$\mathcal{C} = iRe(\omega - kU), \quad (4.37)$$

$$\mathcal{D} = -\partial_{rr} - r^{-1}\partial_r + n^2r^{-2} + k^2, \quad (4.38)$$

where  $\mathcal{I}$  is the identity operator. Here,  $\mathcal{D}$  is the Laplacian in cylindrical coordinates and can be interpreted as a dissipation term whose action is proportional to  $k^2$  and to the curvature in the radial direction. Therefore, the action of  $\mathcal{D}$  is large for modes that are short in the streamwise and radial directions (as opposed to spanning the whole radius). Phenomena associated with the existence of a critical layer are captured by  $\mathcal{C}$ , henceforth the criticality term, which vanishes at the critical layer.

Clearly, the norm of  $\mathcal{R}$  will be large, corresponding to large amplification of input disturbances,  $\mathbf{f}_{k,n,\omega}(r)$ , if both  $\mathcal{C}$  and  $\mathcal{D}$  are small. We investigate here the influence of these two terms on the output from the SVD. In the analysis that follows, the azimuthal wavenumber is set to  $n = 3$ , an energetically dominant azimuthal wavenumber in the DNS (see table 4.1), in order to make  $\mathcal{B}$  a function only of radius.

In order to quantify the distribution of forcing between the radial, streamwise and azimuthal directions, we introduce the forcing energy (correctly the forcing power per unit time),  $PF_{k,n,\omega,q}$ , defined as

$$PF_{k,n,\omega,q} = \int_0^1 \mathbf{f}_{k,n,\omega,q}(r) \mathbf{f}_{k,n,\omega,q}^*(r) r dr = 1, \quad (4.39)$$

and the streamwise

$$PF_{k,n,\omega,q}^x = \int_0^1 f_{k,n,\omega,q}^x(r) f_{k,n,\omega,q}^{x*}(r) r dr, \quad (4.40)$$

and azimuthal

$$PF_{k,n,\omega,q}^\theta = \int_0^1 f_{k,n,\omega,q}^\theta(r) f_{k,n,\omega,q}^{\theta*}(r) r dr, \quad (4.41)$$

contributions to the forcing energy  $PF_{k,n,\omega,q}$ . The radial contribution to  $PF_{k,n,\omega,q}$  is given by  $1 - PF_{k,n,\omega,q}^x - PF_{k,n,\omega,q}^\theta$  and is always low, for the range of streamwise and azimuthal wavenumbers considered in this study.

The dependence of the spatial distribution of the forcing and response energy on streamwise wavenumber and singular mode order,  $(k, q)$ , is considered on figure 4.16, for constant azimuthal wavenumber and convection velocity ( $n = 3$  and  $u_c = 0.8$ , representative of the range observed in the DNS data). The contours of the streamwise and azimuthal contributions to the forcing and response energy are plotted as a function of the streamwise wavenumber and singular mode order.

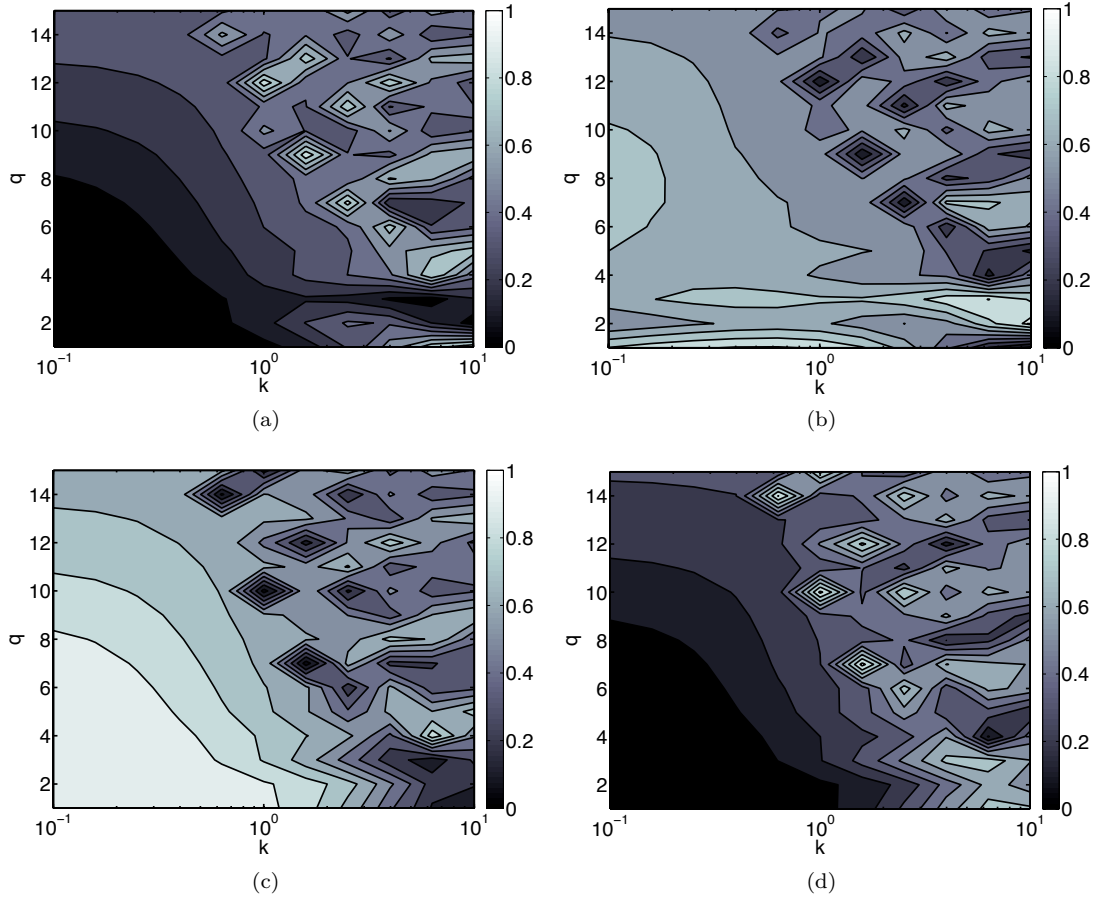


Figure 4.16: Streamwise (a),(c) and azimuthal (b),(d) contributions to the forcing (top row) and response (bottom row) energy, as a function of the streamwise wavenumber and singular mode order, in the presence of mean shear and for  $n = 3$ ,  $u_c = 0.8$ .

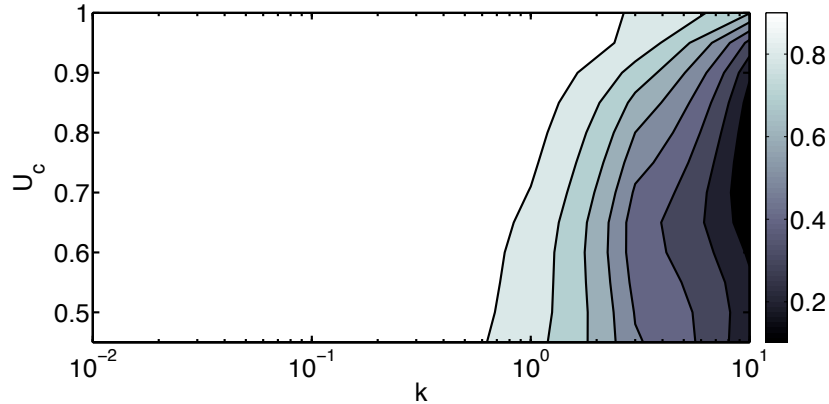


Figure 4.17: Cross-sectional contribution to the forcing energy for the first singular mode and with  $n = 3$ . The preferential forcing direction switches from being mainly in the cross-sectional plane at low  $k$  to being mainly streamwise at high  $k$  at a value of  $k$  around 4 – 5 corresponding to the streamwise length of the near-wall type structures ( $k = 4.3$  corresponds to 1,000 viscous length units at  $Re = 24,580$ ).

(Recall from equation (4.19) that the normalization requires that the sum over all cross-stream and streamwise directions, i.e.,  $PF_{k,n,\omega,q}$ , is equal to 1.) The alternating preference for streamwise and azimuthal forcing and response modes at high  $k$  is a consequence of the oblique propagation of the individual propagating waves.

For the first singular mode and for  $k \leq 4 - 5$ , the forcing is predominantly in the azimuthal direction and the response in the streamwise direction. The same observation applies to all singular modes of order 1 – 15, for  $k \leq 1$ , but the cross-stream contribution to the forcing energy decreases with the singular mode order. For  $k \geq 1$ , the first singular mode exhibits a forcing mainly in the streamwise direction, and a predominant response in the azimuthal direction; for higher-order singular modes, the SVD tends to favor either a forcing and response in the streamwise direction, or a forcing and response in the azimuthal direction. The selection of the same dominant spatial direction for both the forcing and the response by the SVD at high  $k$  is a characteristic typical of a normal system. The contours of the forcing and response energy are qualitatively similar for other azimuthal wavenumbers and convection velocities.

Figure 4.17 shows isocontours of the cross-stream contribution to  $PF_{k,n,\omega,q}$  for the first singular mode,  $q = 1$ , as a function of streamwise wavenumber and convection velocity,  $(k, u_c)$ . At low streamwise wavenumber,  $k \leq 1$ , more than 80% of the forcing energy is in the cross-sectional plane, relatively independent of convection velocity, and figure 4.16 shows that the response is predominantly in the streamwise direction. For  $k \geq 4 - 5$ , which corresponds to the wavelength of the near-wall type structures ( $\lambda^+ = 1000$ ) at this Reynolds number, more than 50% of the forcing energy is in the streamwise direction, and the response is also predominantly in the streamwise direction.

Jovanovic & Bamieh (2005) studied a similar componentwise energy amplification in channel flows, and found amplification proportional to  $Re^3$  for forcing in the cross-sectional plane, resulting in a response in the streamwise velocity component. This large amplification was shown to be attributable to the non-normality of the linear operator governing the flow, arising from the coupling between forcing in the cross-sectional plane and the streamwise velocity component via the mean shear. All the other combinations of forcing and response directions were shown to lead to amplification proportional to the Reynolds number, as is typical of a normal system (Farrell & Ioannou, 1993).

While the Reynolds number scaling of the first singular modes has not been investigated explicitly, the results presented here appear to be in accordance with the results of Jovanovic & Bamieh (2005). The predominance of the azimuthal contribution to the forcing energy  $PF_{k,n,\omega,q}^\theta$  at low  $k$  observed in figure 4.16 is also supported by the results of Jovanovic & Bamieh (2005) showing that streamwise-constant near-wall excitation in the spanwise direction has by far the strongest effect on the flow.

#### 4.4.2 Influence of Non-Normality on Disturbance Amplification

Kim & Lim (2000) performed a DNS of turbulent channel flow with and without the linear term coupling the wall-normal velocity to the wall-normal vorticity, which is responsible for the non-normality of the underlying operator. Those authors showed that decoupling the evolution of the wall-normal vorticity from the evolution of the wall-normal velocity results in the decay of turbulent fluctuations, with the implication that non-normality is necessary (but not sufficient) to maintain turbulence. In this work, decoupling of the streamwise velocity fluctuations from cross-stream forcing (by canceling the mean shear) was used to quantify the influence of non-normality on the system amplification and on the selection of the preferential forcing and response directions by the SVD.

When the coupling is suppressed (zeroed) and there is little forcing in the radial direction, the resolvent formulation of equation (4.32) simplifies to

$$c_{k,n,\omega}^x = Re(\mathcal{D} + \mathcal{C})^{-1} f_{k,n,\omega}^x, \quad (4.42)$$

$$c_{k,n,\omega}^\theta = Re(\mathcal{I} + (\mathcal{D} + \mathcal{C} + r^{-2})^{-1} \mathcal{B}(\mathcal{D} + \mathcal{C} + r^{-2})^{-1} \mathcal{B})^{-1} (\mathcal{D} + \mathcal{C} + r^{-2})^{-1} f_{k,n,\omega}^\theta, \quad (4.43)$$

for the streamwise and azimuthal velocity components, respectively. Under these conditions, denoted the “decoupled system,” forcing in either the streamwise or azimuthal directions can only generate a response in the same direction.

The singular value as a function of the singular mode order at three different streamwise wavenumbers is plotted on figure 4.18 for the coupled and decoupled (effectively non-normal and normal) systems.

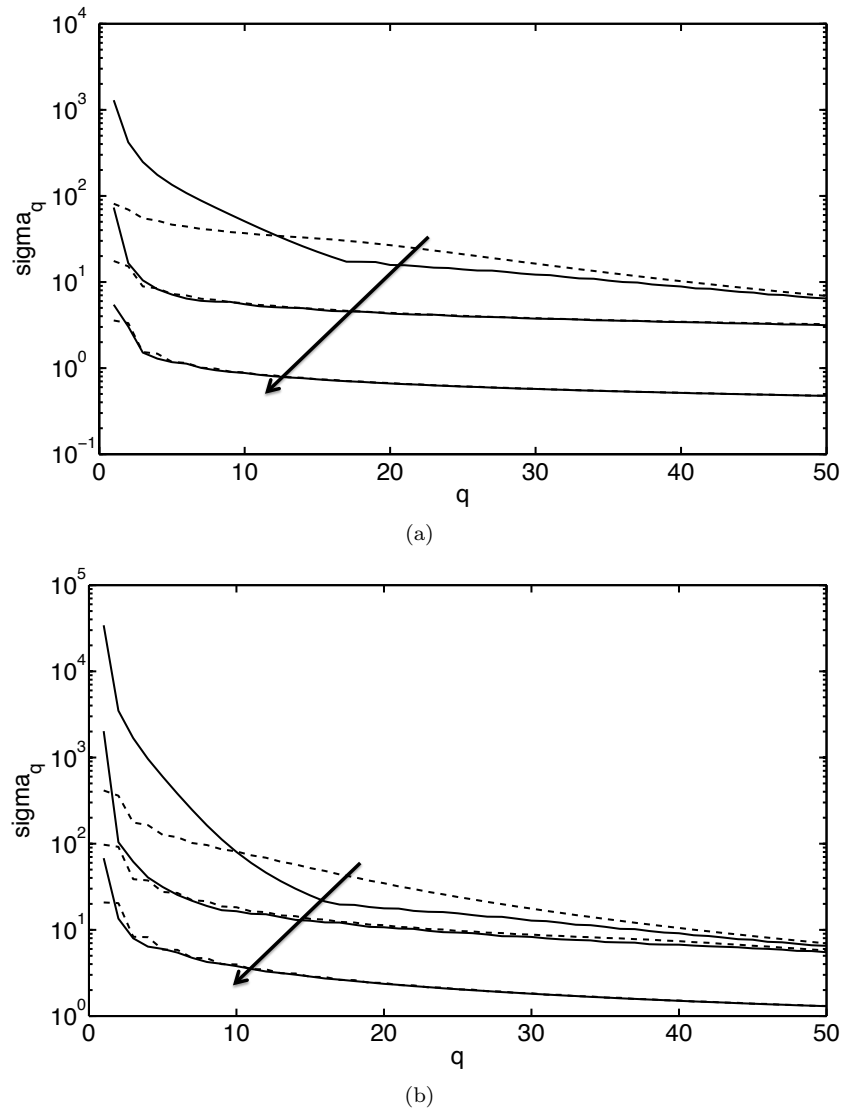


Figure 4.18: Amplification as a function of the singular mode order with (solid) and without (dashed) the linear coupling term for the modes  $(k, n, u_c) = (k, 3, 0.5)$  (a) and  $(k, n, u_c) = (k, 3, 0.8)$  (b) for three different streamwise wavenumbers  $k = 0.1, 1, 10$ . The arrow indicates the direction of increasing  $k$ .

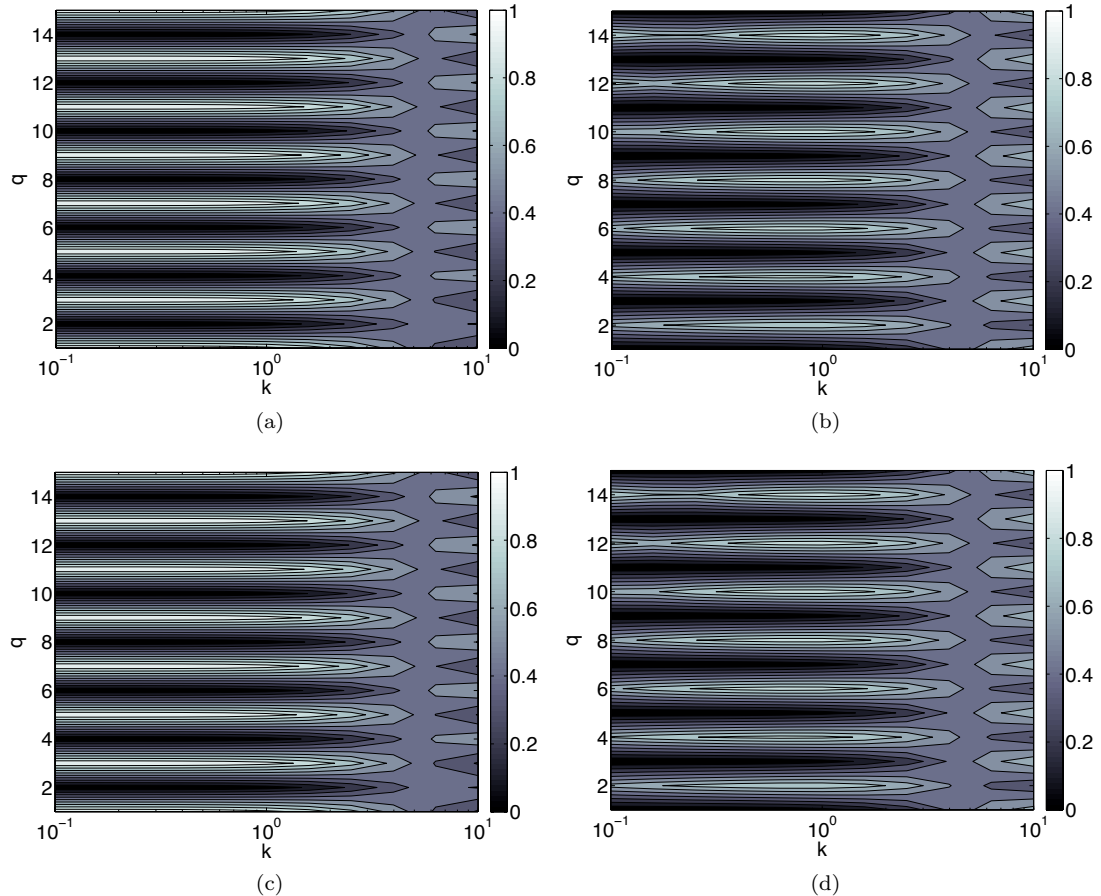


Figure 4.19: Streamwise (a),(c) and azimuthal (b),(d) contributions to the forcing (top row) and response (bottom row) energy, as a function of the streamwise wavenumber and singular mode order, in the absence of mean shear and for  $n = 3$ ,  $u_c = 0.8$ .

Any difference is concentrated in the first few singular values for  $k = 1, 10$ , while significantly larger amplification is obtained when non-normality effects are present for the first few singular modes at low streamwise wavenumber  $k \leq 1$ . The amplification gain due to the non-normality varies from a factor 2 – 3 at  $k = 10$  and  $u_c = 0.5$  to two orders of magnitude at  $k = 0.1$  and  $u_c = 0.8$ . For a range of higher-order modes at  $k = 0.1$ , however, the singular values for the decoupled system are larger than for the coupled case.

The contours of the streamwise and azimuthal contributions to the forcing and response energy, corresponding to this decoupled system, are plotted as a function of the streamwise wavenumber and singular mode order in figure 4.19. A comparison with the results from the fully coupled resolvent of figure 4.16 shows that any differences attributable to removing the source of non-normality are concentrated in the low- $k$  modes, with the exception of the first singular modes. The first singular modes have a response predominantly in the azimuthal direction at high  $k$  for both the coupled and decoupled systems, implying that, for the streamwise velocity component, non-normality effects are

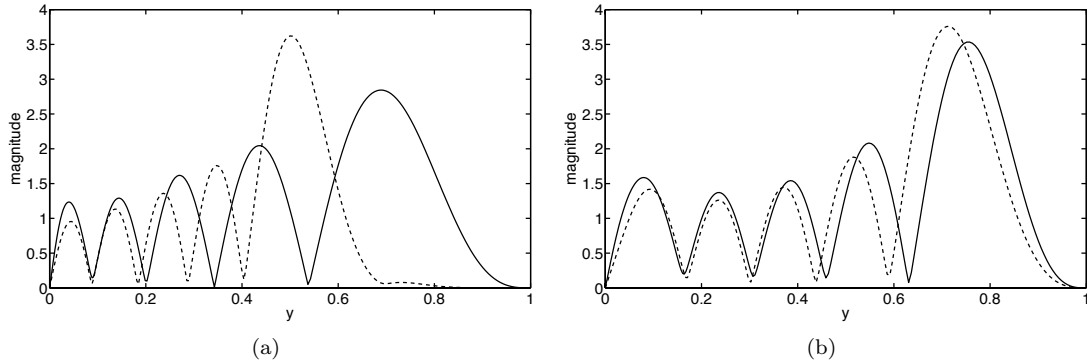


Figure 4.20: Magnitude of the streamwise velocity component of the singular mode with 5 local peaks for the Fourier modes  $(k, n, u_c) = (1, 3, 0.5)$  (a) and  $(k, n, u_c) = (1, 3, 0.8)$  (b) with (solid) and without (dashed) non-normality effects. The modes have a significantly different shape even though the amplification is the same with or without mean shear for these modes at  $k = 1$ . The order of the singular mode with five local peaks from SVD of the coupled and uncoupled resolvent is  $q = 5$  and  $q = 9$ , respectively.

only important at low  $k$ , regardless of the mode order.

In addition to enhancing the amplification associated with the normal operator, non-normality effects also result in the broadening of the mode shapes, as can be seen in figure 4.20, comparing the streamwise singular modes  $(k, n, u_c, q) = (1, 3, 0.5, 0.8, 5)$  and  $(k, n, u_c, q) = (1, 3, 0.5, 0.8, 9)$  obtained from SVD of the coupled and uncoupled resolvents, respectively. The mode order was chosen such that all the singular modes have 5 local peaks.

Equation (4.32) shows that the response in the streamwise direction is proportional to  $\mathcal{D}^{-3}$  for azimuthal forcing and  $\mathcal{D}^{-1}$  for streamwise forcing, implying that modes for which a non-normal mechanism contributes significantly to the amplification will be associated with small  $\mathcal{D}$ , or small curvature in the radial direction, namely modes that are tall in the wall-normal direction, in agreement with the radial variation of the long, globally energetic modes characterized in the previous section.

#### 4.4.3 Influence of Criticality on Disturbance Amplification for High $k$ Modes

The previous subsection showed that there is little difference between the coupled and decoupled system response for relatively high  $k$  modes, implying that the decoupled resolvent can be used to study the high  $k$  modes. In this case, the flow is purely convective, i.e., depends on the mean velocity profile  $U(y)$ , but not on the mean shear  $\frac{dU}{dy}$ , and the resolvent (equation (4.32)) simplifies to

$$c_{k,n,\omega}^x = Re(\mathcal{D} + \mathcal{C})^{-1} f_{k,n,\omega}^x, \quad (4.44)$$

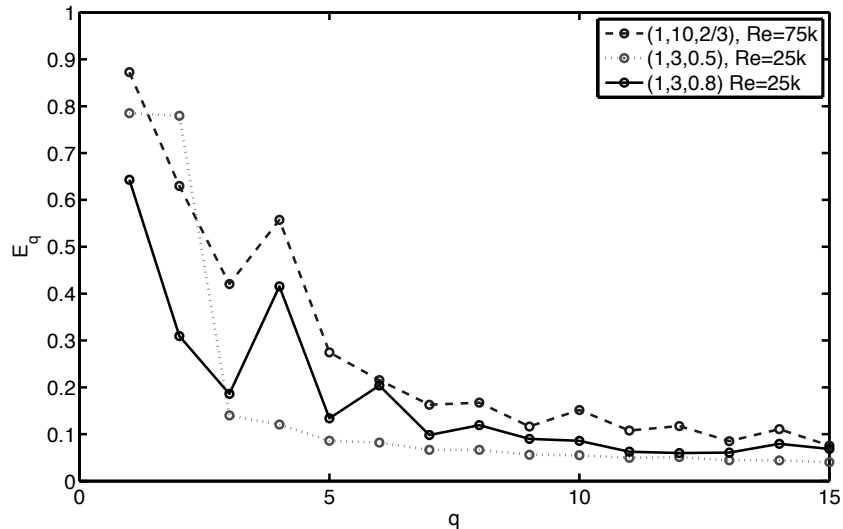


Figure 4.21: Fraction of energy contained in an annulus centered on the critical layer and covering 10% of the cross-sectional area as a function of the singular mode order. A uniform distribution of energy would correspond to 10% energy in the annulus.

for the streamwise velocity component, where  $\mathcal{C}$  and  $\mathcal{D}$  are respectively the criticality and dissipation terms. The response to streamwise forcing results from a balance between criticality and dissipation, thus large amplification is associated with a balance between a concentration of the energy in the vicinity of the critical layer (small  $\mathcal{C}$ ) and a broader distribution of energy in the radial direction (small  $\mathcal{D}$ ).

The influence of criticality can be crudely quantified by evaluating the fraction of energy in the immediate vicinity of the critical layer, where the local mean velocity is approximately equal to the convection velocity, and the  $\mathcal{C}$  term in equation (4.44) is small compared to  $\mathcal{D}$ . Figure 4.21 shows the fraction of energy contained in an annulus centered about the critical layer and covering 10% of the cross-sectional area. If there were no selection mechanism for the radial distribution of energy by the SVD, it can be hypothesized that the energy would be uniformly distributed with 10% energy in the annulus. For the first few singular modes, the energy contained in the annulus is significantly larger than 10%, implying that the SVD favors a relatively localized distribution of energy in the vicinity of the critical layer, but still sufficiently broad to keep the dissipation term  $\mathcal{D}$  low, i.e., the viscous effects tend to spread the localized critical-layer response in the radial direction. From equation (4.44), large amplification will be associated with these modes provided that  $\mathcal{D}$  is also (relatively) small. Figure 4.4 highlighted the relative “peakiness” of the higher-order mode amplitude distributions, likely to lead to higher dissipation relative to the lower modes, even accounting for decaying singular values with increasing mode order. Thus it appears that the effects of criticality, as well as the effects of non-normality, are concentrated in the first few singular modes at high  $k$ .

The concentration of both criticality and non-normality effects in the first few singular modes helps to explain the sharp decrease in singular values between the first mode and the higher-order singular modes shown in figure 4.18. This drop-off occurs faster than for the projection coefficients  $P_q$  (defined by equation (4.28)) computed for the long streamwise waves extracted from the DNS data, such that the amount of forcing increases with the singular mode order for the  $k \sim 1$  modes. Under white noise forcing, the higher-order singular modes have low (negligible) magnitude compared to the first few singular modes, due to the sharp decrease in singular values. In the DNS, however, the presence of higher-order singular modes containing a finite amount of energy implies that the nonlinear interactions result in a nonuniform distribution of forcing among the singular modes, characterized by increasing forcing energy with mode order. One possible explanation is that the nonlinear interaction of the first few (highly amplified) singular modes provides such forcing distribution, implying that the higher-order singular modes are a residual of that nonlinear interaction capturing the energy distribution in the wall-normal direction away from the critical-layer. Figure 4.22 illustrates how the DNS mode  $(0.84, 3, 0.83)$ , representative of the  $k \sim 1$  modes, is decomposed into a component corresponding to the first three singular modes, which are highly amplified, and a residual containing energy mainly away from the critical layer, and corresponding to the less-amplified higher-order singular modes. The singular modes of order larger than three each contain less than 2% of the DNS propagating wave energy, justifying a cutoff between the optimal and residual modes after the third mode.

A cartoon of the dominant amplification mechanisms as a function of the streamwise wavenumber and singular mode order for  $(n, u_c) = (3, 0.8)$  is shown in figure 4.23, superposed onto the contours of the singular value on a logarithmic scale. At low streamwise wavenumber, large amplification is due to non-normality (regions 1 and 2), with a boost from criticality at low mode order (region 2). At high streamwise wavenumber, criticality effects are concentrated in the first few singular modes (region 3) and result in the large amplification of these low-order modes. The higher-order modes experience a relatively low amplification inversely proportional to the viscosity, as is the case for a normal system (region 4). The line delimiting the region where non-normality effects are important follows the contours of the singular value, indicating that the amplification is significantly larger in the presence of non-normality effects. For the smaller structures, inspection of the resolvent (equation (4.32)) shows that, as the streamwise wavenumber increases, the amplification due to non-normality decreases at least as  $k^{-4}$ , and the only source of large amplification is criticality. This change in the dominant amplification mechanism is reflected in the change in the preferential forcing direction from cross-sectional to streamwise for  $k$  between 4 and 5, depending on the convection velocity (see figure 4.17) and has implications on the modeling of the smaller-scale structures that will be discussed in the next subsection.

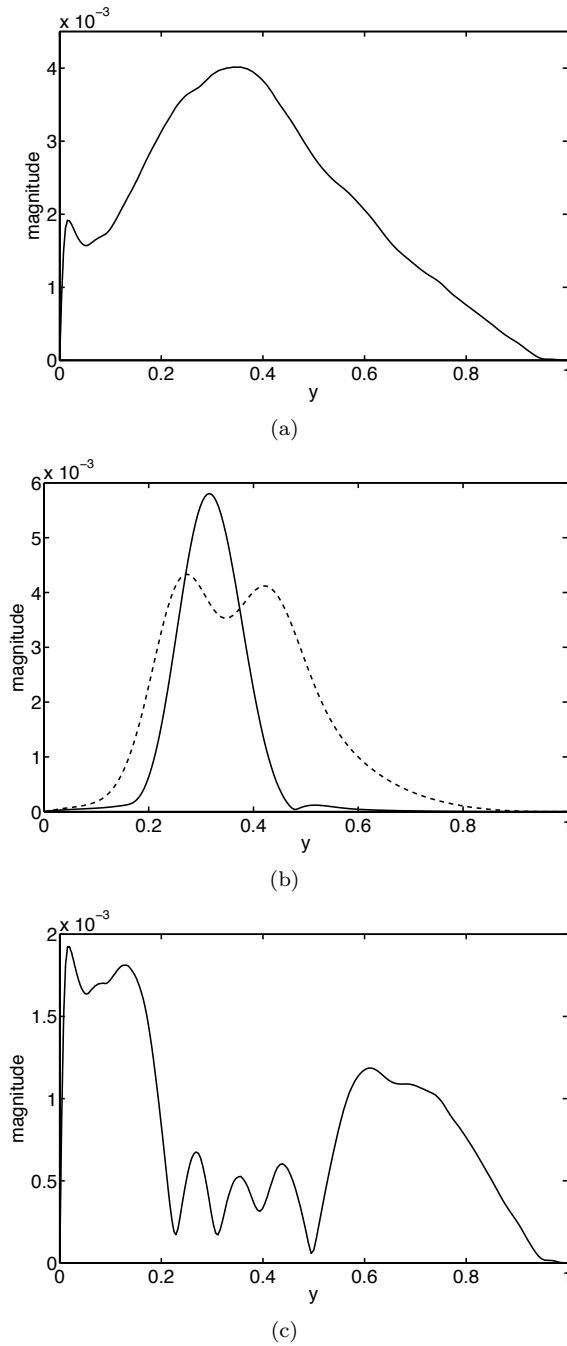


Figure 4.22: Wall-normal profile of (a) the DNS propagating wave  $(k, n, u_c) = (0.84, 3, 0.83)$ , (b) decomposed into the first three singular modes with (dashed) and without (solid) non-normality effects and (c) a residual containing energy mainly away from the critical layer, and corresponding to the higher-order singular modes.

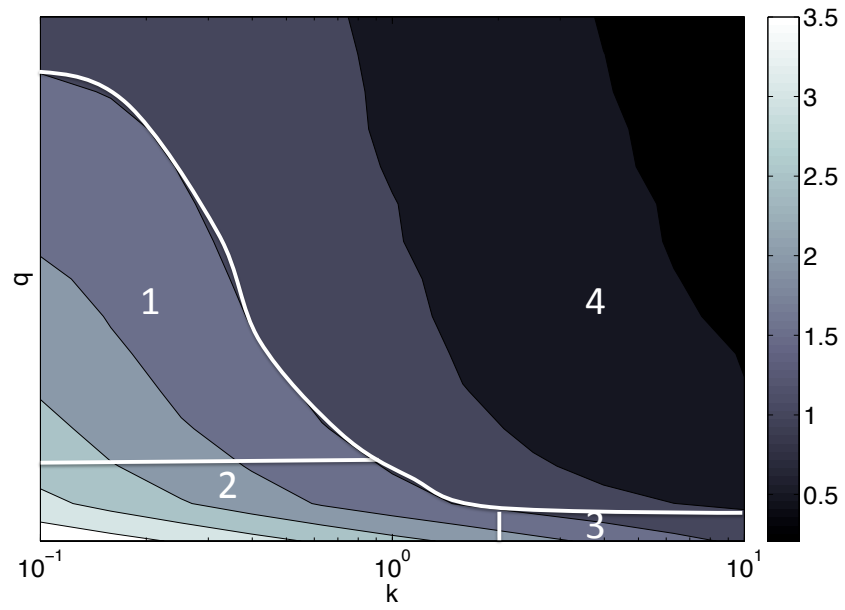


Figure 4.23: Schematic of the regions where non-normality effects (1 and 2) and criticality effects (2 and 3) are important on top of the contours of the singular value on a logarithmic scale, as a function of the streamwise wavenumber and singular mode order at  $(n, u_c) = (3, 0.8)$ . The line delimiting the region where non-normality effects are important (regions 1 and 2) follows the contours of the singular value, indicating that the amplification is significantly larger in the presence of non-normality effects. In region 4, the amplification is relatively low and inversely proportional to the viscosity as is the case for a normal system.

#### 4.4.4 Implications of the Present Study on Analyses on Criticality and Non-Normality

The analysis of the resolvent given above indicated a change in the dominant amplification mechanism from non-normality to criticality with increasing  $k$ , suggesting that the smaller structures are more localized in the wall-normal direction about the critical layer, as opposed to the large-scale structures spanning the whole radius. The smaller structures are expected to be well represented by the first singular mode which captures most of the criticality effects at high  $k$ . Figure 4.25 shows that the width of the first singular mode decreases with  $k$  and increases with  $u_c$ , such that the smaller structures are getting increasingly narrower in the wall-normal direction as they shorten in the streamwise direction or are located closer to the wall.

To quantify the radial extent of the small structures, the scaling of the first singular mode width with  $k$  and  $u_c$  is considered by defining the thickness,  $\epsilon$ , as the mode width at 50% peak magnitude.  $\epsilon$  depends on both  $k$  and  $u_c$  for a given Reynolds number. Figure 4.24(a) shows the thickness of the first singular mode as a function of  $k$  at  $u_c = \frac{2}{3}$  and  $n = 3$ , compared to the scaling law  $k^{-\alpha}$  with  $\alpha = \frac{1}{3}, \frac{1}{2}$ . The value of  $\alpha$  representing best the data varies from  $\frac{1}{3}$  to  $\frac{1}{2}$  depending on  $u_c$  and equals  $\frac{1}{2}$  at  $u_c = \frac{2}{3}$ . The dependence of the first singular mode thickness on the mean shear at the critical layer is evaluated by varying the convection velocity from 0.5 to 0.95 by increments of 0.05 (thereby effectively displacing the critical layer away from the wall to a region where the mean shear is lower as  $u_c$  is increased). The width of the first singular mode for the various convection velocities is plotted on figure 4.24(b) and is well represented by a line proportional to  $U'_{crit}{}^{-\frac{1}{3}}$ , where  $U'_{crit}$  is the mean shear at the critical layer.

Under the classical critical-layer analysis in Cartesian coordinates, e.g., Schmid & Henningson (2001), the Orr-Sommerfeld (OS) equation simplifies to an Airy equation in the vicinity of the critical layer, leading to an analytical scaling of the internal layer thickness as  $(kReU'_{crit})^{-\frac{1}{3}}$ . The internal layer is defined as the region around the critical layer where viscous effects need to be introduced to regularize the solution to the inviscid OS equation. While this analysis does not have a direct analytical analog in the cylindrical coordinates of pipe flow, because the OS and Squire equations are fully coupled, interestingly the upper bound on the exponent obtained for the scaling of the first singular mode thickness as a function of the streamwise wavenumber, and the exponent for the scaling with the mean shear at the critical layer, correspond to the classical  $-\frac{1}{3}$  exponent, suggesting at least a phenomenological similarity between coordinate systems.

The analysis of the resolvent presented in this chapter indicated that the small scales are localized in the vicinity of the critical-layer, and thus exhibit amplification with a large contribution from criticality. Experimental measurements have confirmed the wall-normal localization of the small scales near the critical-layer, or equivalently, that the short scales convect at the local mean velocity.

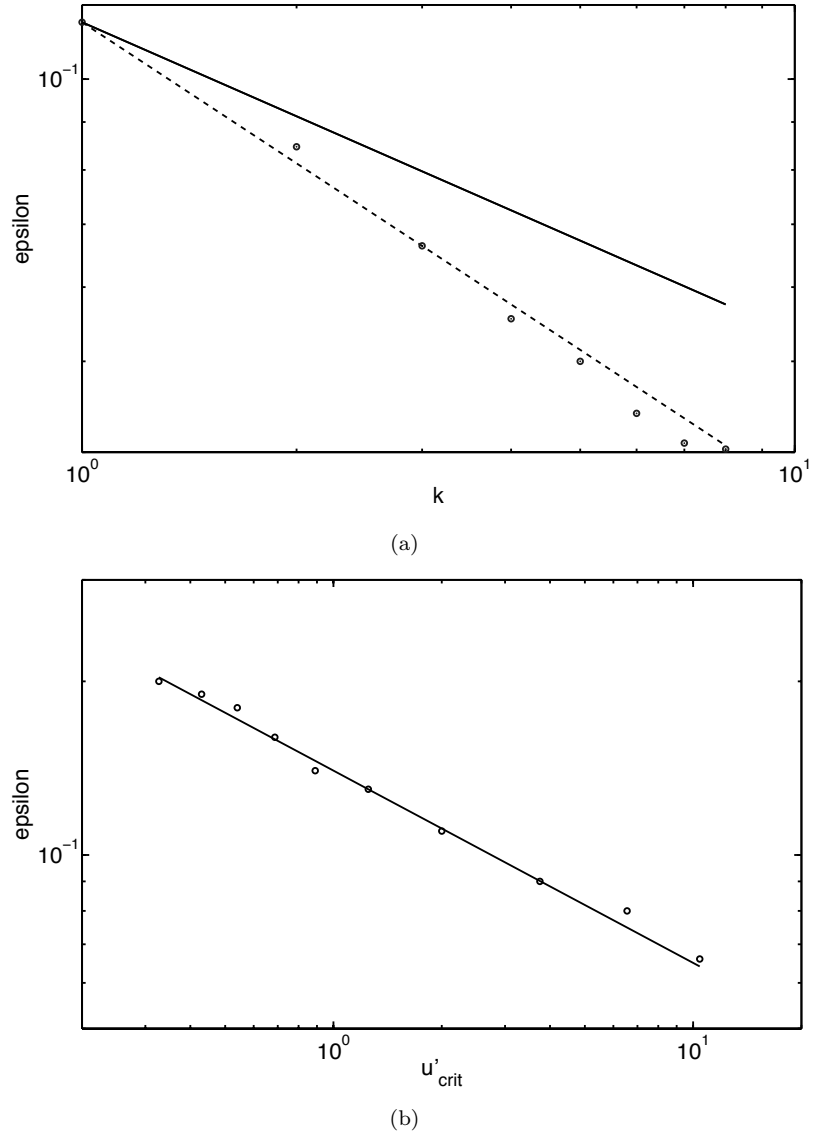
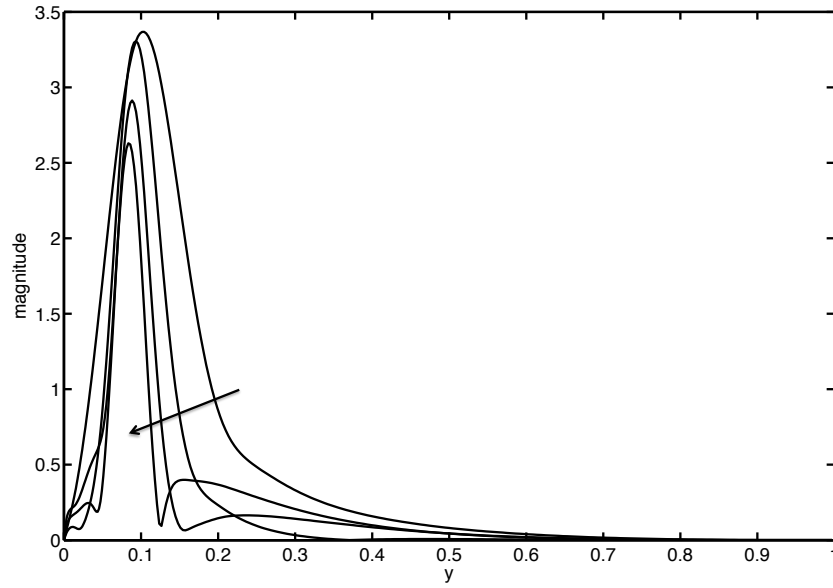
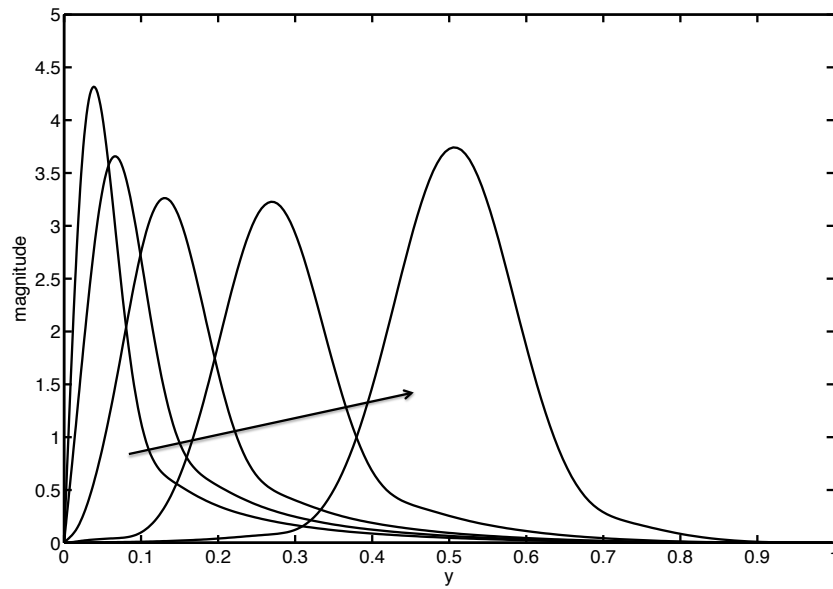


Figure 4.24: Thickness of the first singular mode as a function of the streamwise wavenumber  $k$  at  $u_c = \frac{2}{3}$  and  $n = 3$  (a) and as a function of the mean shear at the critical layer  $U'_{crit}$  for  $u_c$  varying from 0.5 to 0.95 by increments of 0.05 at  $k = 1$  and  $n = 3$ . The dots indicate the data points, the solid and dashed lines correspond to the scaling laws  $k^{-\frac{1}{3}}$  and  $k^{-\frac{1}{2}}$  (a), respectively, and  $U'^{-\frac{1}{3}}_{crit}$  (b).



(a)



(b)

Figure 4.25: Wall-normal profile of the first singular modes  $(k, n, u_c) = (1 : 2 : 8, 3, \frac{2}{3})$  (a) and  $(k, n, u_c) = (1, 3, 0.5 : 0.1 : 0.9)$  (b). The arrow indicates the direction of increasing  $k$  (a) and  $u_c$  (b).

The present analysis highlights that the small scales are well described by criticality-based studies, such as the approach of McKeon & Sharma (2010), due to the negligible importance of non-normality effects at high  $k$  shown on figure 4.18, and the strengthening of the spatial localization of the small scales around the critical-layer with increasing  $k$  (figure 4.25).

Experimental measurements have also shown that the long streamwise structures extend from the wall to the core of the pipe, and convect at a speed characteristic of the log region (LeHew *et al.*, 2011). These large scales are the ones captured in the present modal decomposition of the DNS due to their significant contribution to the radial-integrated streamwise turbulence intensity. In accordance with the experimental measurements and the modal decomposition of turbulent pipe flow DNS data, the low  $k$  propagating waves were shown, by the analysis of the resolvent presented here, to span the whole radius, i.e., to be tall in the wall-normal direction; as the decrease in curvature associated with the stretching of the modes in the wall-normal direction results in lower viscous dissipation. Due to their large radial extent, as shown on figure 4.8, these propagating waves are relatively insensitive to criticality effects, and are therefore best described by globally optimal, linear, studies of the NS equations, e.g., Schmid & Henningson (1994).

The concentration of the influence of non-normality effects in the low streamwise wavenumber, low-order modes is consistent with the classical picture of the energy cascade: the extraction of energy from the mean flow by the large scales (due to the non-normality of the underlying operator), transfer of energy from the large to the small scales by the triadic (nonlinear) interactions, and dissipation by the small scales. Further progress on the spectral transfer and spatial transport of energy is likely possible using the simplified form of the resolvent given in equation (4.44).

## 4.5 Summary

A modal decomposition of turbulent pipe flow DNS data at  $Re = 24,580$ , as a sum of propagating waves with model-based radial basis functions, was presented to obtain sparse representations of the flow that are coherent in the wall-normal direction, and to provide a link between the propagating waves and the governing equations, allowing for the identification of the physical mechanisms sustaining the waves.

The data requirements to perform the modal decomposition were significantly reduced by the use of compressive sampling to extract the frequency content of the flow, and by the introduction of model-based radial basis functions, obtained by following the approach of McKeon & Sharma (2010) to decompose the turbulent pipe flow resolvent into a set of orthonormal forcing and response modes, ranked by their amplification. These two approaches made possible an efficient modal decomposition of turbulent pipe flow in the three spatial directions and in time.

The decomposition of the flow as a sum of propagating waves was explored by McKeon &

Sharma (2010), and shown to capture the coherence in the wall-normal direction. The present study focused on the globally energetic propagating waves contributing largely to the radial-integrated, time-averaged, streamwise turbulence intensity. These propagating waves were shown to be long in the streamwise direction and tall in the wall-normal direction.

The modal decomposition is low order, due to the large amount of energy captured by the globally energetic modes, and requires only 51 2D Fourier modes to capture 20% of the streamwise turbulence intensity. Each 2D Fourier mode contains no more than 5 sparse frequencies, and for each frequency about 95% of the energy is captured with less than 12 singular modes in the radial direction. Altogether,  $51 \times 5 \times 12 \approx 3000$  modes are required to capture about 20% of the streamwise turbulence intensity, compared to the  $10^9$  degrees of freedom of the subsampled DNS, illustrating the significant data compression obtained with the modal decomposition presented in this chapter. This modal decomposition results in time-invariant amplitude coefficients, highlighting that the statistical steadiness of the flow is enforced, as opposed to the time-varying coefficients obtained via POD based on a time average of the velocity cross-correlation tensor.

Analysis of the resolvent led to the identification of the dominant physical mechanisms sustaining the propagating waves, as a function of their streamwise wavenumber. It was shown that the short streamwise waves are localized in the vicinity of the critical layer, and amplified by criticality effects, whereas the long streamwise waves are tall in the wall-normal direction, and have large amplification due to non-normality effects, resulting in energy extraction from the mean flow. In Cartesian coordinates, the standard Orr-Sommerfeld theory also predicts the importance of criticality effects and the scaling of the internal layer with  $k$ .

The resolvent can be seen as a rank one operator at high  $k$  in accordance with the predictions of McKeon & Sharma (2010), based on the sharp decrease in amplification from the first to the second singular mode, and as a low-rank operator at low  $k$ . Criticality analyses are particularly suited to describe the small scales, since non-normality effects play a minor role compared to criticality. It was shown in the present study that a value of  $k$  around 4 – 5, corresponding to the near-wall type structures at  $Re = 24,580$  ( $\lambda^+ = 1000$ ), constitutes the lower bound on the length of the modes benefiting mainly from criticality effects. At lower  $k$ , the propagating waves are tall in the wall-normal direction, in order to maximize non-normality effects. These large scales are the ones captured in the globally optimal studies, and in the present modal decomposition of DNS data, due to their significant contribution to the radial integrated streamwise turbulence intensity.

## Chapter 5

# Conclusion

Two models of turbulent pipe flow were presented to investigate the physics of turbulence, and to study the importance of linear non-normal, critical, and nonlinear effects, in wall-bounded turbulence. Analytical progress was made possible by appropriate simplifications of the Navier-Stokes equations, depending on the phenomena of interest, and by the decomposition of the flow into a mean component and fluctuations about the mean. Two main features of turbulent pipe flow, i.e., the blunting of the velocity profile during transition and the sustenance of the turbulent fluctuations, were studied in detail. The mechanisms responsible for the blunting of the velocity profile were investigated by considering a streamwise-constant projection of the Navier-Stokes equations, whereas the mechanisms sustaining different classes of structures were identified by linear analysis of the resolvent, using the modeling assumption that the nonlinear terms in the Navier-Stokes equations act as an unstructured forcing of the linear dynamics.

The main contributions of this thesis to the understanding of the role of linear non-normal, critical, and nonlinear effects in wall-bounded turbulence are summarized in this chapter. A more detailed description of the results obtained with each model is given at the end of their respective chapter.

The non-normal mechanisms are associated with the linear coupling term between the cross-sectional and streamwise velocity fluctuations, and were shown to result in large amplification of the cross-stream forcing modes, in both the nonlinear streamwise-constant model and the analysis of the turbulent pipe flow resolvent. The most amplified response modes, computed with the two models presented in this thesis, correspond to streamwise streaks of the streamwise velocity fluctuations, in accordance with the results of Jovanovic & Bamieh (2005). Non-normality effects are prominent at low streamwise wavenumber and were shown to be maximized if the low streamwise wavenumber modes were also tall in the wall-normal direction, in order to decrease their viscous dissipation; as opposed to being localized near the wall, where the shear is higher. This is a new formalization of the constraints imposed by non-normality on the radial extent of optimally amplified modes.

Criticality effects are associated with the nearly singular behavior of the resolvent at high

Reynolds number, when a propagating wave convects at a speed corresponding to the local mean velocity (at, or close to, the peak magnitude of the wave). Criticality effects result in the large amplification of propagating waves that are localized near the critical-layer, and were shown in this thesis to be the dominant amplification mechanisms for the high streamwise wavenumber modes, for which non-normality effects are negligible; and to constrain the optimally amplified high streamwise wavenumber modes to be localized in the vicinity of the critical-layer. The work in this thesis allows the reconciliation of the well-known results (Bamieh & Dahleh, 2001; Jovanovic & Bamieh, 2005; Schmid & Henningson, 1994) concerning optimal disturbance amplification due to non-normal effects with the recent resolvent analysis of McKeon & Sharma (2010), which highlighted the importance of criticality effects.

Nonlinear effects result in the redistribution of the high- and low-speed streaks over the cross-section of the pipe, and were shown to be required to capture the change in mean flow that occurs during transition to turbulence. The nonlinear terms convect the streamwise streaks in such a way that the high-speed streaks concentrate near the wall and the low-speed streaks near the center of the pipe, thereby causing a blunting of the velocity profile. These mechanisms were discovered by numerical simulation of the streamwise-constant model under both stochastic and deterministic forcing of the streamfunction equation.

The two models were shown to capture energetic structures of wall-bounded turbulence, taking the form of streamwise-elongated rolls and streaks in the streamwise-constant model, and of coherent propagating waves in the model-based modal decomposition of turbulent pipe flow, and were validated against experimental and numerical data.

A novel application of compressive sampling was presented, to efficiently extract the frequency content of energetic modes in wall-bounded turbulence. Compressive sampling, together with the use of radial basis functions obtained by SVD of the resolvent, made possible a full modal decomposition of turbulent pipe flow, in the three spatial directions and in time, resulting in sparse representations of the flow. A full modal decomposition of wall-bounded turbulence is not commonly pursued, due to the significant data requirements to compute statistically-converged, data-based, radial basis functions.

Future research will involve determining the Reynolds number dependence of the gradual transition from non-normality to criticality dominated amplification; or evaluating the sensitivity of the radial basis functions computed by SVD of the resolvent to changes in the input mean velocity profile, in order to couple the resolvent analysis to the streamwise-constant model, and thereby obtain a data independent framework for the study of wall-bounded turbulence. It also seems possible to relate the constraints on the radial extent of the modes imposed by the dominant amplification mechanisms (non-normality and criticality), described in this thesis, to the spatial flux of scale energy in the wall-normal direction.

## Appendix A

# Matlab code used to solve the convex optimization problem

```

% Nr is the number of grid points in the radial direction
% Ns is the number of samples
% 2D_Fourier(Nr,Ns) is the 2D Fourier mode as a function of the wall-normal
% distance r discretized over Nr points and the Ns number of samples
% (time instant ts)
% F_out(Nr,Nopti) is the output of the minimization corresponding to
% the frequency content as a function of the wall-normal distance.

Nopti=10*Ns; % number of frequencies for the optimization

f=(-Nopti/2+1:1:Nopti/2)/(Nopti/2); % equispaced frequencies for the optimization

C=exp(-1i*2*pi*ts*f); % constraint matrix: output must match input
% at the sampling time instants

for j=1:Nr
    cvx_begin
    cvx_quiet(true)
        variable x(Nopti) complex;
        minimize(norm(x,1)); % minimize the sum of the absolute value
                                % of the temporal Fourier coefficients

        subject to
            C * x==2D_Fourier(j,:);
    cvx_end
    F_out(j,:)=x;
end.

```

# Bibliography

- ADRIAN, R. J. 2007 Vortex organization in wall turbulence. *Phys. Fluids* **19** (041301).
- DEL ÁLAMO, J. C. & JIMÉNEZ, J. 2006 Linear energy amplification in turbulent channels. *J. Fluid Mech.* **559**, 205–213.
- BALTZER, J. R. & ADRIAN, R. J. 2011 Structure, scaling, and synthesis of proper orthogonal decomposition modes of inhomogeneous turbulence. *Phys. Fluids* **23** (1).
- BAMIEH, B. & DAHLEH, M. 2001 Energy amplification in channel flows with stochastic excitation. *Phys. Fluids* **13** (11), 3258–3269.
- BERKOOZ, G., HOLMES, P. & LUMLEY, J. L. 1993 The Proper Orthogonal Decomposition in the analysis of turbulent flows. *Annu. Rev. Fluid Mech.* **25**, 539–575.
- BILINSKIS, I. 2007 *Digital Alias-Free Signal Processing*. John Wiley.
- BOURGUIGNON, J.-L. & MCKEON, B. J. 2011 A streamwise-constant model of turbulent pipe flow. *Phys. Fluids* **23** (9).
- CANDÈS, E. J., ROMBERG, J. & TAO, T. 2006 Robust uncertainty principles: Exact signal reconstruction from highly incomplete frequency information. *IEEE Trans. Inf. Theory* **52** (2), 489–509.
- CANDÈS, E. J. & WAKIN, M. B. 2008 An introduction to compressive sampling. *IEEE Signal Processing Magazine* **25** (2), 21–30.
- CANUTO, C. 2006 *Spectral Methods: Fundamentals in Single Domains*. Springer-Verlag.
- CHEN, S., DONOHO, D. L. & SAUNDERS, M. A. 1998 Atomic decomposition by basis pursuit. *SIAM Journal On Scientific Computing* **20** (1), 33–61.
- CHUNG, D. & MCKEON, B. J. 2010 Large-eddy simulation of large-scale structures in long channel flow. *J. Fluid Mech.* **661**, 341–364.
- DARBYSHIRE, A. G. & MULLIN, T. 1995 Transition to turbulence in constant-mass-flux pipe flow. *J. Fluid Mech.* **289**, 83–114.

- DENNIS, D. & NICKELS, T. 2008 On the limitations of Taylor's hypothesis in constructing long structures in wall-bounded turbulent flow. *J. Fluid Mech.* **614**, 197–206.
- VAN DOORNE, C. W. H. & WESTERWEEL, J. 2009 The flow structure of a puff. *Phil. Trans. Royal Soc. A* **367**, 489–507.
- DUGGLEBY, A., BALL, K. S., PAUL, M. R. & FISCHER, P. F. 2007 Dynamical eigenfunction decomposition of turbulent pipe flow. *J. Turbulence* **8** (43), 1–24.
- DUGGLEBY, A., BALL, K. S. & SCHWAENEN, M. 2009 Structure and dynamics of low Reynolds number turbulent pipe flow. *Phil. Trans. Royal Soc. A* **367** (1888), 473–488.
- DUGUET, Y., WILLIS, A. P. & KERSWELL, R. R. 2010 Slug genesis in cylindrical pipe flow. *J. Fluid Mech.* **663**, 180–208.
- ECKHARDT, B. 2007 Turbulence transition in pipe flow. *Annu. Rev. Fluid Mech.* **39**, 447–468.
- ECKHARDT, B. 2008 Turbulence transition in pipe flow: Some open questions. *Nonlinearity* **21**, 1–11.
- FARRELL, B. F. & IOANNOU, P. J. 1993 Stochastic forcing of the linearized Navier-Stokes equations. *Phys. Fluids* **5** (11), 2600–2609.
- GAYME, D., MCKEON, B. J., PAPACHRISTODOULOU, A., BAMIEH, B. & DOYLE, J. C. 2010 A streamwise constant model of turbulence in plane Couette flow. *J. Fluid Mech.* **658**, 99–119.
- GEORGE, W. K. & CASTILLO, L. 1997 Zero-pressure-gradient turbulent boundary layer. *Appl. Mech. Rev.* **50**, 689–729.
- GUALA, M., HOMMEMA, S. E. & ADRIAN, R. J. 2006 Large-scale and very-large-scale motions in turbulent pipe flow. *J. Fluid Mech.* **554**, 521–542.
- HEINRICHS, W. 2004 Spectral collocation schemes on the unit disc. *J. Comp. Phys.* **199** (1), 66–86.
- HELLSTROËM, L. H. O., SINHA, A. & SMITS, A. J. 2011 Visualizing the very-large-scale motions in turbulent pipe flow. *Phys. Fluids* **23** (1), 703–707.
- HOF, B., VAN DOORNE, C. W. H., WESTERWEEL, J., NIEUWSTADT, F. T. M., FAISST, H., ECKHARDT, B., WEDIN, H., KERSWELL, R. R. & WALEFFE, F. 2004 Experimental observation of nonlinear traveling waves in turbulent pipe flow. *Science* **305** (5690), 1594–1598.
- HOF, B., DE LOZAR, A., AVILA, M., TU, X. & SCHNEIDER, T. M. 2010 Eliminating turbulence in spatially intermittent flows. *Science* **327** (5972), 1491–1494.

- HOYAS, S. & JIMÉNEZ, J. 2006 Scaling of velocity fluctuations in turbulent channels up to  $Re_\tau = 2003$ . *Phys. Fluids* **18**.
- HUTCHINS, N. & MARUSIC, I. 2007 Large-scale influences in near-wall turbulence. *Phil. Trans. Royal Soc. A* **365**, 647–664.
- HWANG, Y. & COSSU, C. 2010 Linear nonnormal energy amplification of harmonic and stochastic forcing in the turbulent channel flow. *J. Fluid Mech.* **664**, 51–73.
- JIMÉNEZ, J. & MOSER, R. D. 2007 What are we learning from simulating wall turbulence? *Phil. Trans. R. Soc. A* **365**, 715–732.
- JONSSON, I. & KAGSTROM, B. 2003 RECSY – A high performance library for Sylvester-type matrix equations. *Euro-Par 2003 Parallel Processing, Proceedings* **2790**, 810–819.
- JOSEPH, D. D. 1968 Eigenvalue bounds for the Orr-Sommerfeld equation. *J. Fluid Mech.* **33**, 617–621.
- JOVANOVIĆ, M. R. & BAMIEH, B. 2005 Componentwise energy amplification in channel flows. *J. Fluid Mech.* **534**, 145–183.
- KIM, J. & LIM, J. 1993 A linear process in wall-bounded turbulent shear flows. *Phys. Fluids* **12** (8), 1885–1888.
- KIM, J. & LIM, J. 2000 A linear process in wall-bounded turbulent shear flows. *Phys. Fluids* **12** (8), 1885–1888.
- KIM, K. C. & ADRIAN, R. J. 1999 Very large-scale motion in the outer layer. *Phys. Fluids* **11** (2), 417–422.
- KLINE, S. J., REYNOLDS, W. C., SCHRAUB, F. A. & RUNSTADLER, P. W. 1967 The structure of turbulent boundary layers. *J. Fluid Mech.* **30**, 741–772.
- LEHEW, J., GUALA, M. & MCKEON, B. J. 2011 A study of the three-dimensional spectral energy distribution in a zero pressure gradient turbulent boundary layer. *Expts. in Fluids* **51** (4), 997–1012.
- LINDGREN, E. R. 1957 The transition process and other phenomena in viscous flow. *Arkiv For Fysik* **12**, 1–169.
- LIU, Z., ADRIAN, R. J. & HANRATTY, T. J. 2001 Large-scale modes of turbulent channel flow: Transport and structure. *J. Fluid Mech.* **448**, 53–80.
- LUSTIG, M., DONOHO, D. & PAULY, J. M. 2007 Sparse MRI: The application of compressed sensing for rapid MR imaging. *Magn. Reson. Med.* **58** (6), 1182–1195.

- MARUSIC, I., MCKEON, B. J., MONKEWITZ, P. A., NAGIB, H. M., SMITS, A. J. & SREENIVASAN, K. R. 2010 Wall-bounded turbulent flows at high Reynolds numbers: Recent advances and key issues. *Phys. Fluids* **22** (6), 1–24.
- MASLOWE, S. A. 1986 Critical layers in shear flows. *Annu. Rev. Fluid Mech.* **18**, 405–432.
- MCKEON, B. J. & SHARMA, A. 2010 A critical layer framework for turbulent pipe flow. *J. Fluid Mech.* **658**, 336–382.
- MEINHART, C. D. & ADRIAN, R. J. 1995 On the existence of uniform momentum zones in a turbulent boundary layer. *Phys. Fluids* **7** (4), 694–696.
- MELLIBOVSKY, F., MESEGUER, A., SCHNEIDER, T. M. & ECKHARDT, B. 2009 Transition in localized pipe flow turbulence. *Phys. Rev. Letters* **103**.
- MESEGUER, A. 2003 Streak breakdown instability in pipe Poiseuille flow. *Phys. Fluids* **15** (5), 1203–1213.
- MESEGUER, A. & TREFETHEN, L. N. 2003 Linearized pipe flow to Reynolds number  $10^7$ . *J. Comp. Phys.* **186**, 178–197.
- MORRISON, J. F., MCKEON, B. J., JIANG, W. & SMITS, A. J. 2004 Scaling of the streamwise velocity component in turbulent pipe flow. *J. Fluid Mech.* **1508**, 99–131.
- MORRISON, W. R. B., BULLOCK, K. J. & KRONAUER, R. E. 1971 Experimental evidence of waves in the sublayer. *J. Fluid Mech.* **47**, 639–656.
- NISHI, M., UENSAL, B., DURST, F. & BISWAS, G. 2008 Laminar-to-turbulent transition of pipe flows through puffs and slugs. *J. Fluid Mech.* **614**, 425–446.
- PAPACHRISTODOULOU, A. 2005 Scalable analysis of nonlinear systems using convex optimization. PhD thesis, California Institute of Technology.
- PEYRET, R. 2002 *Spectral methods for incompressible viscous flow, Applied mathematical sciences*, vol. 148. Springer.
- REDDY, S. C. & IOANNOU, P. J. 2000 Energy transfer analysis of turbulent plane Couette flow. *Proceedings of the IUTAM Laminar-Turbulent Transition* pp. 211–216.
- RESHOTKO, E. & TUMIN, A. 2001 Spatial theory of optimal disturbances in a circular pipe flow. *Phys. Fluids* **13** (4), 991–996.
- ROBINSON, S. K. 1991 Coherent motions in the turbulent boundary layer. *Annu. Rev. Fluid Mech.* **23**, 601–639.

- SALWEN, H., COTTON, F. W. & GROSCH, C. E. 1980 Linear stability of Poiseuille flow in a circular pipe. *J. Fluid Mech.* **98**, 273–284.
- SCHMID, P. J. 2000 Linear stability theory and bypass transition in shear flows. *Phys. Plasmas* **7**, 1788–1794.
- SCHMID, P. J. & HENNINGSON, D. S. 1994 Optimal energy density growth in Hagen-Poiseuille flow. *J. Fluid Mech.* **277**, 197–225.
- SCHMID, P. J. & HENNINGSON, D. S. 2001 *Stability and Transition in Shear Flows, Applied Mathematical Sciences*, vol. 142. Springer.
- SCHNEIDER, T. M., ECKHARDT, B. & YORKE, J. A. 2007 Turbulence transition and the edge of chaos in pipe flow. *Phys. Rev. Letters* **99** (3).
- SCHOPPA, W. & HUSSAIN, F. 2002 Coherent structure generation in near-wall turbulence. *J. Fluid Mech.* **453**, 57–108.
- SHIMIZU, M. & KIDA, S. 2009 A driving mechanism of a turbulent puff in pipe flow. *Fluid Dynam. Res.* **41**.
- SMITS, A. J., MCKEON, B. J. & MARUSIC, I. 2011 High Reynolds number wall turbulence. *Annu. Rev. Fluid Mech.* **43**, 353–375.
- SPALART, P. R., MOSER, R. D. & ROGERS, M. M. 1991 Spectral methods for the Navier-Stokes equations with one infinite and two periodic directions. *J. Comp. Phys.* **96** (2), 297–324.
- SWANSON, C. J., JULIAN, B., IHAS, G. G. & DONNELLY, R. J. 2002 Pipe flow measurements over a wide range of Reynolds numbers using liquid helium and various gases. *J. Fluid Mech.* **461**, 51–60.
- THEODORSEN, T. 1952 Mechanism of turbulence. In *Proc. 2nd Midwestern Conf. on Fluid Mech.*, pp. 1–19. Ohio State University, Columbus, Ohio.
- DEN TOONDER, J. M. J. & NIEUWSTADT, F. T. M. 1997 Reynolds number effects in a turbulent pipe flow for low to moderate Re. *Phys. Fluids* **9** (11), 3398–3409.
- TREFETHEN, L. N. & EMBREE, M. 2005 *Spectra and Pseudospectra: The Behavior of Nonnormal Matrices and Operators*. Princeton University Press.
- TROPP, J. A., LASKA, J. N., DUARTE, M. F., ROMBERG, J. K. & BARANIUK, R. G. 2010 Beyond Nyquist: Efficient sampling of sparse bandlimited signals. *IEEE Trans. Inf. Theory* **56** (1), 520–544.

- WALEFFE, F. 1997 On a self-sustaining process in shear flows. *Phys. Fluids* **9** (4), 883–900.
- WU, X. & MOIN, P. 2008 A direct numerical simulation study on the mean velocity characteristics in turbulent pipe flow. *J. Fluid Mech.* **608**, 81–112.
- WYGNANSKI, I. J. & CHAMPAGNE, F. H. 1973 On transition in a pipe. Part 1: The origin of puffs and slugs and the flow in a turbulent slug. *J. Fluid Mech.* **59**, 281–335.
- ZIKANOV, O. Y. 1996 On the instability of pipe Poiseuille flow. *Phys. Fluids* **8** (11), 2923–2932.